SENSITIVITY STUDY OF THE EFFECTS OF MINERAL DUST PARTICLE NONSPHERICITY AND THIN CIRRUS CLOUDS ON MODIS DUST OPTICAL DEPTH RETRIEVALS AND DIRECT RADIATIVE FORCING CALCULATIONS

A Dissertation

by

QIAN FENG

Submitted to the Office of Graduate Studies of
Texas A&M University
in partial fulfillment of the requirements for the degree of

DOCTOR OF PHILOSOPHY

August 2010

Major Subject: Atmospheric Sciences

SENSITIVITY STUDY OF THE EFFECTS OF MINERAL DUST PARTICLE NONSPHERICITY AND THIN CIRRUS CLOUDS ON MODIS DUST OPTICAL DEPTH RETRIEVALS AND DIRECT RADIATIVE FORCING CALCULATIONS

A Dissertation

by

QIAN FENG

Submitted to the Office of Graduate Studies of
Texas A&M University
in partial fulfillment of the requirements for the degree of

DOCTOR OF PHILOSOPHY

Approved by:

Chair of Committee,	Ping Yang
Committee Members,	George W. Kattawar
	Shaima L. Nasiri
	Hung-Lung Huang
Head of Department,	Kenneth P. Bowman

August 2010

Major Subject: Atmospheric Sciences

ABSTRACT

Sensitivity Study of the Effects of Mineral Dust Particle Nonsphericity and Thin Cirrus Clouds on MODIS Dust Optical Depth Retrievals and Direct Radiative Forcing Calculations. (August 2010)

Qian Feng, B.S., Ocean University of China;

M.S., Ocean University of China;

Ph.D., Ocean University of China

Chair of Advisory Committee: Dr. Ping Yang

A special challenge posed by mineral dust aerosols is associated with their predominantly nonspherical particle shapes. In the present study, the scattering and radiative properties for nonspherical mineral dust aerosols at violet-to-blue (0.412, 0.441, and 0.470 μm) and red (0.650 μm) wavelengths are investigated. To account for the effect of particle nonsphericity on the optical properties of dust aerosols, the particle shapes for these particles are assumed to be spheroids. A combination of the T-matrix method and an improved geometric optics method is applied to the computation of the single-scattering properties of spheroidal particles with size parameters ranging from the Rayleigh to geometric optics regimes. For comparison, the Mie theory is employed to compute the optical properties of spherical dust particles that have the same volumes as their nonspherical counterparts. The differences between the phase functions of spheroidal and spherical particles lead to quite different lookup tables (LUTs) involved in retrieving dust aerosol properties. Moreover, the applicability of a hybrid approach based

on the spheroid model for the phase function and the sphere model for the other phase matrix elements is demonstrated. The present sensitivity study, employing the Moderate Resolution Imaging Spectroradiometer (MODIS) observations and the fundamental principle of the Deep Blue algorithm, illustrates that neglecting the nonsphericity of dust particles leads to an underestimate of retrieved aerosol optical depth at most scattering angles, and an overestimate is noted in some cases.

The sensitivity study of the effect of thin cirrus clouds on dust optical depth retrievals is also investigated and quantified from MODIS observations. The importance of identifying thin cirrus clouds in dust optical depth retrievals is demonstrated. This has been undertaken through the comparison of retrieved dust optical depths by using two different LUTs. One is for the dust only atmosphere, and the other is for the atmosphere with overlapping mineral dust and thin cirrus clouds. For simplicity, the optical depth and bulk scattering properties of thin cirrus clouds are prescribed *a priori*. Under heavy dusty conditions, the errors in the retrieved dust optical depths due to the effect of thin cirrus are comparable to the assumed optical depth of thin cirrus clouds.

With the spheroidal and spherical particle shape assumptions for mineral dust aerosols, the effect of particle shapes on dust radiative forcing calculations is estimated based on Fu-Liou radiative transfer model. The effect of particle shapes on dust radiative forcing is illustrated in the following two aspects. First, the effect of particle shapes on the single-scattering properties of dust aerosols and associated dust direct radiative forcing is assessed, without considering the effect on dust optical depth retrievals. Second, the effect of particle shapes on dust direct radiative forcing is further discussed by including the effect of particle nonsphericity on dust optical depth retrievals.

DEDICATION

This dissertation is dedicated to all my family and friends who have inspired and supported me throughout my life.

ACKNOWLEDGMENTS

First of all, I would like to thank my advisor, Dr. Ping Yang, for his instructive advice and useful suggestions throughout my work on this project. I am deeply grateful for everything he has done for me, and for the opportunity he offered to me to continue my Ph.D. study. I would also like to thank my committee members, Dr. George Kattawar, Dr. Shaima Nasiri and Dr. Hung-Lung (Allen) Huang, for their direction and assistance during my study. I would like to thank Dr. Sarah Brooks for the constructive comments she has given to me.

This research is supported by a grant (NNX08AP29G) from NASA's Radiation Sciences Program managed by Dr. Hal Maring, a NOAA grant (DG133E08CN0231), and partly supported by a NOAA grant (DG133E08CN0231). The effort on the single-scattering computation involved in this project is partly supported by a grant (ATM-0803779) from the National Science Foundation (NSF) Physical & Dynamic Meteorology Program managed by Dr. Bradley Smull.

Finally, I would like to thank my wife, Zhen Hong, the love of my life, for her continuous support and encouragement she has given me. I would also like to thank my family and friends, especially my parents, for all of the support they have given me throughout the years.

TABLE OF CONTENTS

Page

ABSTRACT iii

DEDICATION v

ACKNOWLEDGMENTS vi

TABLE OF CONTENTS vii

LIST OF FIGURES ix

LIST OF TABLES xv

1. INTRODUCTION 1

    1.1 Mineral dust and its role in climate 1
    1.2 Satellite-based remote sensing of mineral dust aerosols 1
    1.3 Direct radiative forcing by mineral dust aerosols 6
    1.4 Organization of the dissertation 7

2. METHODOLOGY 9

    2.1 Objective 9
    2.2 Methods for scattering simulations 9
    2.3 Radiative transfer simulations 17
    2.4 Aerosol retrieval algorithm 21

3. SCATTERING AND RADIATIVE PROPERTIES FOR MINERAL DUST AEROSOLS AND THE EFFECT OF PARTICLE NONSPHERICITY ON RETRIEVING DUST OPTICAL DEPTHS 24

    3.1 Methods 24
    3.2 Bulk scattering properties of mineral dust aerosols 24
    3.3 Radiative properties of mineral dust aerosols 32
    3.4 The effect of particle nonsphericity on dust optical depth retrievals 40
    3.5 Summary 61

Page

4. THE EFFECT OF THIN CIRRUS CLOUDS ON DUST OPTICAL DEPTH RETRIEVALS 62

4.1 Methods 62
4.2 Dust detection methods 63
4.3 Bulk scattering properties for mineral dust and thin cirrus clouds 70
4.4 The effect of thin cirrus on dust optical depth retrievals 73
4.5 Summary 86

5. THE EFFECT OF PARTICLE SHAPES ON SHORTWAVE DIRECT RADIATIVE FORCING CALCULATIONS FOR MINERAL DUST 87

5.1 Methods 87
5.2 Scattering property simulations 87
5.3 Radiative forcing simulations 92
5.4 Sensitivity study of the effect of particle shapes on dust direct radiative forcing 97
5.5 Summary 104

6. SUMMARY AND CONCLUSION 105

REFERENCES 107

VITA 119

LIST OF FIGURES

FIGURE Page

1 Electron microscope images of samples for mineral dust particles [Nousiainen, 2009]. 11

2 Geometry of spheroidal particle shapes used in the present study..... 11

3 Comparison between the T-matrix results and their counterparts based on the approximate method for the single-scattering properties (extinction efficiency, single-scattering albedo, and asymmetry factor) of dust particles. The particle shape is assumed to be a spheroid with an aspect ratio of 1.7. The size parameter is expressed in terms of the equal volume sphere radius. 14

4 Comparison of the phase functions computed from the T-matrix method and the IGOM method for different size parameters. The size parameters are expressed in terms of the equal volume sphere radius..... 15

5 Relationships between simulated TOA apparent reflectance and Lambertian surface reflectance, for different values of AOD (τ) and refractive index (m). The vertical lines indicate the critical surface reflectance where the presence of aerosol cannot affect the TOA apparent reflectance, depending on the aerosol refractive index (i.e., aerosol absorption). 23

6 Weights for various aspect ratios derived from the best fit of the theoretically simulated phase matrix to the measured counterparts..... 27

7 Comparison between the theoretical simulation results and their counterparts based on laboratory measurements for the scattering phase matrices of feldspar samples. The solid lines indicate the simulated phase matrix based on a spheroid model. The dotted lines indicate the simulated result based on the Mie theory. 30

8 Simulated phase functions with different effective radius for spheroidal dust particles at the wavelength of 0.650 μm. For comparison, the corresponding empirical phase function used in the Deep Blue algorithm is also shown in this figure. 31

FIGURE Page

9 Relative differences of TOA intensity between the spherical and spheroidal particle shape assumption (red dots) as a function of scattering angle at the MODIS channels of 0.412 and 0.650 μm. The corresponding result between the hybrid and spheroid model is shown in blue dots. The dust AOD is 1.0 for both cases. The surface reflectances are assumed to be 0.08 and 0.30 for the 0.412 and 0.650 μm channels, respectively. 35

10 Polar plot (radius, view zenith angle; angle, relative azimuthal angle) of the TOA upward normalized radiances simulated from the spheroid, hybrid and sphere models at the MODIS 0.412 μm channel with an assumed refractive index of 1.55+0.001i. The solar zenith angle is 24°. The AOD and surface reflectance are assumed to be 1.0 and 0.08, respectively. 38

11 Contours of the relative differences between the TOA upward radiances simulated from the sphere and spheroid models, $(I_{sphere} - I_{spheroid}) / I_{spheroid} \times 100\%$, versus the solar zenith angle and view zenith angle at the MODIS 0.412 μm channel for four relative azimuthal angles. The optical depth and surface reflectance are assumed to be 1.0 and 0.08, respectively. 41

12 Simulated TOA reflectances for a dust atmosphere as a function of scattering angles for different values of dust particle size and refractive index. 42

13 Correlations between the TOA upward reflectance simulated at the MODIS 0.412 and 0.470 μm channels as a function of AOD for two different kinds of dust aerosols. The term "Dust(1.0,1.0)" indicates non-absorptive dust aerosols, whose single-scattering albedos at the 0.412 and 0.470 μm channels are both 1.0. The term "Dust(0.91,0.95)" indicates that moderately absorptive dust aerosols, whose single-scattering albedos are 0.91 and 0.95 at the 0.412 and 0.470 μm channels, respectively. 44

14 Correlations between the TOA upward reflectance simulated at the MODIS 0.412 and 0.650 μm channels (upper panel), and the TOA upward reflectance simulated at the MODIS 0.470 and 0.650 μm channels (lower panel) as functions of AOD and single-scattering albedo. The dotted and solid lines indicate the results based on the sphere and spheroid models, respectively. Different single-scattering albedo values shown in the figure are for 0.412 μm (upper panel) and 0.470 μm (lower panel). 47

FIGURE Page

15 Same plots as in Fig. 14 but for different sun-satellite geometry. 48

16 Comparison of LUTs for the two-channel retrieval technique on the basis of the scattering properties computed from different dust particle sizes..... 49

17 The comparison of LUTs for the three-channel retrieval technique on the basis of the scattering properties computed from different dust particle sizes. 50

18 Calculated land surface reflectance over the Sahara desert at 0.412, 0.470 and 0.650 μm channels by using MODIS L1 radiance and L2 cloud products..... 52

19 MODIS RGB image over West Africa on March 2, 2003. The area indicated by the small red box is used to retrieve dust AOD in the present sensitivity study..... 54

20 Upper panels: the retrieved dust AOD based on the spheroid and sphere models. Middle left panel: retrieved dust AOD based on the sphere model versus those based on the spheroid model. Middle right panel: the histogram of retrieved dust AOD based on spheroid and sphere models. Lower left panel: the relative differences of the phase functions. Lower right panel: the relative differences of the retrieved AOD. 55

21 MODIS RGB image on May 27, 2008, showing a dust plume over North Asia. The area indicated by the small red box is used to retrieve dust AOD in the present sensitive study. 58

22 Comparisons of retrieved dust AOD between the spheroidal and spherical particle shape assumptions. The upper panel shows results for the spheroidal particle shape assumption, the middle panel shows results for the spherical particle shape assumption, and the lower panel shows the corresponding scattering angles. 59

23 The scatter plots of retrieved dust AOD based on the spherical particle shape assumption versus the corresponding results based on the spheroidal particle shape assumption, for different scattering angles..... 60

24 Upper panel: MODIS RGB image on March 27, 2004 shows Asian dust storm over Northern China. Lower panel: MODIS NDDI image shows the differences between mineral dust aerosols and clouds. 66

FIGURE Page

25 Upper panel: brightness temperature (in K) image of MODIS 11 μm band over Northern China on March 27, 2004. Lower panel: the dust detection results (NDDI > 0.28 and BT11 < 275 K). 67

26 Shown are the brightness temperature (in K) difference $BT_{8.5} - BT_{11}$ (upper panel) and $BT_{11} - BT_{12}$ (low panel) for a dust storm outbreak as indicated in the upper panel of Fig. 24. 68

27 Same plots as in Fig. 26 but for a dust storm over oceans as indicated in Fig. 19. 69

28 Comparisons of the phase matrix calculated at the wavelength of 0.412 μm for randomly oriented droxtal ice crystals and spheroidal mineral dust aerosols. 72

29 The relative differences of the TOA upward reflectances between the dust only and dust plus thin cirrus atmosphere, as a function of satellite view zenith angles for different values of dust optical depth and surface reflectance. The surface reflectances for the left and right panels are 0.04 and 0.08, respectively. 75

30 Polar plots of the TOA upward reflectances for the dust only and dust plus thin cirrus atmosphere. 76

31 Calculated surface reflectance database at 0.412, 0.470 and 0.65 μm channels over North Asia. 77

32 Same plots as in Fig. 13 but for the dust only and dust plus thin cirrus atmosphere. In addition, the sun-satellite geometry associated with Fig. 13 and Fig. 32 is also different. Upper panel has relative azimuthal angle (ϕ) equal to 132°, while lower panel has ϕ equal to 72°. The optical depth and effective diameter for thin cirrus clouds are 0.3 and 20 μm, respectively. 79

33 Similar to Fig. 14 but for the comparison between the dust only and dust plus thin cirrus atmosphere. The more horizontal curves represent different values of single-scattering albedo. 80

34 Upper panel: MODIS RGB image on May 27, 2008 shows Asian dust storm over Mongolian regions. Lower panel: MODIS NDDI image shows the differences between mineral dust aerosols and clouds. 83

FIGURE Page

35 Retrieved dust AOD corresponding to LUT based on the dust only atmosphere (upper panel) and LUT based on the dust plus thin cirrus atmosphere (lower panel)..... 84

36 Upper panel: the histogram of retrieved dust AOD based on the LUTs for the dust only and dust plus thin cirrus atmosphere, respectively. Lower panel: the absolute errors of the retrieved dust AOD. 85

37 Real and imaginary parts of the refractive index for mineral dust aerosols [d'Almeida et al., 1991]..... 90

38 The comparison of bulk scattering properties (mean extinction efficiency, single-scattering albedo and asymmetry factor) for spherical and nonspherical mineral dust particles in the spectral region ranging from 0.25 to 4.0 μm. The effective radius and effective variance for dust aerosols are assumed to be 1.0 μm and 1.0, respectively. 91

39 Scatter plots of CERES SSF TOA SW upward flux as a function of SSF MODIS aerosol optical depth (0.55 μm) for different solar zenith angles. The corresponding linear regression line is also showed. 94

40 Simulated clear sky SW albedos at the top of atmosphere as a function of solar zenith angles at three different wind conditions by using Fu-Liou model. The corresponding results (open circles) inferred from CERES are also shown. 95

41 (Upper panel) TOA SW fluxes for spheroidal dust versus TOA SW fluxes for spherical dust over dark surface. (Lower panel) Simulated SW dust radiative forcing with spheroidal and spherical particle shape assumptions, as a function of dust optical depths for different solar zenith angles. 96

42 TOA SW dust radiative forcing over dark surface with a surface albedo of 0.05, as a function of solar zenith angles for two different optical depths. The red (blue) error bars represent the dust radiative forcing uncertainties due to 10% (5%) errors in optical depth retrievals. 100

43 Same plots as in Fig. 42 but for a different surface albedo. 100

44 Spatial distribution of retrieved dust AOD based on the spheroidal and spherical particle shape assumptions and the corresponding TOA instantaneous SWRF for different surface albedos. 101

FIGURE Page

45 Left panel: the scatter plots of TOA SW radiative forcing for spherical dust versus the counterpart for spheroidal dust for different scattering angles. Right panel: the corresponding relative differences for TOA SW radiative forcing. 103

LIST OF TABLES

TABLE Page

1 Comparisons of the single-scattering albedos computed from the spheroid and sphere models at three MODIS channels used in the Deep Blue aerosol retrieval algorithm. The effective radius r_e and effective variance v_e for mineral dust aerosols are 1.0 μm and 1.0, respectively. 33

2 Comparisons of the single-scattering albedos computed from different particle sizes for spheroidal particle shape assumption at three MODIS channels used in the Deep Blue aerosol retrieval algorithm..... 34

1. INTRODUCTION

1.1 Mineral dust and its role in climate

Mineral dust, a term used to indicate the suspended atmospheric mineral aerosol particles [Nousiainen, 2009], is a major component of atmospheric aerosols. Mineral dust aerosols originating from arid and semi-arid regions such as deserts can transport a vast distance to impact the climate system on a global scale. It has been recognized that the climate effect induced by mineral dust aerosols through regulation of the radiative energy budget is of increasing interest [King et al., 1999; Haywood and Bougher, 2000; Sokolik et al., 2001; Kaufman et al., 2002]. Mineral dust aerosols, with optical properties varying widely [Sokolik et al., 1999], can reduce the incoming solar radiation reaching the dark surface by scattering, leading to negative radiative forcing. In the meanwhile, mineral dust aerosols absorb solar and infrared radiation, leading to positive radiative forcing and further enhancing the greenhouse warming effect. Here, the radiative forcing is defined as the change in net radiation due to the presence of mineral dust aerosols. These two aforementioned opposing mechanisms are called dust direct radiative effects. Indirect effects mean mineral dust aerosols are effective in modifying cloud formation and physical properties, and precipitation amount by acting as cloud condensation nuclei.

1.2 Satellite-based remote sensing of mineral dust aerosols

Global characteristics of dust aerosol properties are of significant interests for climate

---

This dissertation follows the style of *Journal of Geophysical Research*.

studies. Consequently, satellite remote sensing techniques are required to retrieve the physical and optical properties of mineral dust aerosols on a global scale. Particularly remarkable are the new generation of Earth observing satellite (EOS) passive sensors such as the Multi-angle Imaging spectroradiometer (MISR) [Martonchik and Diner, 1992], the Moderate Resolution Imaging Spectroradiometer (MODIS) [King et al., 1992] and Polarization and Directionality of the Earth's Reflectance (POLDER) [Deuze et al., 1999]. These sensors, suitable for aerosol retrievals from space, provide radiance measurements at the top of the atmosphere with multiple visible/near-infrared channels (MISR, MODIS and POLDER), multiple view angles (MISR and POLDER), and polarized information reflected from the Earth's surface and its atmosphere (POLDER). In the framework of MODIS, algorithms have been developed to characterize dust aerosol properties, with emphasis on dust aerosol optical depth (AOD), including the traditional MODIS aerosol retrieval algorithm [Remer et al., 2005] and the Deep Blue algorithm [Hsu et al., 2004, 2006]. The traditional MODIS aerosol retrieval algorithm over land is applicable to observations over darker surfaces, utilizing the surface reflectance correlation between the visible and near-IR channels. However, this approach fails over most desert regions since the high surface reflectivity dominates the satellite signal over these dust source regions. The Deep Blue algorithm is specially designed to solve the problem by including measurements from the deep blue channel (the 0.412-μm channel for MODIS), on which the surface contribution to the satellite measurements is relatively small compared with the aerosol contribution.

Despite the significant progress made toward inferring the microphysical and optical properties of aerosols from satellite observations over dark and bright surfaces [Remer et

al., 2005; Hsu et al., 2004, 2006], reliable retrieval of the whole set of aerosol properties (e.g., particle size and shape, optical depth and complex refractive index) from satellite measurements is still a challenging task. Various simplified aerosol models, which play a vital role in aerosol retrievals, are often prescribed *a priori* for developing an efficient satellite aerosol retrieval algorithm. And, it has been realized that the quality of retrieving aerosol optical properties based on satellite measured radiance data critically depends on the accuracy of the scattering properties adopted in the aerosol models [Wang and Gordon, 1994].

A special issue posed by mineral dust aerosols is their predominantly nonspherical particle shapes [Koren et al., 2001; Okada et al., 2001; Reid et al., 2003a], which means that the Mie theory is not applicable for computing their scattering properties. Indeed, several laboratory experiments [West et al., 1997; Volten et al., 2001; Curtis et al., 2008] revealed that the particle shapes of mineral dust are highly irregular and the scattering properties of realistic mineral dust aerosols are significantly different from those of equivalent spherical particles. Neglecting the nonsphericity of mineral dust particles may lead to substantial errors in theoretical radiance simulation and hence in retrieving dust properties from satellite observations [Kahnert et al., 2005, 2007; Mishchenko et al., 2003; Zhao et al., 2003]. Thus, more focus has been put on treating the scattering properties for nonspherical dust particles based on scattering-computational methods, since in situ measurements of the scattering properties for mineral dust aerosols are often hindered due to the technical constraints.

While mineral dust aerosols are uniquely and irregularly shaped, a spheroidal particle shape assumption has been widely employed in the simulation of scattering properties for

nonspherical dust particles [Mishchenko et al., 1997; Kahnert, 2004; Dubovik et al., 2002a, 2006; Yang et al., 2007] and in relevant remote sensing applications [Eck et al., 2005; Levy et al., 2007]. In order to account for the nonspherical effect of dust particles, the traditional MODIS aerosol retrieval algorithm assumes dust aerosols to be a mixture of randomly oriented spheroidal particles [Remer et al., 2005], and the Deep Blue algorithm relies on a hybrid approach which is based on an empirical phase function (representative of the bulk scattering properties for nonspherical dust aerosols) and the spherical particle shape assumption for the other phase matrix elements [Hsu et al., 2004, 2006].

Most existing scattering-computational methods, such as the discrete dipole approximation (DDA) method [Purcell and Pennypacker, 1973; Draine and Flatau, 1994] and the finite-difference time domain (FDTD) method [Yee, 1966; Yang et al., 2000], require substantial computational resources and are not practical for coarse-mode dust particles at visible wavelengths (i.e., in the case of moderate and large size parameters), although these methods are flexible for complicated particle geometries. To date, the T-matrix code developed by Mishchenko and Travis [1994] for rotationally symmetric particles remains a computationally efficient tool for simulating the optical properties of nonspherical dust particles for small and moderate size parameters. However, even for spheroidal particles, there is no single computational code that can cover size parameters ranging from the Rayleigh to geometric optics regimes. To overcome this difficulty, Dubovik et al. [2002a, 2006] used a combination of the T-matrix method and an improved geometric optics (IGOM) method [Yang and Liou, 1996] to solve for the single-scattering properties of nonspherical mineral dust aerosol particles that are

assumed to be spheroids. Most recently, Yang et al. [2007] further improved the IGOM method by accounting for some processes in the physical optics domain, such as the edge and above-/below-edge effects [Nussenzveig and Wiscombe, 1980] on the computation of the extinction and absorption efficiencies, respectively. Note that some attempts have been made to simulate the scattering properties of nonspherical mineral dust with more complicated particle shapes [Kalashnikova and Sokolik, 2002; Kalashnikova et al., 2005; Bi et al., 2008, 2010].

Since cloud contamination is an essential issue and can lead to large errors when retrieving aerosols from space [Mishchenko et al., 1999], a cloud mask must be used to eliminate the problem of cloud contamination prior to aerosol retrievals [Remer et al., 2005]. Several primary techniques have been developed to screen out cloud-contaminated pixels for aerosol retrievals from MODIS data [Kaufman et al., 1997; Chu et al., 2002; Martins et al., 2002; Remer et al., 2002]. However, these techniques sometimes fail to identify thin cirrus clouds, which have comparable optical depths with aerosols, and the detection of thin cirrus still remains a major problem [Gao et al., 2002; Roskovensky and Liou, 2003]. In addition, thin cirrus clouds are ubiquitous in nature and can have a relatively long lifetime [McFarquhar et al., 2000]. As a result, the thin cirrus cloud contamination problem sometimes still exists in the retrieved aerosol products although it is claimed that thin cirrus contaminated pixels are used for aerosol retrievals [Gao et al., 2002]. It would be satisfying to be able to retrieve both atmospheric aerosols and thin cirrus properties simultaneously when they coexist. However, it is very different to separate the reflected sunlight signal by both types of particles. To obtain reliable aerosol information, the effect of thin cirrus on aerosol retrievals must be accurately taken into

account. It is important to note that simultaneous retrievals of aerosols and thin cirrus optical depths can only be attempted over oceans, for some case studies, by assuming that the aerosol lies below thin cirrus clouds [Roskovensky and Liou, 2005].

1.3 Direct radiative forcing by mineral dust aerosols

Substantial progress has been made in our understanding of the dust direct radiative effect on the climate system by dust transport and general circulation models embedded with radiative transfer codes [Tegen et al., 1996; Myhre and Stordal, 2001]; by sensitivity studies using stand-alone radiative transfer simulations [Liao and Seinfeld, 1998]; and by satellite-based assessment of dust radiative effect [Zhang and Christopher, 2003; Li et al., 2004; Christopher and Jones, 2008]. In these studies, it is not far-fetched to say that dust optical properties are crucial to its direct radiative forcing calculations. The magnitude of dust direct radiative forcing, which is about $0.7 \pm 0.2 \ \ Wm^{-2}$ for global cloud-free oceans [Christopher and Jones, 2008], depends on dust optical depth, particle size distribution, mineralogical composition, cloud cover as well as the albedo of the underlying surface. The shortwave direct radiative forcing for mineral dust can be negative or positive, while the corresponding longwave direct radiative forcing is always positive and has the same order of magnitude as its shortwave counterpart. However, there are still some discrepancies related to the importance of dust particle shapes when radiative transfer models are employed to calculate the direct radiative forcing by mineral dust. As pointed out by earlier investigations, dust particle shape assumption is not a crucial factor for radiative fluxes but for radiances. That is to say, dust particle shapes would be a significant factor for dust retrievals, but not for radiative forcing calculations. The effect

of dust particle shapes on the accuracy of dust radiative forcing calculations is twofold. First, the shapes of mineral dust particles become less important in radiative forcing calculations if the dust optical thickness is already known [Mishchenko et al., 1995; Fu et al., 2009], resulting in the Mie theory being generally employed in the calculation of dust radiative forcing [Liao and Seinfeld, 1998; Myhre and Stordal, 2001]. Second, it is important to emphasize that the poor description of mineral dust shapes may lead to the large errors in estimates of direct radiative forcing by dust [Pilinis and Li, 1998; Kahnert et al., 2005, 2007]. Therefore, further discussion about the effect of particle shapes on estimates of dust radiative forcing is necessary and potentially important.

1.4 Organization of the dissertation

With the help of existing scattering-computational methods, radiative transfer models and aerosol retrieval algorithms, the research presented here is intended to study the effects of particle nonsphericity and thin cirrus clouds on MODIS dust optical depth retrievals. Furthermore, the effect of particle shapes on dust direct radiative forcing calculations is also discussed. The rest of this dissertation is organized as follows:

A general methodology, coupled with a brief introduction of several key science concepts basic to the current research, is detailed in section 2. In section 3, the simulated scattering and radiative properties for nonspherical mineral dust aerosols based on spheroidal particle shape assumption are investigated and compared with the counterparts for spherical particles. The effect of particle nonsphericity on dust AOD retrievals is quantitatively described in this section. Section 4 discusses the effect of thin cirrus clouds on the retrieved dust AOD. Some preliminary results related to the effect of particle

nonsphericity on dust radiative forcing calculations are presented in section 5. Finally, the summary and conclusion are discussed in section 6.

2. METHODOLOGY

2.1 Objective

The objectives of this research presented here are to:

- Update lookup tables (LUTs) for the Deep Blue aerosol retrieval algorithm with existing scattering-computational methods.
- Demonstrate the feasibility of the hybrid approach which has already been employed in Deep Blue algorithm, based on the spheroidal particle shape assumption for the phase function and the spherical particle shape assumption for the other phase matrix elements.
- Determine the effects of particle nonsphericity and thin cirrus clouds on dust optical depth retrievals based on the principle of Deep Blue aerosol retrieval algorithm.
- Determine the effect of particle shapes on direct radiative forcing calculations for mineral dust.

A brief introduction of several key methods and concepts, which constitute the foundation for the current research, is presented here as follows.

2.2 Methods for scattering simulations

As mentioned above, neglecting the particle nonsphericity of mineral dust aerosols may lead to substantial errors in simulating their scattering and radiative properties, and hence in remote sensing applications. As a consequence, there is a pressing need to

account for particle nonsphericity in computing the scattering properties of mineral dust aerosols in various applications.

Fig. 1 shows some examples of particle shapes for mineral dust collected in Northern Sahara. It clearly indicates that the shapes of mineral dust aerosols are not spherical, and seldom even quasi-spherical. While mineral dust aerosol particles in the atmosphere usually have quite complicated morphologies, in order to compute their scattering properties, it is a reasonable approximation to assume an ensemble of dust particles to be a mixture of randomly oriented spheroids with a shape (aspect ratio) distribution. One reason is that the phase functions simulated by the spheroidal particle shape assumption closely resemble those measured for realistic dust particles [Mishchenko et al., 1997]. Furthermore, the spheroid model has the ability to systematically mimic the spectral variations of dust phase matrix, extinction coefficient, and single-scattering albedo [Dubovik et al. 2002a, 2006]. Here the ratio of a spheroidal shape is defined in terms of the ratio of the rotational-axis length (a) to the equatorial-axis length (b) of the particle (hereafter, indicated as a/b), as indicated in Fig. 2. Note that $a/b>1$ and $a/b<1$ define prolate and oblate spheroids, respectively. The effective radius r_e for individual spheroidal particle is defined following the work of Foot [1998] and Grenfell and Warren [1999] in the form of

$$r_e = \frac{3}{4}\frac{V}{A} \tag{1}$$

where V and A are the volume and projected area for the spheroid under random orientation condition. The volumes of a spheroid is given as following:

$$V = \frac{4}{3}\pi b^2 a\,. \tag{2}$$

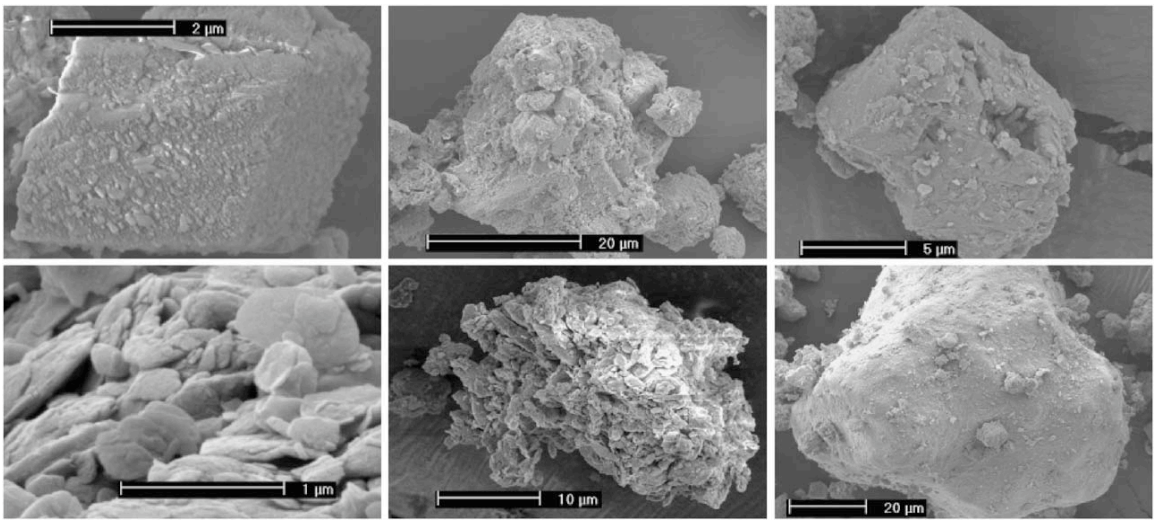

Fig. 1 Electron microscope images of samples for mineral dust particles [Nousiainen, 2009].

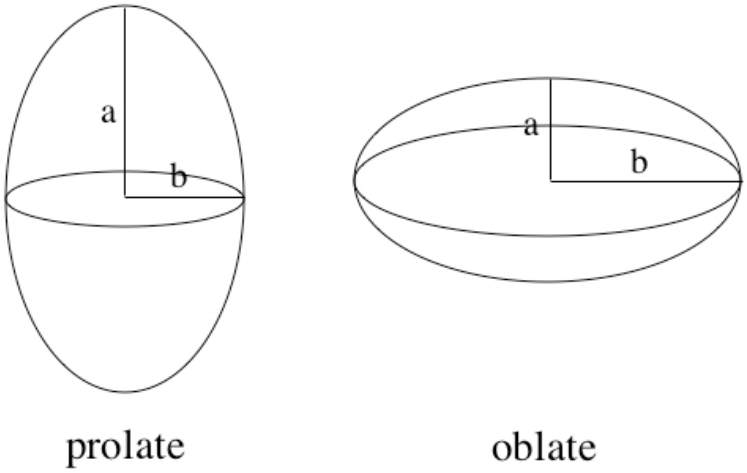

Fig. 2 Geometry of spheroidal particle shapes used in the present study.

According to the work of Vouk [1948], the project area (A) is one quarter of the surface area (S) for convex particles. The surface area of a spheroid, following Beyer [1981], can be formulated as follows:

$$S = \begin{cases} 2\pi b^2 + \pi \dfrac{a^2}{\varepsilon} \ln \dfrac{1+\varepsilon}{1-\varepsilon} & \text{for oblate spheroid,} \\ 2\pi b^2 + 2\pi \dfrac{ab}{\varepsilon} \sin^{-1} \varepsilon & \text{for prolate spheroid,} \end{cases} \tag{3}$$

where ε is the eccentricity of the spheroid.

To compute the single-scattering properties of individual mineral dust aerosols, we follow the methodology suggested by Dubovik et al. [2002a, 2006] to simulate the scattering properties of individual dust particles that are assumed to be spheroids. Specifically, we use the T-matrix method [Mishchenko and Travis, 1994] to calculate the scattering properties of small and moderate size particles and an approximate method based on improved geometric optics method (IGOM) [Yang et al., 2007] for large size particles. The technical details regarding the combination of the two methods are reported in Dubovik et al. [2006] and Yang et al. [2007]. Note that the IGOM used in Dubovik et al. [2006] is a version reported in Yang and Liou [1996]. The updated version of IGOM [Yang et al., 2007] used in the present study accounts for the edge effect for the extinction efficiency and the above-/below-edge effects for the absorption efficiency. The detailed explanation regarding the edge effects are reported in Yang et al. [2007] and references cited therein. Here, the edge effect is defined as the nonzero contribution of the penumbra region to the extinction efficiency, which is not taken into account in the conventional geometric optics method (CGOM). Thus, the total extinction efficiency $Q_e(a,b,k,m)$ is given by

$$Q_e(a,b,k,m) = Q_{e,IGOM}(a,b,k,m) + \overline{Q}_{e,edge}(a,b,k), \tag{4}$$

where $k = 2\pi/\lambda$ is the wavenumber, λ is the wavelength, m is the complex refractive index, $Q_{e,IGOM}(a,b,k,m)$ is the extinction efficiency computed from the IGOM, and $\overline{Q}_{e,edge}(a,b,k)$ is the mean edge contribution to the extinction efficiency. Similar to the computation of the extinction efficiency, the absorption efficiency for randomly oriented spheroids $Q_a(a,b,k,m)$ is defined as

$$Q_a(a,b,k,m) = Q_{a,IGOM}(a,b,k,m) + \left[Q_{a,a.e.}(r_e,k,m) + Q_{a,b.e.}(r_e,k,m)\right](4\pi r_e^{\,2}/S), \qquad (5)$$

where $Q_{a,IGOM}(a,b,k,m)$ is the absorption efficiency computed from the IGOM, $Q_{a,a.e.}(r_e,k,m)$ and $Q_{a,b.e.}(r_e,k,m)$ are referred to as the above-edge and below-edge contribution for spheres.

Fig. 3 shows the extinction efficiency, single-scattering albedo, and asymmetry factor of randomly oriented spheroids (with an aspect ratio of 1.7), as a function of particle size parameters. The refractive index of dust particle is assumed to be 1.53+0.008i. The size parameters are defined in terms of the equal volume sphere radius. The T-matrix method is applied to particle size parameters ranging from 0.5 to 50 (blue lines), and the approximate method for particle size parameters ranging from 23 to 800 (red lines). Overall, the results based on the approximate method agree well with the T-matrix solutions at moderate size particles. Fig. 4 shows the comparison of the phase functions of randomly oriented spheroids (with an aspect ratio of 1.7) for different particle size parameters and refractive indices. Obviously, the IGOM solutions agree well with the T-matrix counterparts, particularly for large size parameters and absorptive dust particles.

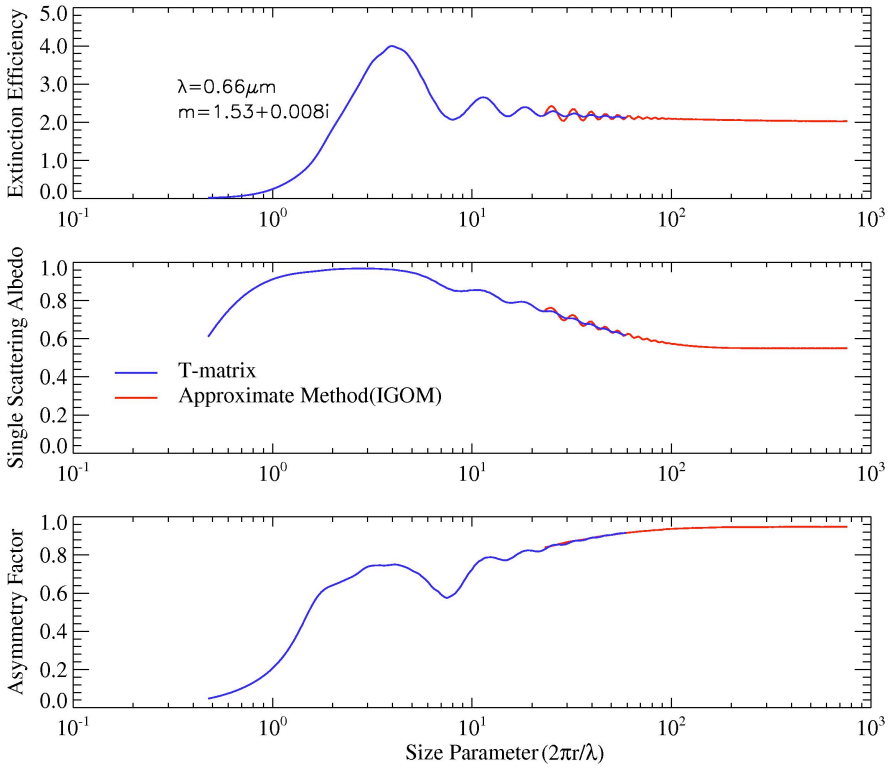

Fig. 3 Comparison between the T-matrix results and their counterparts based on the approximate method for the single-scattering properties (extinction efficiency, single-scattering albedo, and asymmetry factor) of dust particles. The particle shape is assumed to be a spheroid with an aspect ratio of 1.7. The size parameter is expressed in terms of the equal volume sphere radius.

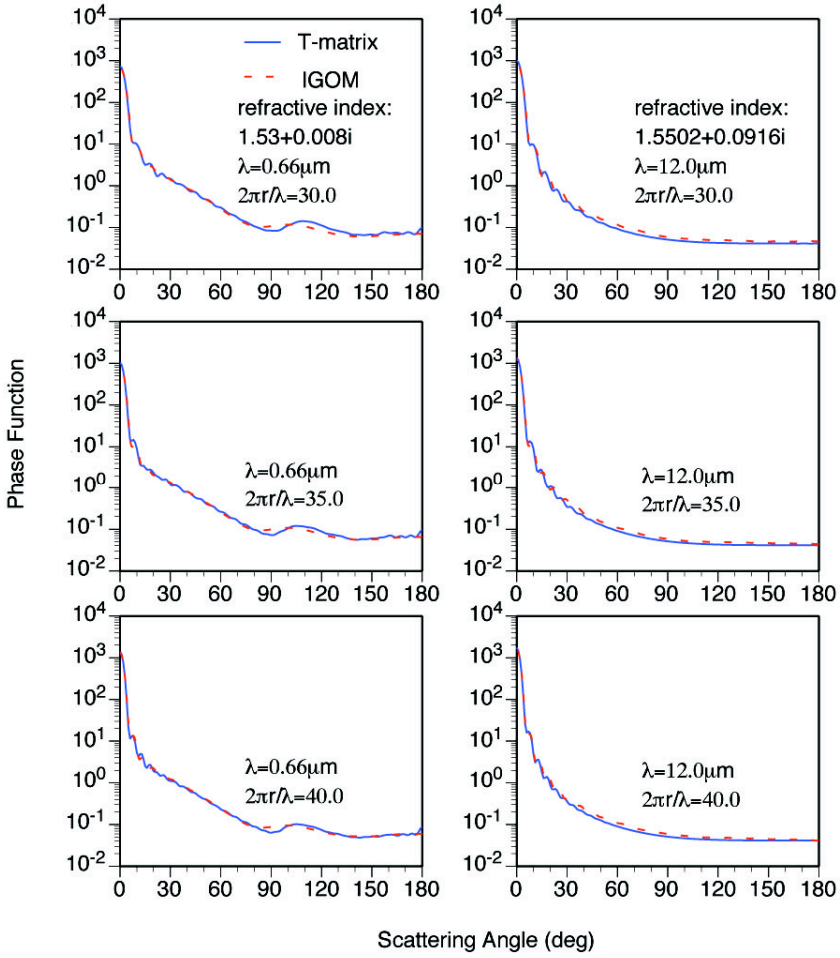

Fig. 4 Comparison of the phase functions computed from the T-matrix method and the IGOM method for different size parameters. The size parameters are expressed in terms of the equal volume sphere radius.

Without considering the particle shape distribution, the bulk scattering properties of mineral dust can be derived by averaging the single-scattering properties over the particle size distribution as follows:

$$Q_{e(ave)} = \frac{\int_r Q_e(r) A(r) \frac{dn(r)}{d\ln r} d\ln r}{\int_r A(r) \frac{dn(r)}{d\ln r} d\ln r}, \tag{6}$$

$$Q_{s(ave)} = \frac{\int_r Q_s(r) A(r) \frac{dn(r)}{d\ln r} d\ln r}{\int_r A(r) \frac{dn(r)}{d\ln r} d\ln r}, \tag{7}$$

$$\omega_{(ave)} = \frac{Q_{s(ave)}}{Q_{e(ave)}}, \tag{8}$$

$$P_{11(ave)} = \frac{\int_r P_{11}(r) Q_s(r) A(r) \frac{dn(r)}{d\ln r} d\ln r}{\int_r Q_s(r) A(r) \frac{dn(r)}{d\ln r} d\ln r}, \tag{9}$$

where $Q_{e(ave)}$, $Q_{s(ave)}$, $\omega_{(ave)}$, and $P_{11(ave)}$ are averaged extinction, scattering efficiency, single-scattering albedo, and phase function, respectively. The effective radius r_e for spheroidal particles with particle size distribution is given by

$$r_e = \frac{3}{4} \frac{\int_t V(r) \frac{dn(r)}{d\ln r} d\ln r}{\int_r A(r) \frac{dn(r)}{d\ln r} d\ln r}, \tag{10}$$

where $V(r)$ and $A(r)$ are the volume and projected area for individual dust particle with equal volume sphere radius of r, $\frac{dn(r)}{d\ln r}$ is the particle size distribution. The effective variance v_e [Hansen and Travis, 1974] is defined as

$$v_e = \sqrt{\frac{\int_r (r - r_e)^2 \pi r^2 \frac{dn(r)}{d\ln r} d\ln r}{r_e^2 \int_r \pi r^2 \frac{dn(r)}{d\ln r} d\ln r}}. \tag{11}$$

2.3 Radiative transfer simulations

2.3.1 Adding-double radiative transfer code

As demonstrated by Mishchenko et al. [1994] and Levy et al. [2004], neglecting polarization may lead to errors in the simulated spectral radiances at the top of a Rayleigh-scattering atmosphere, particularly, at short wavelengths. For example, the differences of the simulated blue channel (0.47 μm) TOA reflectance between polarized and unpolarized radiative transfer model can reach up to 0.03, which may lead to a dust AOD retrieval error of 0.3 [Levy et al., 2004]. This situation becomes even worse for the deep blue channel (0.412 μm), which has a relative larger Rayleigh-scattering optical depth than that for the blue channel. As a result, a polarized radiative transfer code (Adding/Doubling code) developed by De Haan et al. [1987] based on the adding-doubling method is used to address the transfer of polarized radiation for aerosol retrievals. In this radiative transfer code, the well known Stokes vectors, as denoted as I, Q, U, V, are included and a radiation beam can be completely characterized by its intensity and state of polarization. Choosing axes r and l, and $r \times l$ in the direction of beam propagation, we can define the Stokes vectors as

$$\mathbf{I} = E_l E_l^* + E_r E_r^*$$

$$\mathbf{Q} = E_l E_l^* - E_r E_r^*$$

$$\mathbf{U} = E_l E_r^* + E_r E_l^*$$

$$\mathbf{V} = i(E_l E_r^* - E_r E_l^*). \qquad (12)$$

The electric field component, E_l and E_r, define the electric field. The atmosphere is usually assumed to consist of a number of plane-parallel layers, each of which is specified in terms of the single-scattering albedo, optical depth and scattering matrix.

Note that the scattering matrix for randomly oriented spheroidal particles has a block-diagonal form with six independent nonzero elements, given by

$$P(\Theta)=\begin{bmatrix} P_{11}(\Theta) & P_{12}(\Theta) & 0 & 0 \\ P_{12}(\Theta) & P_{22}(\Theta) & 0 & 0 \\ 0 & 0 & P_{33}(\Theta) & P_{34}(\Theta) \\ 0 & 0 & -P_{34}(\Theta) & P_{44}(\Theta) \end{bmatrix}, \tag{13}$$

where Θ is scattering angle. For spherical particles, the scattering matrix has only four independent elements, since $P_{11}(\Theta)=P_{22}(\Theta)$ and $P_{33}(\Theta)=P_{44}(\Theta)$. Here, the scattering plane, which contains the incident beam and scattered beam, acts as a plane of reference for the scattering matrix. The radiance associated with a radiation field is largely determined by the (1, 1)-element of the scattering matrix, i.e., the phase function. Scattering matrix of mineral dust aerosols plays an important role in radiative transfer simulations, since it contains all polarizing properties of dust particles and is indispensable for accurate calculations of multiple scattering by mineral dust aerosols in an atmosphere [Volten et al., 2001]. The expansion coefficients of the elements in the scattering matrix in generalized spherical functions are needed as input to the polarized radiative transfer code. The polarized radiative transfer equation is defined as

$$\mu\frac{d\mathbf{I}(\tau,\mu,\phi)}{d\tau}=\mathbf{I}(\tau,\mu,\phi)-\mathbf{J}(\tau,\mu,\phi)\ , \tag{14}$$

where $\mathbf{I}$ is the stokes vectors at a layer with an optical depth of τ , $\mu=\cos\theta$, the angle θ is measured from the positive z-direction in the right-handed Cartesian coordinate system. The azimuthal angle, ϕ, is measured from a plane including the z-axis and x-axis. The source term $\mathbf{J}(\tau,\mu,\phi)$ is defined as

$$\mathbf{J}(\tau,\mu,\phi)=\frac{\omega}{4\pi}\int_0^{2\pi}\int_{-1}^{1}\mathbf{Z}(\mu,\phi;\mu',\phi')\mathbf{I}(\tau,\mu',\phi')d\mu'\phi'\ , \tag{15}$$

where ω is the single-scattering albedo. The phase matrix is defined as

$$\mathbf{Z}(\mu,\phi;\mu',\phi') = L(\pi-\sigma_2)P(\Theta)L(-\sigma_1), \tag{16}$$

where the scattering plane make the angle σ_1 with the incident meridian plane and the angle σ_2 with the scattered meridian plane. The rotation matrix haves the general form

$$L(-\sigma) = \begin{pmatrix} 1 & 0 & 0 & 0 \\ 0 & \cos 2\sigma & -\sin 2\sigma & 0 \\ 0 & \sin 2\sigma & \cos 2\sigma & 0 \\ 0 & 0 & 0 & 1 \end{pmatrix}. \tag{17}$$

Now suppose we have two layers, one placed on top of the other. If the reflection and transmission matrices of the upper ($\mathbf{R_1}, \mathbf{T_1}$) and lower layer ($\mathbf{R_2}, \mathbf{T_2}$) are known, then the reflection and transmission matrices of the combined layer ($\mathbf{R_c}, \mathbf{T_c}$) can be determined by using adding equations. The optical depth of the combined layer is the sum of each layer. The adding equations can be defined as follows

$$\mathbf{Q_1} = \mathbf{R_2}\mathbf{R_1}^*$$
$$\mathbf{S} = \mathbf{Q_1}(\mathbf{1}-\mathbf{Q_1})^{-1}$$
$$\mathbf{D} = \mathbf{T_1} + \mathbf{S}\mathbf{T_1} + \mathbf{S}\exp(-\frac{\tau_1}{\mu_0})$$
$$\mathbf{U} = \mathbf{R_2}\mathbf{D} + \mathbf{R_2}\exp(-\frac{\tau_1}{\mu_0})$$
$$\mathbf{R_c} = \mathbf{R_1} + \exp(-\frac{\tau_1}{\mu})\mathbf{U} + \mathbf{T_1}^*\mathbf{U}$$
$$\mathbf{T_c} = \exp(-\frac{\tau_2}{\mu})\mathbf{D} + \mathbf{T_2}\exp(-\frac{\tau_1}{\mu_0}) + \mathbf{T_2}\mathbf{D}$$

$$\mathbf{R_2}\mathbf{R_1}^* = \frac{1}{\pi}\int_0^{2\pi}\int_0^1 \mathbf{R_1}^*(\mu,\phi;\mu',\phi')\mathbf{R_2}(\mu',\phi';\mu_0,\phi_0)\mu' d\mu' d\phi' \tag{18}$$

Here, $\mathbf{R_1}^*$ and $\mathbf{T_1}^*$ means the transmission and reflection matrices for light incident form below.

If these two layers are identically homogeneous, and have the same optical depth, then the doubling method is applied. For the adding-double method, each plane-parallel layer is generally divided into many optically thin homogeneous layers, whose refection and transmission matrices are approximated by the following equations

$$R(\mu,\phi;\mu',\phi') = \frac{\omega}{4(\mu+\mu')}\left\{1-\exp\left[-\tau^*(\frac{1}{\mu}+\frac{1}{\mu'})\right]\right\}\mathbf{Z}(\mu,\phi;-\mu',\phi') \qquad (19)$$

$$T(\mu,\phi;\mu',\phi') = \frac{\omega}{4(\mu'-\mu)}\left[\exp(-\frac{\tau^*}{\mu'})-\exp(-\frac{\tau^*}{\mu})\right]\mathbf{Z}(\mu,\phi;\mu',\phi') \quad \text{if } \mu' \neq \mu \qquad (20)$$

$$T(\mu,\phi;\mu',\phi') = \frac{\omega\tau^*}{4\mu'^2}\exp(-\frac{\tau^*}{\mu'})\mathbf{Z}(\mu,\phi;\mu',\phi') \quad \text{if } \mu' = \mu \qquad (21)$$

2.3.2 Fu-Liou radiative transfer code

For radiative forcing calculations, the radiative transfer code originally developed by Fu and Liou [1993] is used to calculate the hemispherical flux at the top of the atmosphere. The model is a delta-four stream radiative transfer code with six solar spectral bands (0.2-0.7, 0.7-1.3, 1.3-1.9, 1.9-2.5, 2.5-3.5, and 3.5-4.0 μm) for the shortwave flux calculations and twelve infrared spectral bands (2200-1900, 1900-1700, 1700-1400, 1400-1250, 1250-1100, 1100-980, 980-800, 800-670, 670-540, 540-400, 400-280, and 280-0 cm^{-1}) for the longwave flux calculations. The model accounts for molecular Rayleigh scattering, various gas absorption, as well as absorption and scattering due to aerosols and clouds. Since aerosol radiative forcing is strongly influenced by surface albedo due to the complicated multiple reflections between the aerosol layer and the surface layer, the dependence of broadband albedo on solar zenith angle over ocean is taken into account by using a lookup table (LUT) generated by a coupled atmosphere-ocean radiative transfer model [Jin and Stamnes, 2004]. Over land,

the surface is assumed to be Lambertian and homogeneous, and have the same surface albedo for each spectral band in the present sensitivity study.

2.4 Aerosol retrieval algorithm

The desert areas are the major source regions for mineral dust aerosols. The problem of retrieving dust properties over these bright surfaces using visible channels is illustrated in Fig. 5, which shows the simulated apparent reflectances at the top of the atmosphere (TOA) as a function of surface reflectances for dust aerosols with different refractive index (aerosol absorption). The TOA apparent reflectances measured by satellite are a mixture of the contribution from the light scattered solely by atmosphere, and the contribution from the transmitted radiance after multiple reflections between surface and atmosphere. If the dust aerosol absorbs sunlight, its presence would darken the reflectance over the high-reflecting surface and brighten the reflectance over dark surface. The critical surface reflectance, depending on the aerosol absorption, is defined as the reflectance at which the presence of aerosol will not change the TOA apparent reflectance. On the other hand, for non-absorptive dust aerosol, its presence would always brighten the underlying surface. And, the TOA apparent reflectance for non-absorptive dust aerosol is not sensitive to the change of AOD over bright surfaces. The retrievals of aerosol properties over the high-reflecting surface may contain large errors.

To investigate and quantify the nonspherical effect of dust particles on the retrieved dust AOD, in the present research, we develop an unsophisticated aerosol retrieval algorithm based on the fundamental principle of the Deep Blue aerosol retrieval algorithm that was specially developed to retrieve aerosol properties over bright-

reflecting surfaces [Hsu et al., 2004, 2006]. The Deep Blue aerosol retrieval method is a robust approach for aerosol retrievals over desert regions where the dominant aerosol type is mineral dust. The Deep Blue approach for retrieving pure mineral dust can be summarized as follows. A two-channel (0.412 and 0.470 μm) retrieval algorithm is first employed to derive the dust aerosol properties (AOD and single-scattering albedos). If the retrieved dust AOD based on the two-channel technique exceeds 0.7 (heavy dust aerosol loading condition), a three-channel (0.412, 0.470 and 0.650 μm) technique is applied to retrieve the dust aerosol properties. The commonly used LUT technique is employed for the retrieval on the basis of the best match between the simulated reflectance and their measured counterparts at the MODIS 0.412, 0.470 and 0.650 μm channels. It is assumed, in this algorithm, that there is almost no absorption for mineral dust particles at the MODIS 0.650 μm channel and the Angstrom exponent for mineral dust aerosol is zero so that the dust AOD is the same for the three channels. In addition, the Deep Blue algorithm also includes the procedure for mixed aerosol (dust/smoke) retrievals. The fundamental physical principles of the Deep Blue algorithm and the technical details for its operational implementation are described in Hsu et al. [2004, 2006].

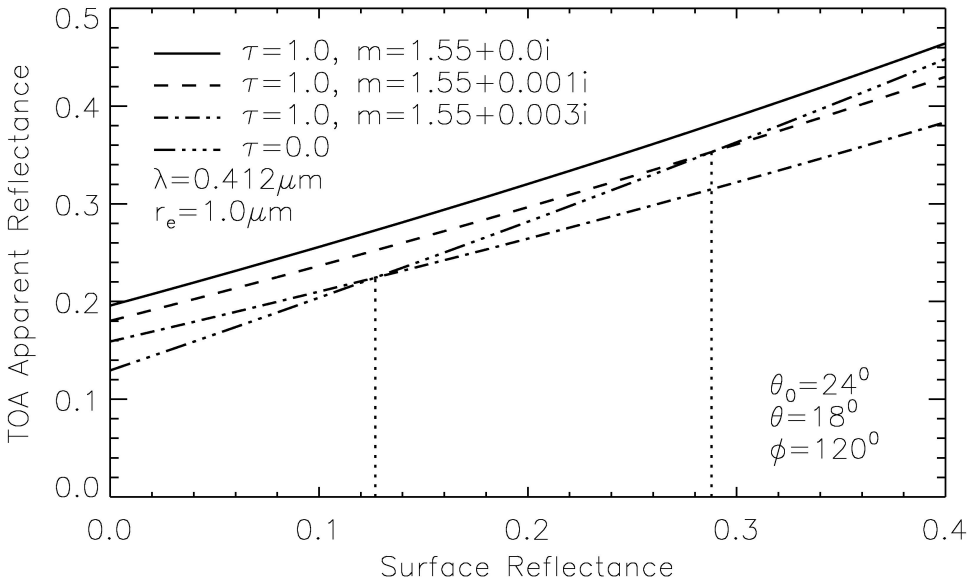

Fig. 5 Relationships between simulated TOA apparent reflectance and Lambertian surface reflectance, for different values of AOD (τ) and refractive index (m). The vertical lines indicate the critical surface reflectance where the presence of aerosol cannot affect the TOA apparent reflectance, depending on the aerosol refractive index (i.e., aerosol absorption).

3. SCATTERING AND RADIATIVE PROPERTIES FOR MINERAL DUST AEROSOLS AND THE EFFECT OF PARTICLE NONSPHERICITY ON RETRIEVING DUST OPTICAL DEPTHS

3.1 Methods

With the assistance of the aforementioned scattering-computational methods, the scattering and radiative properties for nonspherical mineral dust aerosols at the channels used in the Deep Blue algorithm are simulated based on the spheroidal particle shape assumption. For comparison, the corresponding results related to the spherical particle shape assumption are also presented. Moreover, the applicability of a hybrid approach based on the spheroidal particle shape assumption for the phase function and the spherical particle shape assumption for the other phase matrix elements is also demonstrated. Based on the Deep Blue aerosol retrieval algorithm, the commonly used LUT technique is employed for the retrieval based on the best match between the simulated reflectance and the measured counterparts at the MODIS 0.412, 0.470 and 0.650 μm channels. To quantify the effect of particle nonsphericity on retrieved dust AOD, two different LUTs based on the polarized radiative transfer model are developed. One is derived from the assumption of a spheroidal particle shape, and the other from the assumption of a spherical shape.

3.2 Bulk scattering properties of mineral dust aerosols

For remote sensing applications, the bulk scattering properties of mineral dust aerosols are required and can be derived by integrating the single-scattering properties of

individual particles over size (specified in terms of the radius of a volume-equivalent sphere) and shape (specified in terms of particle aspect ratio) distributions [Mishchenko et al., 1997; Nousiainen and Vermeulen, 2003; Dubovik et al., 2002a, 2006]. To obtain the bulk scattering properties of mineral dust aerosols, the single-scattering properties of individual dust particles need to be averaged over particle size and shape distributions. In this study, we use the lognormal function for particle size distribution [Kokhanovsky et al., 2006; Dubovik et al., 2006] given by

$$\frac{dn(r)}{d\ln r} = \frac{N_0}{\sqrt{2\pi}\ln\sigma_g}\exp\left[-\frac{(\ln r - \ln r_g)^2}{2(\ln\sigma_g)^2}\right], \tag{22}$$

where r is the radius of the volume-equivalent sphere, N_0 is number concentration, r_g is the median radius, and σ_g is the standard deviation. The size distribution parameters (i.e., r_g and σ_g) for mineral dust aerosols are uncertain and vary from region to region, depending critically on their geographic sources [Dubovik et al., 2002b; Reid et al., 2003a]. The typical values of the effective radius for mineral dust range from 0.5 to 1.2 μm, and reach up to 3.0 μm during the initial stage of dust storms. The variation in particle size distribution leads to uncertainties in the simulation of the scattering properties of mineral dust aerosols.

Mishchenko et al. [1997] showed that a mixture of randomly oriented spheroids with a broad aspect ratio distribution for all sizes can smooth out the features in the phase functions in side-scattering directions to resemble the overall scattering pattern observed for natural dust particles. Following Dubovik et al. [2006] who used 20 aspect ratios and a sophisticated method to derive dust particle shape distribution from the laboratory measurements of the feldspar phase matrix at 0.441 and 0.633 μm, in this study, we

consider an ensemble of spheroids with 20 aspect ratios distributed logarithmically equidistant between 0.3 and 3.3. Without imposing a constraint of an equal probability for prolate and oblate spheroidal particles, we employ the Monte Carlo method to derive the weights for different aspect ratios based on the best fit of the theoretically simulated phase matrix to the measured results for feldspar dust samples at a wavelength of 0.441 μm. The measured phase matrix of feldspar, as a function of the scattering angle in the range 5°-173°, is chosen as a reference for fitting the theoretical results to the measurements, because feldspar samples account for the majority of desert dust aerosol from Africa [Reid et al., 2003b]. Moreover, the measured results for feldspar samples at 0.441 and 0.633 μm do not show much difference. Thus, we only use the phase matrix of feldspar at 0.441 μm, although the data for the 0.633 μm wavelength is also available. Here, we assume that the effective radius r_e and effective variance v_e for mineral dust aerosols are 1.0 μm and 1.0, respectively. These values are consistent with the laboratory measurements of feldspar dust samples [Volten et al., 2001]. Note that the present fitting procedure follows that reported by Dubovik et al. [2006]. Fig. 6 shows the weights for the aspect ratios derived in this study, which have a broad distribution. Evidently, particles with aspect ratios that deviate considerably from unity have larger weights than quasi-spherical particles whose aspect ratios are close to unity, particularly, in the case of prolate spheroids. Furthermore, in an ensemble of the particles, prolate (i.e., the aspect ratio larger than unity) shapes dominate.

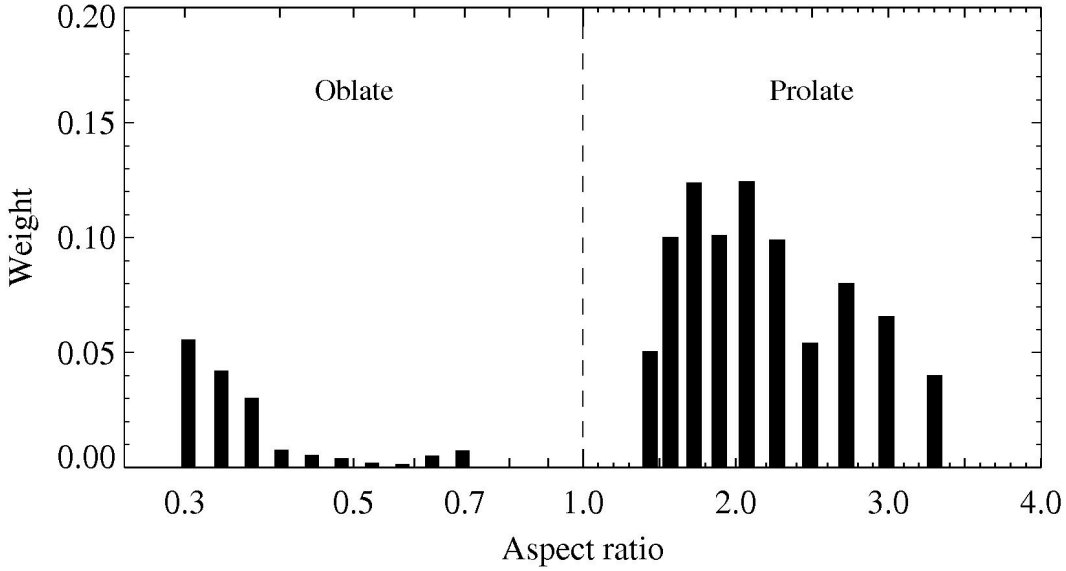

Fig. 6 Weights for various aspect ratios derived from the best fit of the theoretically simulated phase matrix to the measured counterparts.

To consider the effect of the spectral response function for a given MODIS channel, the bulk phase matrix can be calculated as follows [Baum et al., 2005]:

$$P_{ave} = \frac{\int_{\lambda_1}^{\lambda_2} \sum_{k=1}^{20} W_k \int_r P(\varepsilon_k, r, \lambda) Q_s(\varepsilon_k, r, \lambda) A(\varepsilon_k, r) \frac{dn(r)}{d \ln r} d \ln r F(\lambda) S(\lambda) d\lambda}{\int_{\lambda_1}^{\lambda_2} \sum_{k=1}^{20} W_k \int_r Q_s(\varepsilon_k, r, \lambda) A(\varepsilon_k, r, \lambda) \frac{dn(r)}{d \ln r} d \ln r F(\lambda) S(\lambda) d\lambda} \tag{23}$$

where P_{ave} is the bulk phase matrix, $A(\varepsilon,r)$ is the projected area of an individual dust particle, r is the radius of a sphere of equivalent volume, ε is the aspect ratio, $P(\varepsilon_k,r,\lambda)$ is the phase matrix for a given aspect ratio, particle size and wavelength, $Q_s(\varepsilon_k,r,\lambda)$ is the scattering efficiency, W_k is the weight for each aspect ratio, $F(\lambda)$the spectral response function, and $S(\lambda)$ is the solar spectrum. Note that Eq. (23) can also be applied to the monochromatic case if the response function is replaced by the Dirac-delta function, i.e., $F(\lambda) = \delta(\lambda - \lambda_0)$ where λ_0 is a monochromatic wavelength of interest.

Fig. 7 is a comparison of the phase matrices from the present model simulations and from the measurements for feldspar particles [Volten et al. 2001]. The complex refractive index of dust particles used in the model simulation is 1.55+0.001i. Evidently, the simulated phase matrix based on a spheroid model agrees quite well with the experimental results, particularly, in the case of the phase function. On the contrary, the spherical counterpart substantially deviates from the experimental results in side-scattering (100º-130º) and backscattering (150º-180º) directions. The ratios P_{34}/P_{11} and P_{44}/P_{11} for spherical particle shape assumption are quite different from measurements at the scattering angles (120°-180°). The ratio P_{22}/P_{11} can be used to test nonsphericity [Bohren et al., 1983], and is known as a “nonsphericity indicator” because it is quite sensitive to the degree of particle nonsphericity, as demonstrated by Mishchenko et al.

[2002]. The experimental data of P_{22}/P_{11} shown in Fig. 7, indicates that realistic dust particles are nonspherical. In terms of the agreement between the theoretical and measured results for P_{22}/P_{11}, $-P_{12}/P_{11}$ and P_{33}/P_{11}, a substantial improvement is observed in the case for the spheroid model in comparison with the case for the sphere model.

Fig. 8 shows the simulated phase functions with different effective radius for spheroidal dust particles at the wavelength of 0.650 μm. The solid and dot line show the phase function for dust particles with an effective radius of 1.0 μm and 0.5 μm respectively. The effective variance is 1.0 for both cases. Obviously, the forward peak for the phase function decreases as the dust particle size becomes smaller. The differences of the phase functions between these two different particle sizes are not quite significant at side-scattering and backscattering angles. The corresponding empirical phase function used in the Deep Blue algorithm is also shown in this figure for comparison. This empirical phase function was derived based on the best fit between the satellite retrieved AOD and the measured results by the ground-based Aerosol Robotic Network (AERONET) at Cape Verde [Hsu et al., 2006]. By comparing the forward peak between the empirical phase function and the phase functions with different particle sizes, we can conclude that the empirical phase function corresponds to dust particles with smaller particle size.

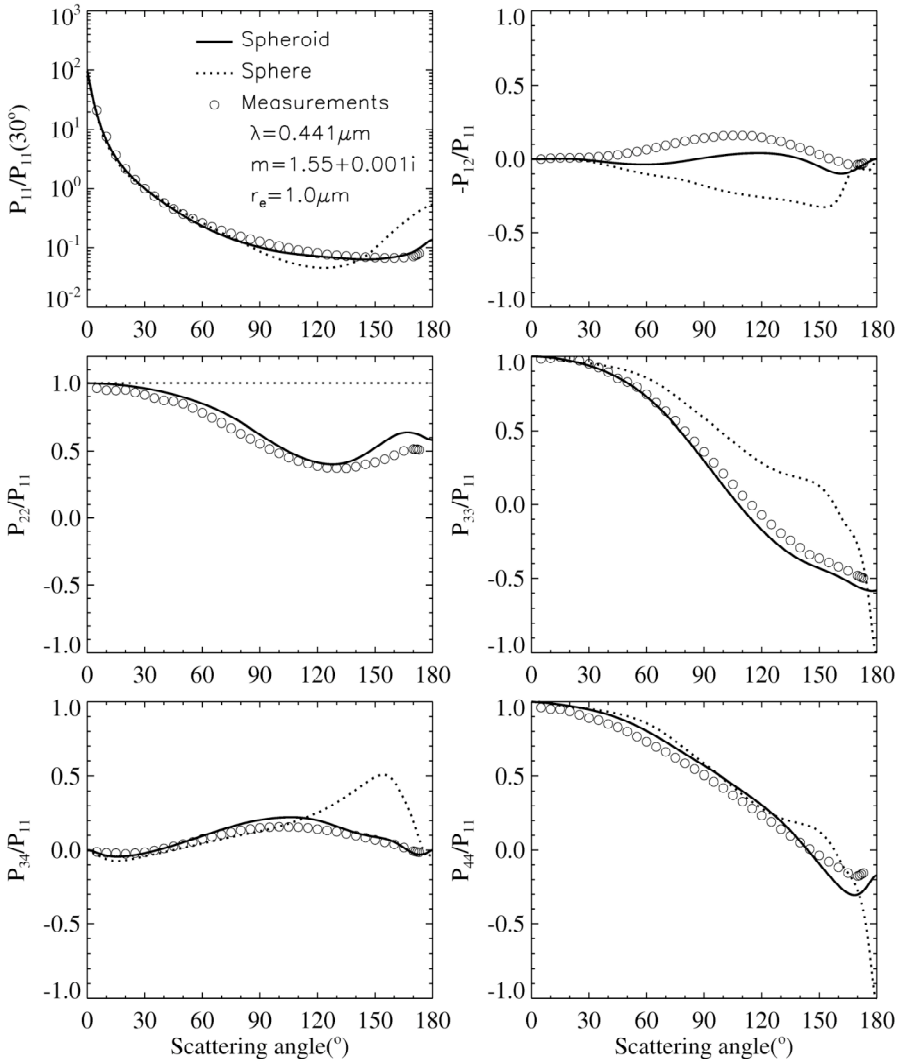

Fig. 7 Comparison between the theoretical simulation results and their counterparts based on laboratory measurements for the scattering phase matrices of feldspar samples. The solid lines indicate the simulated phase matrix based on a spheroid model. The dotted lines indicate the simulated result based on the Mie theory.

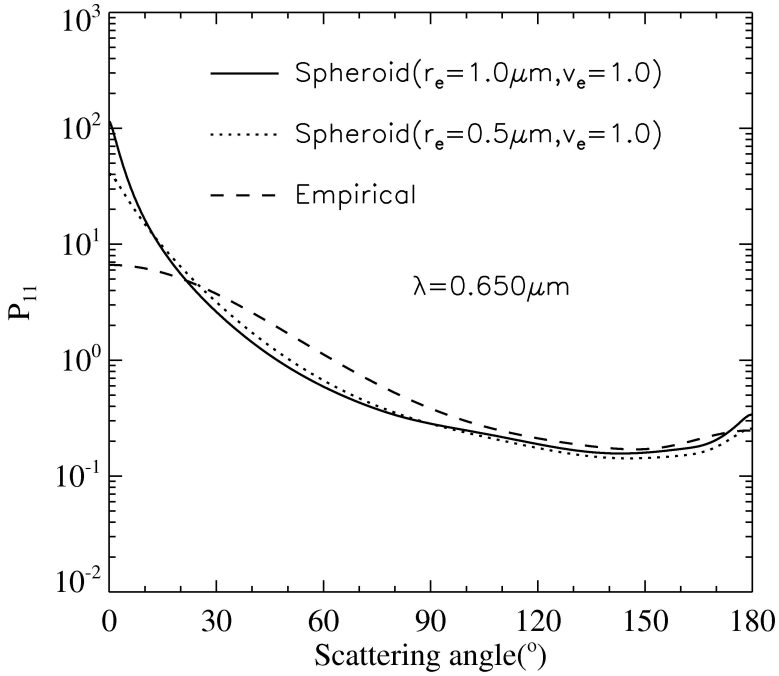

Fig. 8 Simulated phase functions with different effective radius for spheroidal dust particles at the wavelength of 0.650 μm. For comparison, the corresponding empirical phase function used in the Deep Blue algorithm is also shown in this figure.

3.3 Radiative properties of mineral dust aerosols

For simplicity in the present radiative transfer simulation, gaseous absorption is not considered. To account for the vertical distribution of aerosol loading, in this study, the entire atmosphere is divided into 7 layers from the surface to the top of the atmosphere, and the vertical distribution of aerosol loading in the atmosphere is specified in terms of a Gaussian function peaked at 3 km above the surface. The atmospheric Rayleigh optical depth $\tau_{R,\lambda}$ (at sea level) is calculated approximately in the visible spectral region via the following formula [Dutton et al., 1994]:

$$\tau_{R,\lambda} = 0.00877\lambda^{-4.05}, \tag{24}$$

where λ is the spectral wavelength with units in microns.

To include different types of dust aerosols specified by different absorption, we use a number of refractive indices of dust aerosols for the MODIS channels centered at 0.412 and 0.470 μm to get a distribution of the single-scattering albedo values corresponding to various absorption conditions. Table 1 lists the refractive indices and the corresponding single-scattering albedos simulated for three MODIS channels based on the spheroid and sphere models. It should be noted that the differences of the single-scattering albedos computed from these two models are relatively small although the corresponding phase matrices (not shown here) are quite different. Table 2 lists the refractive indices and the corresponding single-scattering albedos simulated for three MODIS channels for different particle sizes. Obviously, the single scattering albedos are sensitive to the particle size and refractive index for mineral dust aerosols. For example, in the case of the refractive index equal to 1.55+0.003i, when r_e decrease from 1.0 to 0.5 μm, the corresponding ω increases from 0.929 to 0.961 for the MODIS channel of 0.412 μm.

Table 1 Comparisons of the single-scattering albedos computed from the spheroid and sphere models at three MODIS channels used in the Deep Blue aerosol retrieval algorithm. The effective radius r_e and effective variance v_e for mineral dust aerosols are 1.0 μm and 1.0, respectively.

Refractive index at 412nm	ω at 0.412 μm for the spheroid model	ω at 0.412 μm for the sphere model
1.55+0.00i	1.0	1.0
1.55+0.001i	0.972	0.972
1.55+0.002i	0.949	0.948
1.55+0.003i	0.929	0.927
Refractive index at 0.470 μm	ω at 0.470 μm for the spheroid model	ω at 0.470 μm for the sphere model
1.55+0.00i	1.0	1.0
1.55+0.001i	0.976	0.975
1.55+0.002i	0.955	0.954
1.55+0.003i	0.936	0.934
Refractive index at 0.650 μm	ω at 0.650 μm for the spheroid model	ω at 0.650 μm for the sphere model
1.55+0.00i	1.0	1.0

Table 2 Comparisons of the single-scattering albedos computed from different particle sizes for spheroidal particle shape assumption at three MODIS channels used in the Deep Blue aerosol retrieval algorithm.

Refractive index at 412nm	ω at 0.412 μm (r_e =1.0 μm; v_e =1.0)	ω at 0.412 μm (r_e =0.5 μm; v_e =1.0)
1.55+0.00i	1.0	1.0
1.55+0.001i	0.972	0.986
1.55+0.002i	0.949	0.973
1.55+0.003i	0.929	0.961
1.55+0.004i	0.910	0.949
Refractive index at 0.470 μm	ω at 0.470 μm (r_e =1.0 μm; v_e =1.0)	ω at 0.470 μm (r_e =0.5 μm; v_e =1.0)
1.55+0.00i	1.0	1.0
1.55+0.001i	0.976	0.987
1.55+0.002i	0.955	0.975
1.55+0.003i	0.936	0.964
1.55+0.004i	0.919	0.954
Refractive index at 0.650 μm	ω at 0.650 μm (r_e =1.0 μm; v_e =1.0)	ω at 0.650 μm (r_e =0.5 μm; v_e =1.0)
1.55+0.00i	1.0	1.0

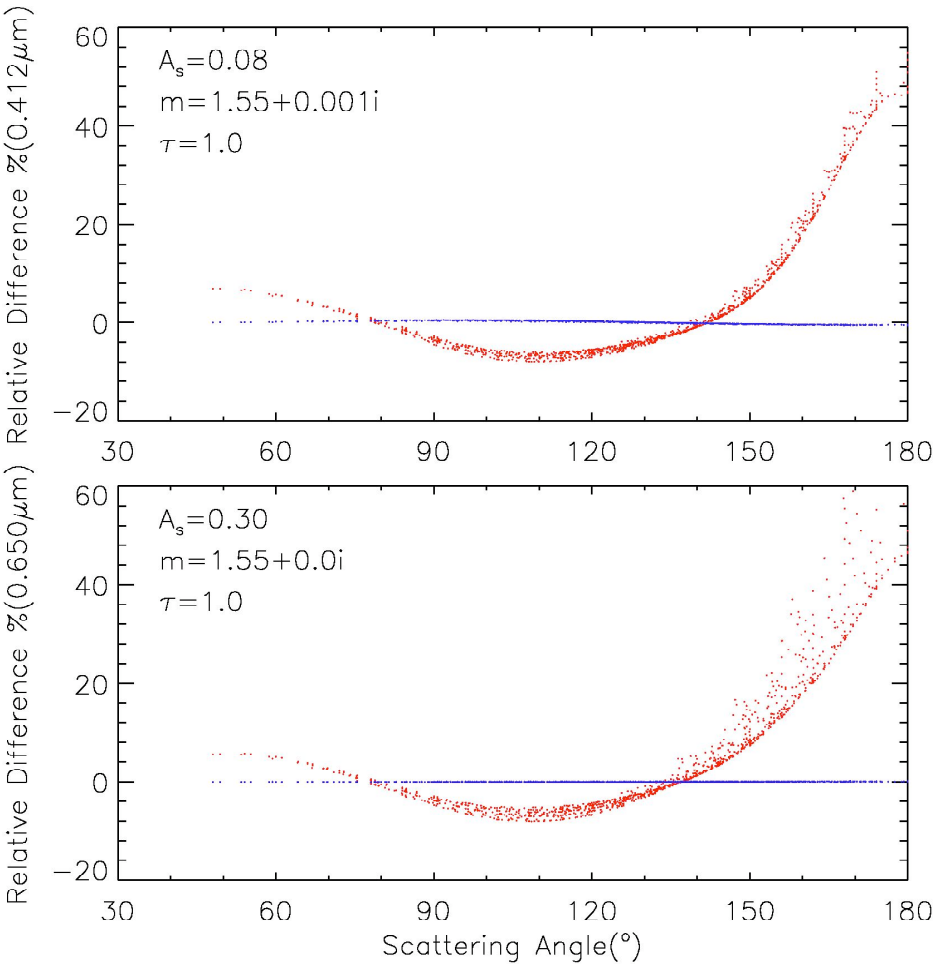

Fig. 9 Relative differences of TOA intensity between the spherical and spheroidal particle shape assumption (red dots) as a function of scattering angle at the MODIS channels of 0.412 and 0.650 μm. The corresponding result between the hybrid and spheroid model is shown in blue dots. The dust AOD is 1.0 for both cases. The surface reflectances are assumed to be 0.08 and 0.30 for the 0.412 and 0.650 μm channels, respectively.

Fig. 9 shows the relative differences of the TOA upward radiances simulated from the sphere and spheroid models, $(I_{sphere} - I_{spheroid})/I_{spheroid} \times 100\%$ (red dots), as a function of scattering angle at two MODIS channels centered at 0.412 and 0.650 μm. In addition to the spheroid and sphere models, we also consider a hybrid model for which the phase function is from the nonspherical spheroid model; whereas, the other nonzero elements of the phase matrix come from the results based on the sphere model. The relative differences between radiances simulated from the hybrid and spheroid models, $(I_{hybrid} - I_{spheroid})/I_{spheroid} \times 100\%$, are also shown as blue dots in Fig. 9. The surface reflectances assumed for the present simulations are 0.08 and 0.30 for the MODIS 0.412 and 0.650 μm channels, respectively, and the dust AOD is assumed to be 1.0. Evidently, the relative differences of the TOA radiances associated with the hybrid and spheroid models are quite small and practically negligible compared to the relative differences of the TOA radiances associated with the sphere and spheroid models.

The results shown in Fig. 9 illustrate that the TOA radiances under dusty conditions are sensitive to the phase function rather than other elements of the phase matrix. It is also evident from Fig. 9 that the relative differences between the TOA radiances computed from the sphere and spheroid models depend strongly on scattering angle and are quite significant in side-scattering (90-130º) and backscattering (150-180º) directions. Furthermore, the relative differences of the TOA radiances between the sphere and spheroid models are consistent with the trend of the corresponding phase function differences (see Fig. 7), since the simulated TOA radiances for a dusty atmosphere are approximately proportional to the phase function used in the radiative transfer simulation. An increase of the surface reflectance leads to a spreading of the data points for the relative differences of TOA radiances between the sphere and spheroid models (black dots) at larger scattering angles (>140º). This is probably due to the increased multiple reflections between the surface with a higher reflectivity and a dust aerosol layer, which enhance the multiple scattering of radiation by dust particles.

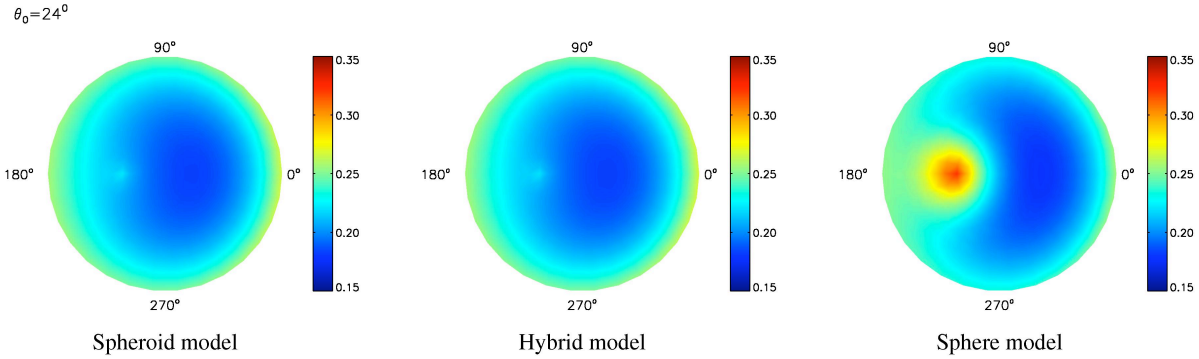

Fig. 10 Polar plot (radius, view zenith angle; angle, relative azimuthal angle) of the TOA upward normalized radiances simulated from the spheroid, hybrid and sphere models at the MODIS 0.412 μm channel with an assumed refractive index of 1.55+0.001i. The solar zenith angle is 24º. The AOD and surface reflectance are assumed to be 1.0 and 0.08, respectively.

Fig. 10 shows the polar plot of the TOA upward normalized radiances simulated from the spheroid, hybrid and sphere models at the MODIS channel of 0.412 μm. Here, the normalized radiance is defined as $\pi I / F_0$, where I is the TOA upward radiance, and F_0 is the solar flux at the top of the atmosphere. The corresponding refractive index of dust aerosol is assumed to be 1.55+0.001i. The solar zenith angle is 24º. The AOD and surface reflectance are 1.0 and 0.08, respectively. Note that the patterns of the TOA upward radiances for the spheroid and hybrid models are similar. However, the pattern for the sphere model is quite different from that of the spheroid model, especially at the backscattering angle (180º).

Fig. 11 shows the contours of the relative differences of the TOA upward radiances simulated from the sphere and spheroid models, $(I_{sphere} - I_{spheroid}) / I_{spheroid} \times 100\%$, versus the solar zenith angle and view zenith angle at the MODIS 0.412 μm channel for four relative azimuthal angles. For the 0.412 μm MODIS channel, the input parameters for the radiative transfer simulations shown in Fig. 11 are the same as those in Fig. 10. It is evident from Fig. 11 that the nonsphericity effect on the TOA radiance is quite sensitive to the relative azimuthal angle. For some incidence-viewing geometries, neglecting the nonsphericity effect can lead to errors up to as much as 50%, i.e., in a large angular regime when $\phi = 180^o$.

Fig. 12 shows the simulated TOA reflectances for a dust atmosphere as a function of scattering angles (125º-150º) for different values of dust particle size and refractive index. The corresponding values of single-scattering albedo, which depend on particle size and refractive index, are also depicted in the figure. The surface albedo and dust optical depth are assumed to be 0.06 and 1.0, respectively. Because of single scattering

approximation, the simulated TOA reflectances are proportional to the phase function and single-scattering albedo of dust aerosols. As shown in Fig. 8, the differences of the phase functions between dust aerosols with effective radius of 1.0 μm and 0.5 μm are not quite significant at side-scattering and backscattering angles. As a result, the simulated TOA reflectances corresponding to these two different particle sizes are very sensitive to the single-scattering albedo of dust aerosols.

3.4 The effect of particle nonsphericity on dust optical depth retrievals

To retrieve dust properties, we develop two LUTs for the TOA bi-directional reflectance based on the spherical and spheroidal shape assumptions respectively, at three MODIS channels centered at 0.412, 0.470 and 0.65 μm. It has been suggested that the parameterization of LUTs can be employed in aerosol remote sensing over reflecting land surfaces [Kokhanovsky et al., 2005]. The format of the present LUTs are quite similar to that used in the Deep Blue algorithm, i.e., the LUTs are developed with respect to the view zenith angle, the solar zenith angle, the relative azimuthal angle, the AOD, the surface reflectance, and the single-scattering albedo. TOA reflectance in the LUTs is calculated for 13 solar zenith angles (θ_0=0.0° to 72.0°, with an increment of 6.0°), 14 view zenith angles (θ=0.0° to 78.0°, with an increment of 6.0°), and 16 relative azimuthal angles (φ=0.0° to 180.0°, with an increment of 12.0°). Here, the effective radius and effective variance for mineral dust aerosols are 1.0 μm and 1.0, respectively.

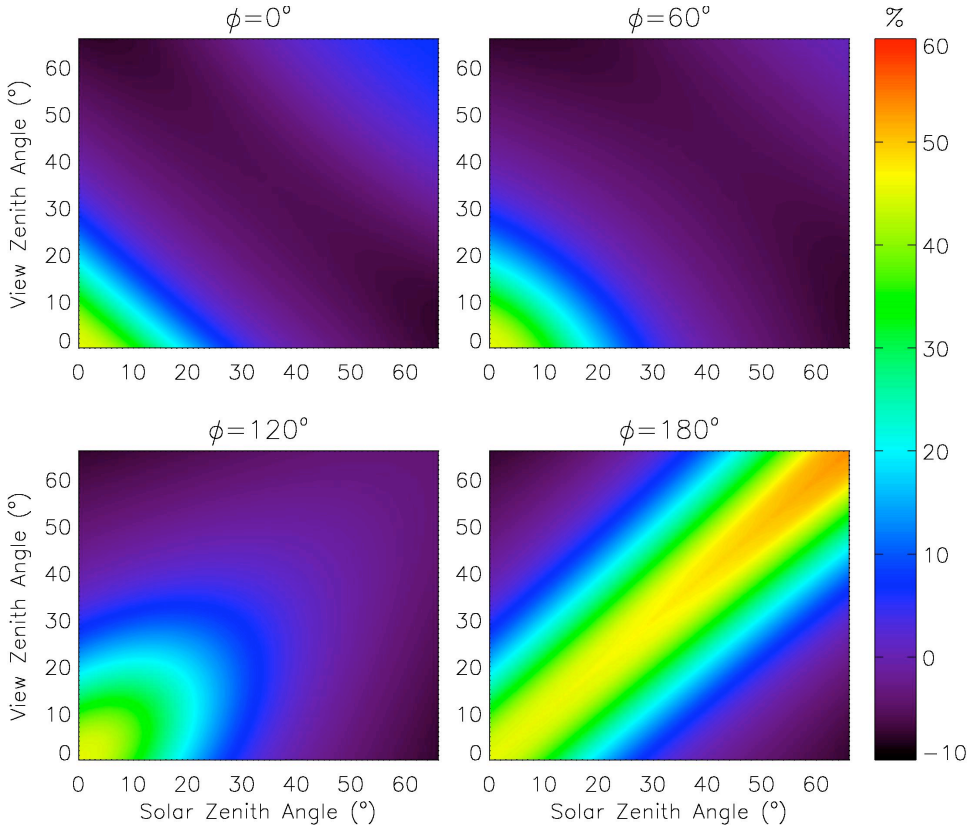

Fig. 11 Contours of the relative differences between the TOA upward radiances simulated from the sphere and spheroid models, $(I_{sphere} - I_{spheroid}) / I_{spheroid} \times 100\%$, versus the solar zenith angle and view zenith angle at the MODIS 0.412 μm channel for four relative azimuthal angles. The optical depth and surface reflectance are assumed to be 1.0 and 0.08, respectively.

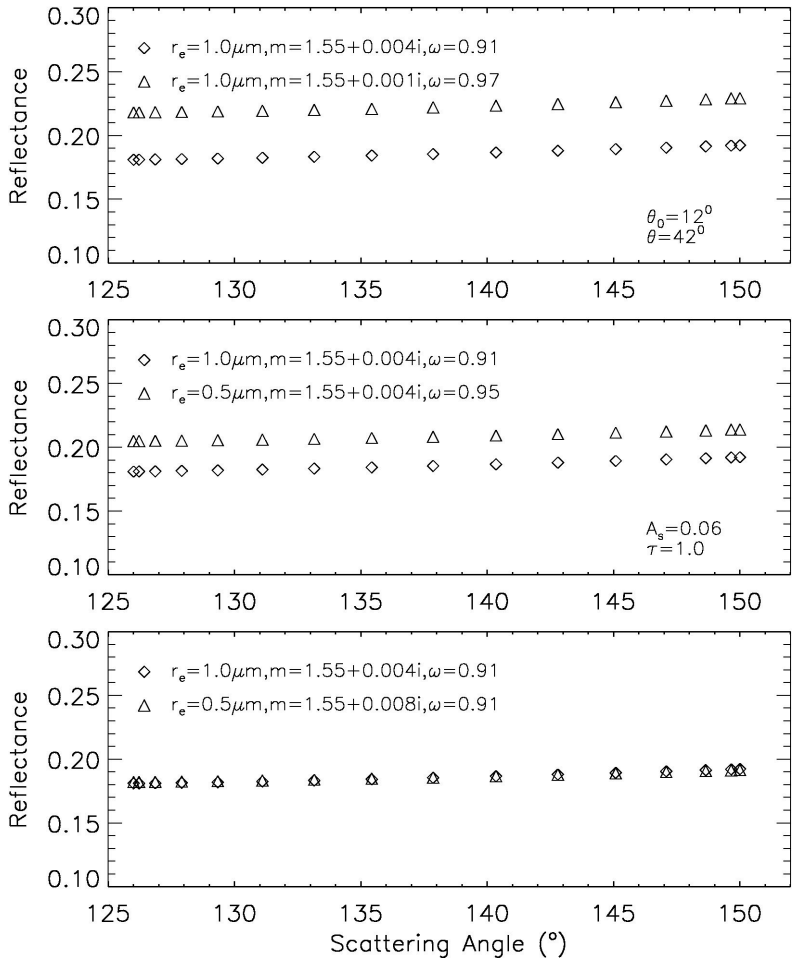

Fig. 12 Simulated TOA reflectances for a dust atmosphere as a function of scattering angles for different values of dust particle size and refractive index.

Fig. 13 shows the LUTs for the two-channel retrieval technique used in the present retrieval algorithm on the basis of the scattering properties computed from the spheroid and sphere models. It shows the relationship between the simulated TOA upward reflectance in the MODIS channels of 0.412 and 0.470 μm as a function of AOD for two kinds of dust aerosols. The term "Dust(1.0,1.0)" indicates non-absorptive dust aerosols. The term "Dust(0.91,0.95)" indicates dust aerosols that are moderately absorptive, whose single-scattering albedos are 0.91 and 0.95 for the MODIS 0.412 and 0.470 μm channels, respectively. In this figure, the sun-satellite geometry in the upper panel corresponds to a scattering angle of 145° and in the lower panel corresponds to a scattering angle of 123°.

Obviously, the LUT for the two-channel retrieval technique based on the sphere model is quite different from that based on the spheroid model. It is expected that the differences in the LUTs for the spheroid and sphere models lead to an inconsistency of the retrieved dust AOD. For example, the AOD inferred from the LUT based on the sphere model is substantially smaller than its counterpart inferred from the LUT based on the spheroid model (as shown in the upper panel), and the opposite is noted in the lower panel.

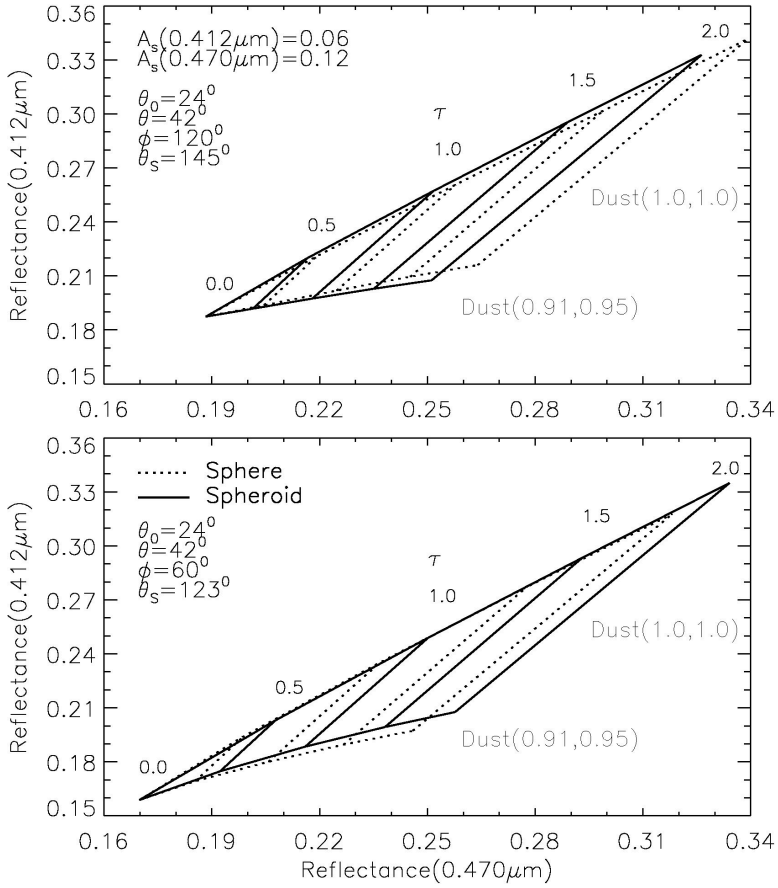

Fig. 13 Correlations between the TOA upward reflectance simulated at the MODIS 0.412 and 0.470 μm channels as a function of AOD for two different kinds of dust aerosols. The term "Dust(1.0,1.0)" indicates non-absorptive dust aerosols, whose single-scattering albedos at the 0.412 and 0.470 μm channels are both 1.0. The term "Dust(0.91,0.95)" indicates that moderately absorptive dust aerosols, whose single-scattering albedos are 0.91 and 0.95 at the 0.412 and 0.470 μm channels, respectively.

Fig. 14 illustrates the correlations between the TOA reflectances at the MODIS 0.412 and 0.650 μm channels (upper panel) and between the reflectances at the MODIS 0.470 and 0.650 μm channels (lower panel) for various AOD and single-scattering albedos. The values of single-scattering albedo shown in this figure are for 0.412 (upper panel) and 0.470 μm (lower panel). These correlations constitute the LUT for a three-channel aerosol retrieval algorithm for simultaneously retrieving dust AOD and single-scattering albedo. Fig. 15 shows similar results as in Fig. 14 but for different sun-satellite geometry. It can be seen from a comparison of Fig. 14 and 15 that the LUTs are sensitive to the sun-satellite geometry configuration. Moreover, the overall features of Fig. 14 and Fig. 15 for the differences between the LUTs based on the sphere and spheroid models are the same as shown in Fig. 13, that is, dust AOD can be overestimated or underestimated if dust particles are assumed to be spheres in the forward radiative transfer simulations involved in aerosol retrievals. The inconsistency of the retrieved dust AOD between the sphere and spheroid models is mainly due to the differences of the phase functions associated with the sphere and spheroid models as a function of scattering angle.

Fig. 16 shows the comparison of LUTs for the two-channel retrieval technique on the basis of the scattering properties computed from different dust particle sizes. One LUT is for dust aerosols with an effective radius of 1.0 μm, and the other with an effective radius of 0.5 μm. However, the corresponding single-scattering albedos associated with no-absorptive and moderately absorptive dust aerosols with an effective radius of 1.0 μm are the same as their counterparts for dust aerosols with an effective radius of 0.5 μm. That is to say, the corresponding refractive indices for non-absorptive and moderately absorptive dust aerosols at the MODIS 0.412 and 0.470 μm channels should be different for these two different particle sizes. Fig. 17 shows the LUTs for the three-channel retrieval technique on the basis of the scattering properties computed from different dust particle sizes. The effective radius corresponding to the solid and dot lines are 0.5 μm and 1.0 μm, respectively. The overall feature of Fig. 16 and Fig. 17 is that the LUTs corresponding to different particle sizes are almost the same. That is, the LUTs for dust aerosol retrievals used in the present study are not very sensitive to the particle sizes. For simplicity, we will use the LUTs corresponding to dust aerosols with an effective radius of 1.0 for the aerosol retrievals.

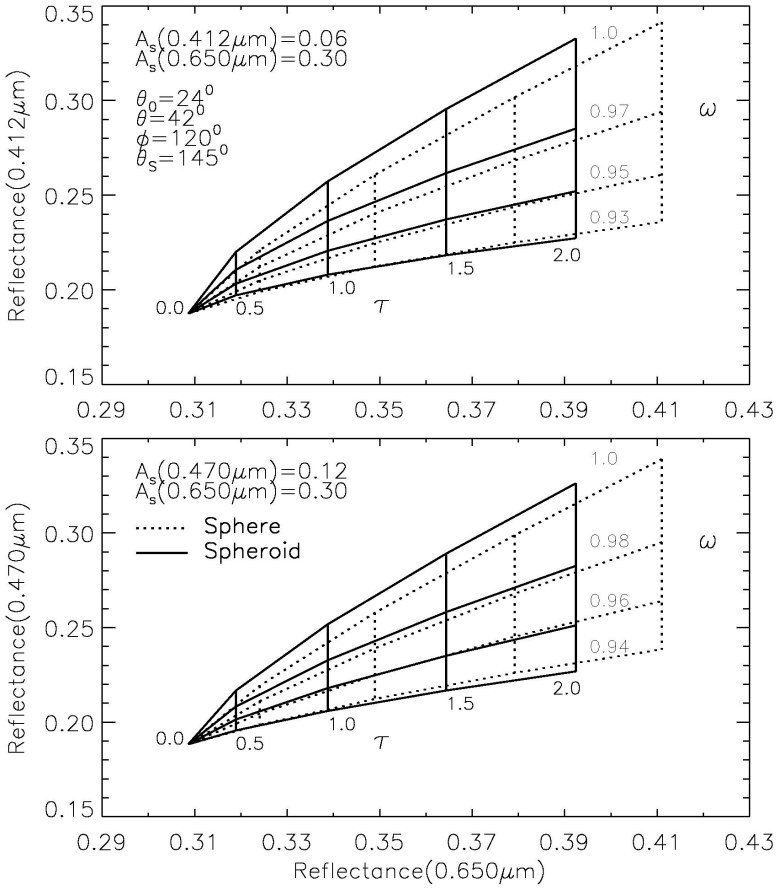

Fig. 14 Correlations between the TOA upward reflectance simulated at the MODIS 0.412 and 0.650 μm channels (upper panel), and the TOA upward reflectance simulated at the MODIS 0.470 and 0.650 μm channels (lower panel) as functions of AOD and single-scattering albedo. The dotted and solid lines indicate the results based on the sphere and spheroid models, respectively. Different single-scattering albedo values shown in the figure are for 0.412 μm (upper panel) and 0.470 μm (lower panel).

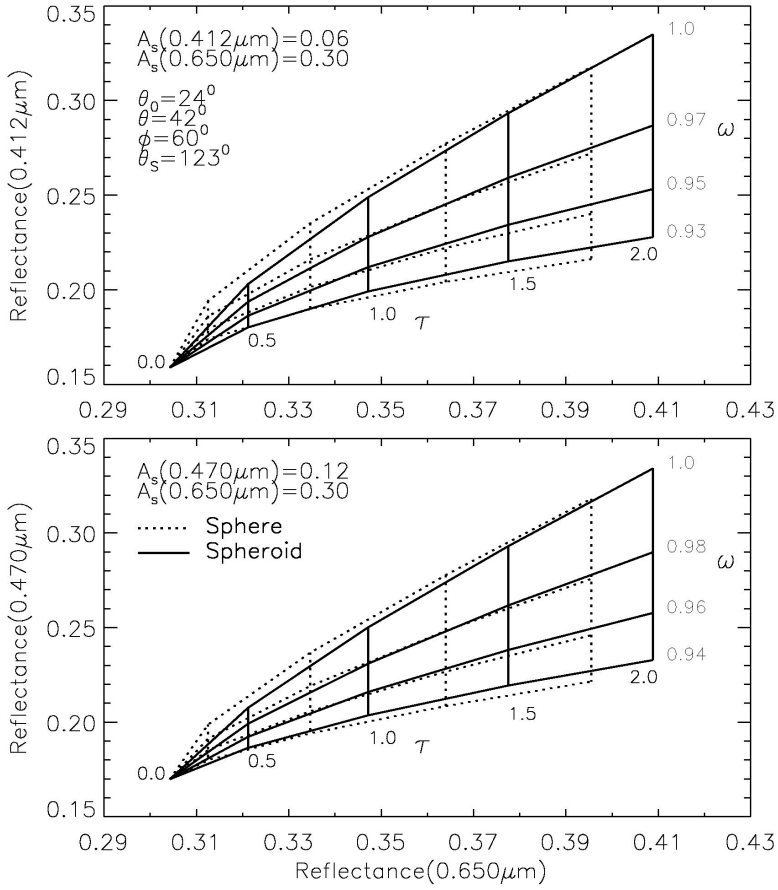

Fig. 15 Same plots as in Fig. 14 but for different sun-satellite geometry.

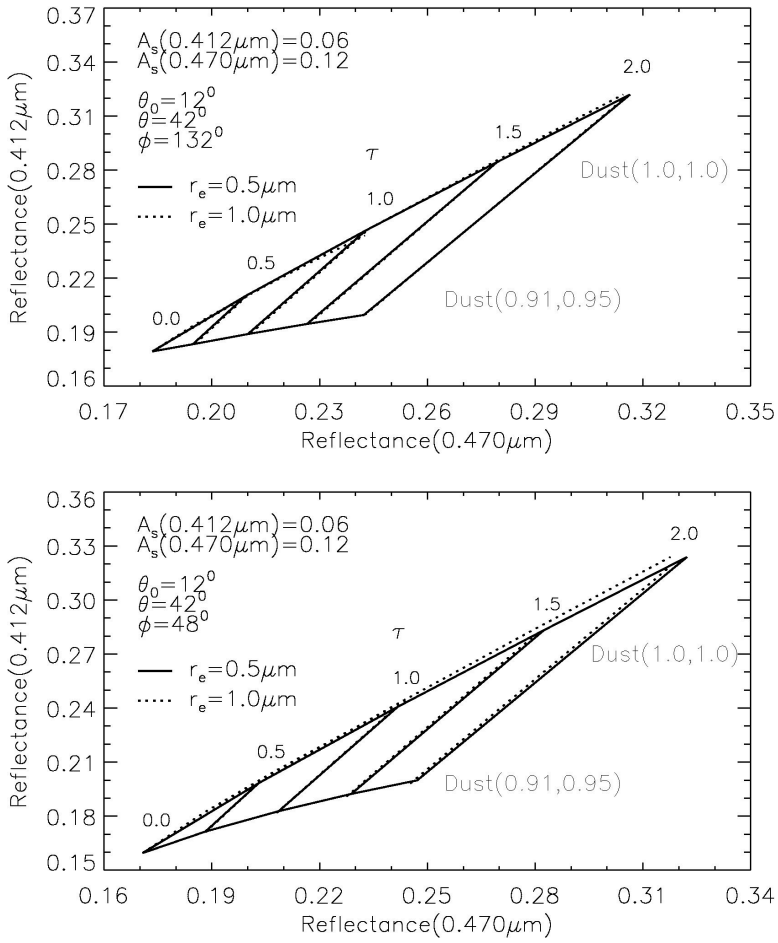

Fig. 16 Comparison of LUTs for the two-channel retrieval technique on the basis of the scattering properties computed from different dust particle sizes.

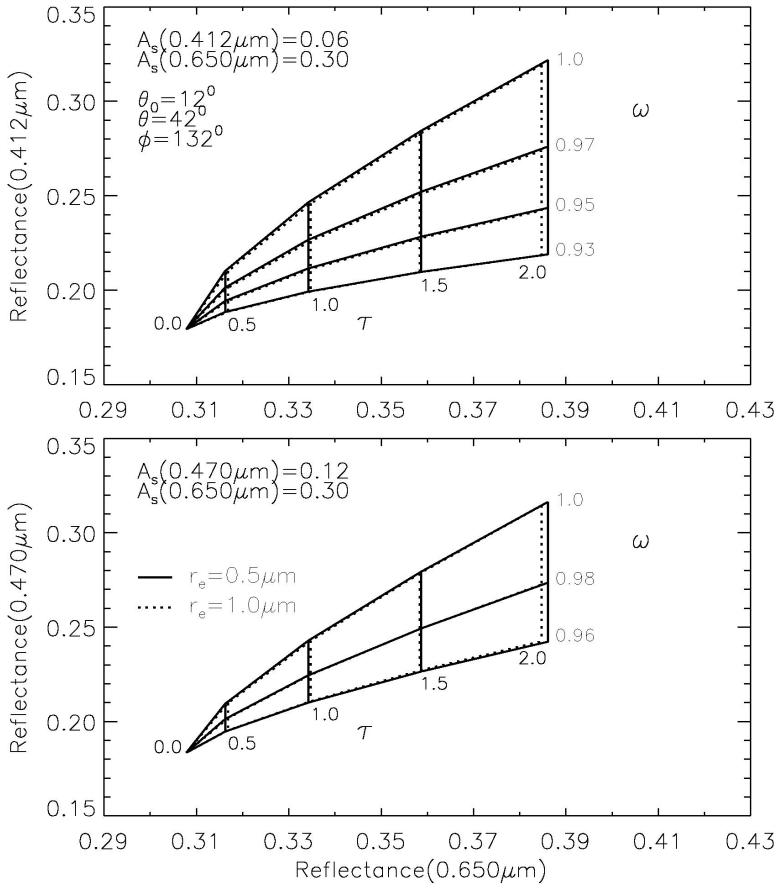

Fig. 17 The comparison of LUTs for the three-channel retrieval technique on the basis of the scattering properties computed from different dust particle sizes.

A prior knowledge of the surface reflectance is needed for implementing an aerosol retrieval algorithm. In this study, the surface reflectance is estimated approximately on the basis of the minimum reflectivity technique (MRT) [Herman and Celarier, 1997; Hsu et al., 2004; Koelemeijer et al., 2003]. Specifically, we use a polarized radiative transfer model [De Haan et al., 1987] to develop a LUT for the TOA upward reflectance with respect to the view zenith angle, the solar zenith angle, the relative azimuthal angle between the sun and satellite, and the surface reflectance for a Rayleigh-scattering atmosphere (without aerosol and cloud contribution). The surface reflection is assumed to be Lambertian. The Lambert-equivalent reflectivity (LER) for each channel is obtained for each cloud-free MODIS pixel based on the best match between the measured TOA reflectance and the corresponding value from LUT. All LER values are sorted with a 0.1° $\times$0.1° longitude-latitude grid resolution, and the minimum value of LER at 0.650 μm and the corresponding values for the other two wavelengths are found as the resultant surface reflectance.

Fig. 18 shows the derived land surface reflectance (with a resolution of 0.1° latitude $\times$ 0.1° longitude) over the Sahara desert at the MODIS 0.412, 0.470 and 0.650 μm channels by using two months (Mar. and Apr., 2003) of the MODIS L1 radiance and L2 cloud product data. Obviously, the surface reflectance over the Sahara desert at 0.412 μm is much smaller than that at 0.650 μm. With the information of the surface reflectance and the LUTs, dust AOD can be retrieved based on the comparison between the theoretical simulated TOA reflectance and their measured counterparts.

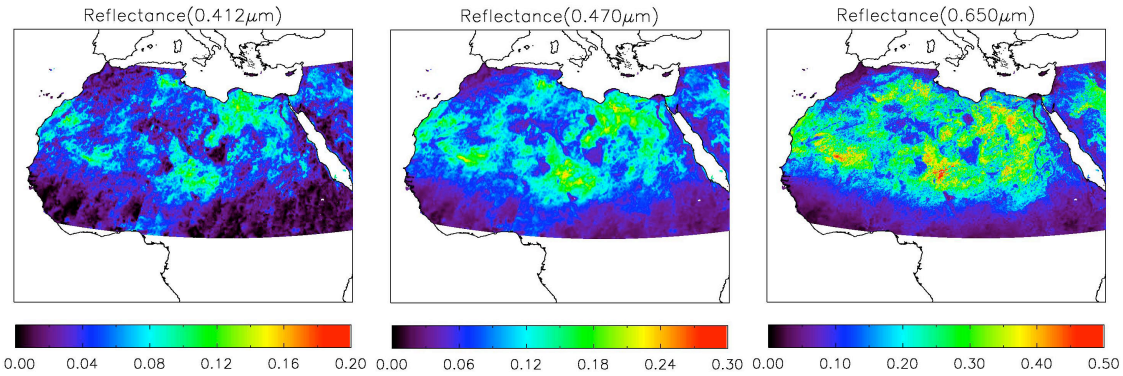

Fig. 18 Calculated land surface reflectance over the Sahara desert at 0.412, 0.470 and 0.650 μm channels by using MODIS L1 radiance and L2 cloud products.

For the present sensitivity study, we select the MODIS observations made over West Africa on 2 March, 2003, which are shown by a RGB (R: band 1, G: band 4, B: band 3) true-color image in Fig. 19. The transport of dust from land to the ocean is evident in this figure. For simplicity, we retrieve AOD in a small area indicated by the red box in Fig. 19, which was cloud-free according to the MODIS cloud mask product. We also assume that the aerosol type for this small area is mineral dust.

Fig. 20 shows the retrieved dust AOD values based on the spheroid and sphere models in the upper left and right panels, respectively. Although the overall patterns in the two panels are similar, there are some pixels for which the retrieval values based on the spheroid model are substantially larger than their counterparts based on the sphere model. The patterns are clearly illustrated in the middle left panel in Fig. 20, which shows the variation of the retrieval based on the sphere model versus the retrieval based on the spheroid model. Evidently, the retrieved dust AOD based on the spheroid model can be either larger or smaller than that retrieved based on the sphere model. The middle right panel shows the histogram distribution of pixel number versus the retrieved dust AOD. There are a number of pixels with dust AOD larger than 1. The lower left panel in Fig. 20 shows the relative difference of the phase functions computed from the sphere and spheroid models as a function of scattering angle, which is defined as

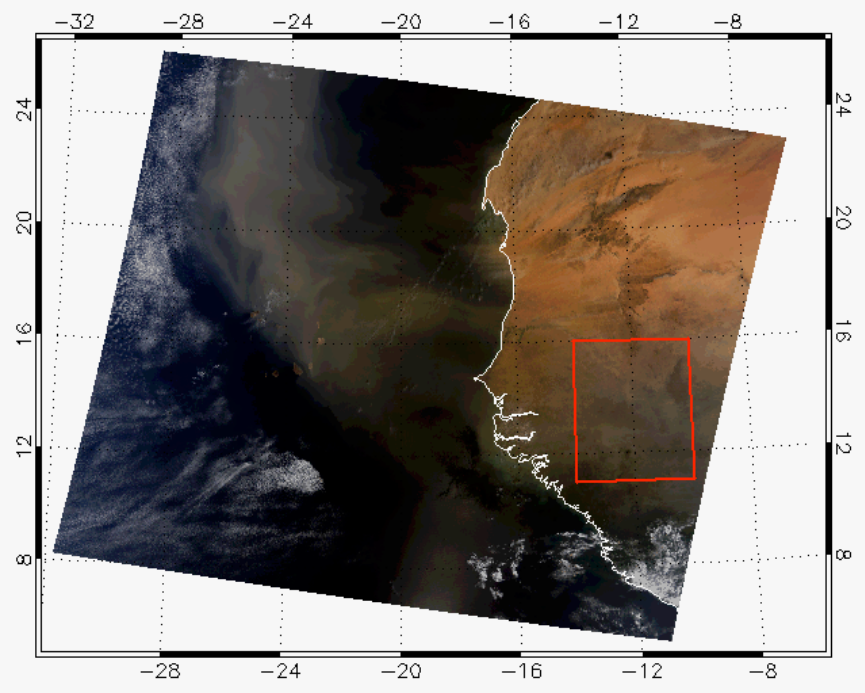

Fig. 19 MODIS RGB image over West Africa on March 2, 2003. The area indicated by the small red box is used to retrieve dust AOD in the present sensitivity study.

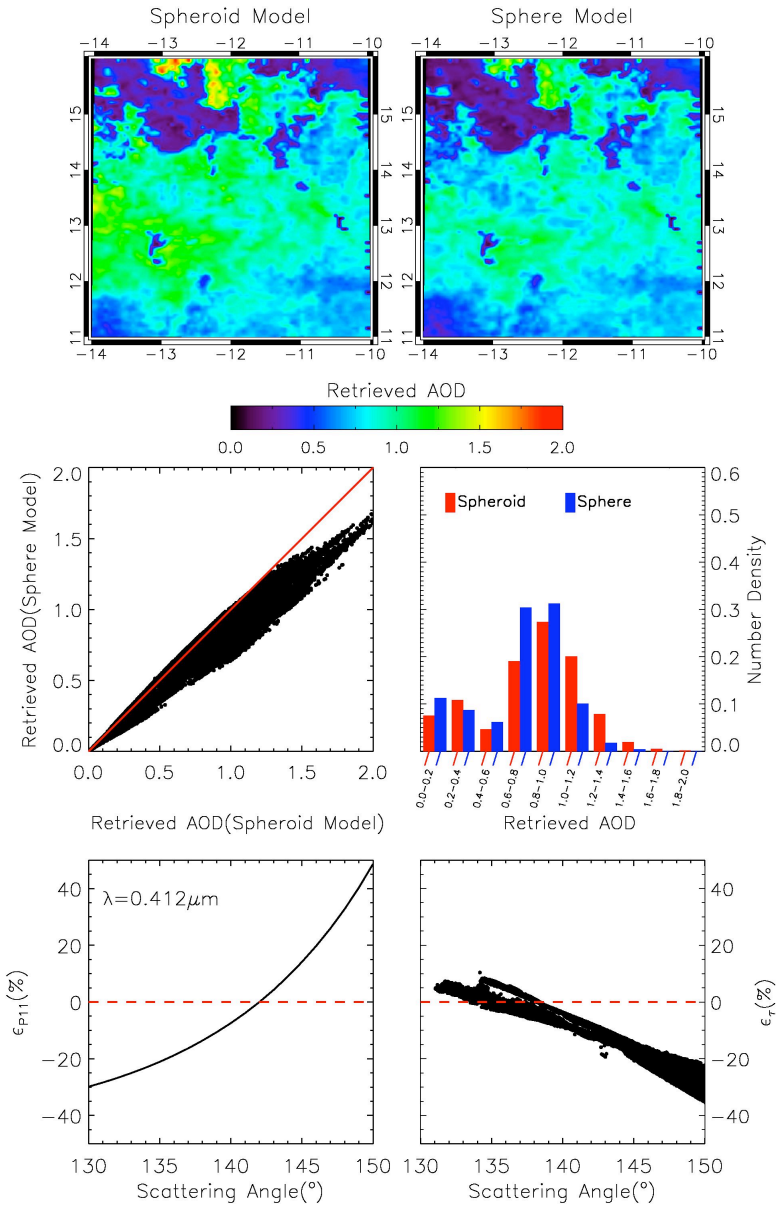

Fig. 20 Upper panels: the retrieved dust AOD based on the spheroid and sphere models. Middle left panel: retrieved dust AOD based on the sphere model versus those based on the spheroid model. Middle right panel: the histogram of retrieved dust AOD based on spheroid and sphere models. Lower left panel: the relative differences of the phase functions. Lower right panel: the relative differences of the retrieved AOD.

$$\varepsilon_{P_{11}} = \frac{P_{11,\text{sphere}} - P_{11,\text{spheroid}}}{P_{11,\text{spheroid}}} \times 100\%. \quad (25)$$

It can be seen the phase function from the sphere model is smaller than its spheroid counterpart for scattering angles between 130º and 142º. For scattering angles larger than 142º, the opposite is observed. This feature noted in the phase function comparison is consistent with that shown in Fig. 7. The lower right panel in Fig. 20 shows the relative difference of the AOD retrieved on the basis of the two models, which is defined as

$$\varepsilon_{\tau} = \frac{\tau_{\text{sphere}} - \tau_{\text{spheroid}}}{\tau_{\text{spheroid}}} \times 100\%. \quad (26)$$

If the coupling of the surface reflection and the multiple scattering of the aerosol layer are not considered, the AOD, under the assumption that the first order scattering dominates the scattered radiation field, can be approximated as

$$\tau \propto R / P_{11}, \quad (27)$$

where R is the bi-directional reflectance. In Eq. (27), the dependence on the incident and viewing geometries is omitted. From the lower two panels in Fig. 20, the variations of ε_{τ} in a scattering region of <134º or >142º can be explained by the relation in Eq. (27). However, the AOD retrieved from the sphere model can be either larger or smaller than its spheroid counterpart in the scattering angle region of 134-140º because of the complicated multiple reflections between the surface and the aerosol layer. It is evident from the lower right panel in Fig. 20, that the assumption of a spherical shape for dust particles can lead to a significant underestimation (~20%) of AOD, especially for large AOD (>1, see the middle left panel in Fig. 20). The results shown in Fig. 20 well demonstrate that the nonsphericity of mineral dust aerosols cannot be neglected for the retrieval of dust AOD.

Fig. 21 shows another example of dust storm across Gobi desert by using a MODIS RGB image over Northern Asia On May 27, 2008. The area indicated by the red box is used to retrieve dust AOD based on the spheroidal and spherical particle shape assumptions, respectively. The aerosol type for this area is also assumed to be mineral dust aerosol, the method for the cloud screening is described in the next section. Fig. 22 shows the comparison of retrieved dust AOD based on the spheroidal and spherical particle shape assumptions. The scattering angles corresponding to the retrieved dust AOD are also shown in this figure. The overall patterns of these two retrieved results are similar, however, there are some pixels for which the retrieved values based on the spheroidal particle shape assumption is different from their counterparts based on the spherical particle shape assumption. The comparisons between these two retrieval datasets are clearly illustrated by Fig. 23, which shows the scatter plots of the retrievals based on the spherical particle shape assumption versus the retrievals based on the spheroidal particle shape assumption for different scattering angles. For scattering angles ranging from 125^{o} to 129^{o}, the dust AOD retrieved from the spherical particle shape assumption is larger than its spheroidal counterparts. For scattering angles larger than 143^{o}, the opposite is observed, and the differences between retrieved dust AOD based on the spheroidal and spherical particle shape assumptions are becoming larger and larger as the scattering angle increase.

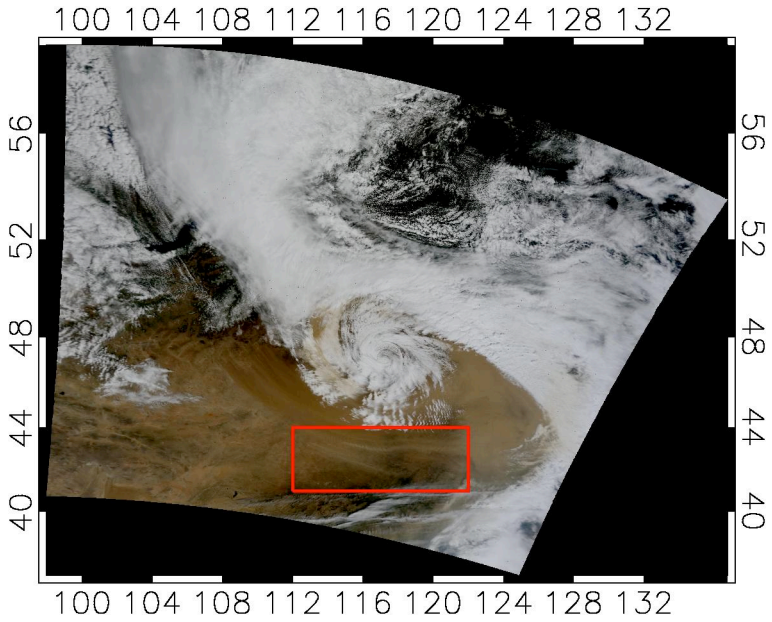

Fig. 21 MODIS RGB image on May 27, 2008, showing a dust plume over North Asia. The area indicated by the small red box is used to retrieve dust AOD in the present sensitive study.

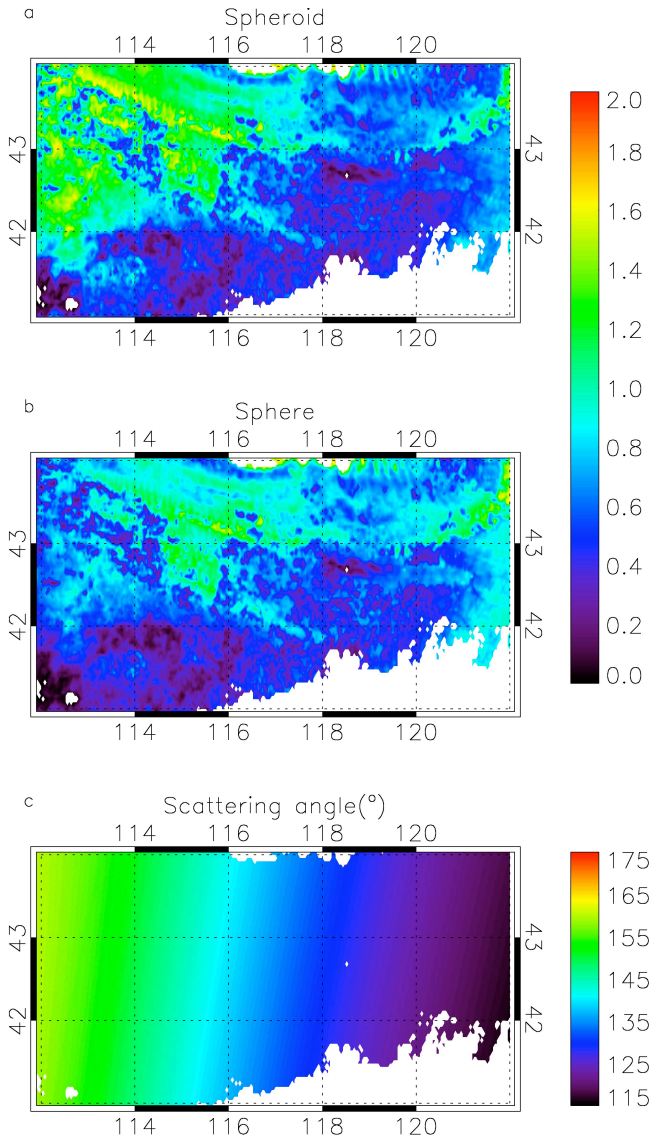

Fig. 22 Comparisons of retrieved dust AOD between the spheroidal and spherical particle shape assumptions. The upper panel shows results for the spheroidal particle shape assumption, the middle panel shows results for the spherical particle shape assumption, and the lower panel shows the corresponding scattering angles.

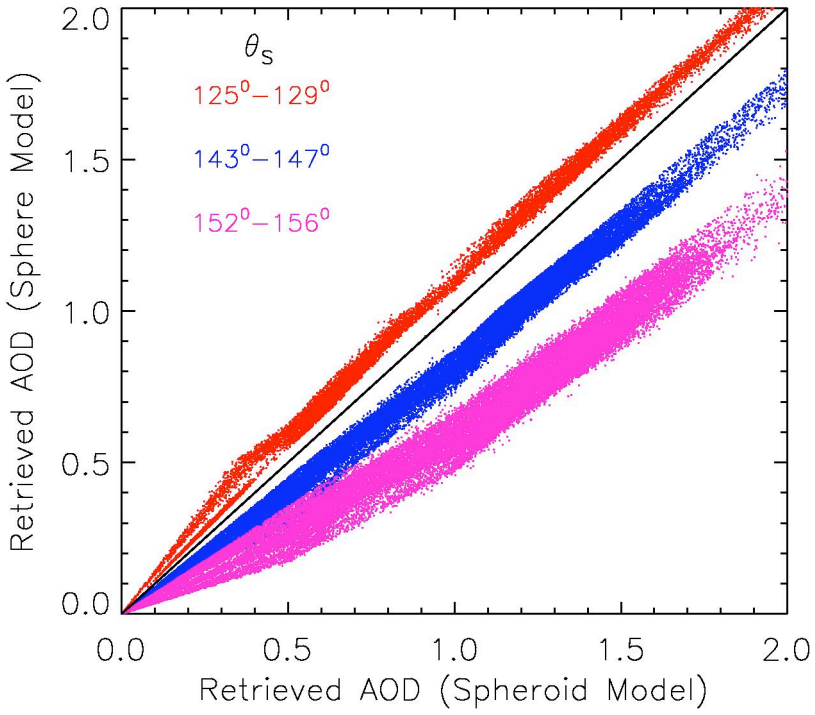

Fig. 23 The scatter plots of retrieved dust AOD based on the spherical particle shape assumption versus the corresponding results based on the spheroidal particle shape assumption, for different scattering angles.

3.5 Summary

To understand the effect of particle nonsphericity on the scattering and radiative properties of mineral dust aerosols, these particles are assumed to be spheroids and spheres in the forward scattering and radiative transfer simulations involved in aerosol property retrieval. The single-scattering properties of mineral dust aerosols are calculated at three MODIS channels based on a combination of the T-matrix method and an improved geometric optics method for spheroidal particles, whereas the Mie theory is used for spherical particles. Differences in the phase functions of mineral dust aerosols between the spheroid and sphere models lead to a significant inconsistency in the calculation of the radiative properties of mineral dust aerosols, particularly, in side-scattering and backscattering directions. Moreover, a sensitivity study was carried out to quantify the nonsphericity effect on the retrieved AOD by using a simple retrieval algorithm that was developed on the basis of the fundamental principles of the Deep Blue aerosol retrieval method. The results indicate that the nonspherical effect of mineral dust aerosols cannot be neglected for the retrieval of dust AOD. In the case of large AOD (>1), neglecting particle nonsphericity may underestimate AOD by as much as 20%, and the differences of the retrieved dust AOD between the spherical and spheroidal particle shape assumptions depend on the scattering angle. Furthermore, it is shown that a hybrid method that uses the phase function associated with nonspherical particles and the other phase matrix elements associated with spherical particles is accurate. Note that this type of hybrid method is implemented in the operational Deep Blue algorithm that uses empirical phase functions to account for the nonsphericity effect of dust particles on their single-scattering properties.

4. THE EFFECT OF THIN CIRRUS CLOUDS ON DUST OPTICAL DEPTH RETRIEVALS

4.1 Methods

To study the effect of undetected thin cirrus clouds on the dust optical depth retrievals, two different kinds of LUTs, each similar to the aforementioned in section 3 for the Deep Blue algorithm, are constructed based on the polarized radiative transfer model. One is for the atmosphere with dust aerosols only (hereafter referred to as dust only atmosphere), and the other is for the atmosphere with overlapping mineral dust layers and thin cirrus clouds (hereafter referred to as dust plus thin cirrus atmosphere). Since it is very difficult to simultaneously retrieve the optical depths for mineral dust and thin cirrus clouds when they coexist, the information related to thin cirrus clouds such as the optical depth and scattering properties is simplified and prescribed a priori for the dust plus thin cirrus atmosphere. For example, it is assumed that a single layer of homogeneous thin cirrus clouds, with a fixed optical thickness (0.3), lies on top of the mineral dust layers. In addition, the particle size and shape of ice crystals composing thin cirrus are also prescribed in advance. The Deep Blue aerosol retrieval algorithm, which is introduced in details in section 2, is employed here for retrievals.

Here, a simple method based on the Normalized Difference Dust Index [Qu et al., 2006] is used to identify mineral dust from clouds. Suppose a pixel contaminated by very thin cirrus clouds is not properly identified, the LUT based on the dust only atmosphere should be used to retrieve the dust AOD. However, a more realistic dust AOD could be retrieved tentatively based on the LUT for the dust plus thin cirrus atmosphere. By

comparing these two sets of retrieved dust AOD, the effect of thin cirrus on the dust AOD retrieval is quantitatively described.

4.2 Dust detection methods

Although the detection of dust is often plagued by the occurrence of clouds, especially thin cirrus clouds [Roskovensky and Liou, 2005], several visible and IR channel techniques related to satellite remote sensing have been proposed for detecting mineral dust aerosols. Ackerman [1997] suggested a tri-spectral approach, which is based on the brightness temperature difference of three IR channels at the wavelengths 8.5, 11 and 12 μm, is possibly helpful to detect mineral dust aerosols. Sokolik [2002] implemented a bio-spectral approach to separate dust from clouds, which depends on a unique radiative signature of mineral dust (i.e., negative brightness temperature difference between MODIS 11 and 12 channels). Based on the dust spectrum characterization analysis, a promising indicator termed as NDDI (Normalized Difference Dust Index) was proposed to distinguish mineral dust from clouds by using MODIS solar reflectance data, with the assistance of brightness temperature at MODIS 11 μm band to separate airborne dust from ground features [Qu et al., 2006]. Hansell et al. [2007] suggested an integrated method for the simultaneous detection/separation of mineral dust aerosols and clouds using MODIS thermal infrared channels. However, all the methods mentioned before have their own limitations. For example, it has been demonstrated that the discrimination between dust aerosols and clouds based on the bio-spectral or tri-spectral approach with a fixed brightness temperature difference threshold is almost impossible due to the regional radiative signature of dust aerosols [Darmenov and

Sokolik, 2005]. The NDDI is working with different values of threshold for different regions, and the characteristic of NDDI for some low clouds may be similar to that for mineral dust aerosols over oceans [Wu et al., 2006], which greatly increases errors for dust detection. It is important to emphasize that the MODIS cloud mask (e.g., MOD35), which is employed in current operational aerosol retrievals, may permit heavy dust to escape detection and misclassify as clouds [Remer et al., 2005]. For simplicity, the NDDI dust detection method, which is based on the combination of the NDDI and the brightness temperature at MODIS 11 μm channel (BT11), is used here to separate mineral dust aerosols from clouds, since the test of different dust detection methods is beyond the scope of the current research. The fundamental principles and the technical details are referenced in Qu et al. [2006]. The NDDI can be defined as:

$$NDDI = (R_{2.13} - R_{0.47})/(R_{2.13} + R_{0.47}), \tag{28}$$

where $R_{2.13}$ and $R_{0.47}$ are the measured TOA reflectance in the MODIS 2.13 and 0.47 μm channels, respectively.

The reliability of NDDI for detecting mineral dust aerosols is demonstrated in Fig. 24 by analyzing the NDDI values for mineral dust aerosols and clouds. Fig. 24 (upper panel) clearly shows a RGB image of dust storm over Northern Asia from the MODIS data on March 27, 2004. The corresponding NDDI image is shown in the lower panel of Fig. 24, with negative value for clouds and positive value for airborne mineral dust aerosols and ground features. In order to separate airborne dust and ground features, the image of the brightness temperature for MODIS 11 μm band is analyzed, as shown in the upper panel of Fig. 25. It is obvious that the BT11 for airborne dust is cooler compared with that for ground features, and thus airborne dust can be separated from ground features by setting

a threshold for BT11, which is determined empirically. The lower panel of Fig. 25 shows the mineral dust detection results with a threshold for NDDI and BT11 0.28 and 275K, respectively. It should be emphasized that it is possible that some pixels contaminated by very thin cirrus clouds still cannot be identified successively, even though other robust cloud masks were employed. Here, we also examine the brightness temperature difference in the context of tri-spectral approach. The data from MODIS 8.5 μm, 11 μm, and 12 μm bands are used, and the brightness temperature difference between channels 8.5 μm and 11 μm ($BT_{8.5} - BT_{11}$) and channels 11 μm and 12 μm ($BT_{11} - BT_{12}$) are computed and analyzed. Shown in Fig. 26 are $BT_{8.5} - BT_{11}$ as well as $BT_{11} - BT_{12}$ images for the dust storm outbreak over Asian as indicated in the upper panel of Fig. 24. Most dust storm regions have positive $BT_{8.5} - BT_{11}$ and negative $BT_{11} - BT_{12}$, so that we can use the criteria of $BT_{8.5} - BT_{11} > 0$ and $BT_{11} - BT_{12} < 0$ to detect dust, although negative $BT_{8.5} - BT_{11}$ are also observed in some dust storm regions. Fig. 27 is similar to Fig 26 but for a dust storm over oceans as indicated in Fig. 19. As shown in this figure, $BT_{11} - BT_{12}$ can be positive and negative for dust regions, while for clear sky and cloudy areas $BT_{11} - BT_{12}$ are positive. The values of $BT_{8.5} - BT_{11}$ are always negative for dust storm and clear sky regions. In this case, we cannot use the criteria of $BT_{8.5} - BT_{11} > 0$ and $BT_{11} - BT_{12} < 0$ to detect dust regions. This behavior of brightness temperature difference has been already pointed out, and is probably due to the different mineralogical composition for different dust source regions [Darmenov et al., 2005]. In the present study, we still use the parameter of Normalized Difference Dust Index to identify mineral dust aerosol from clouds.

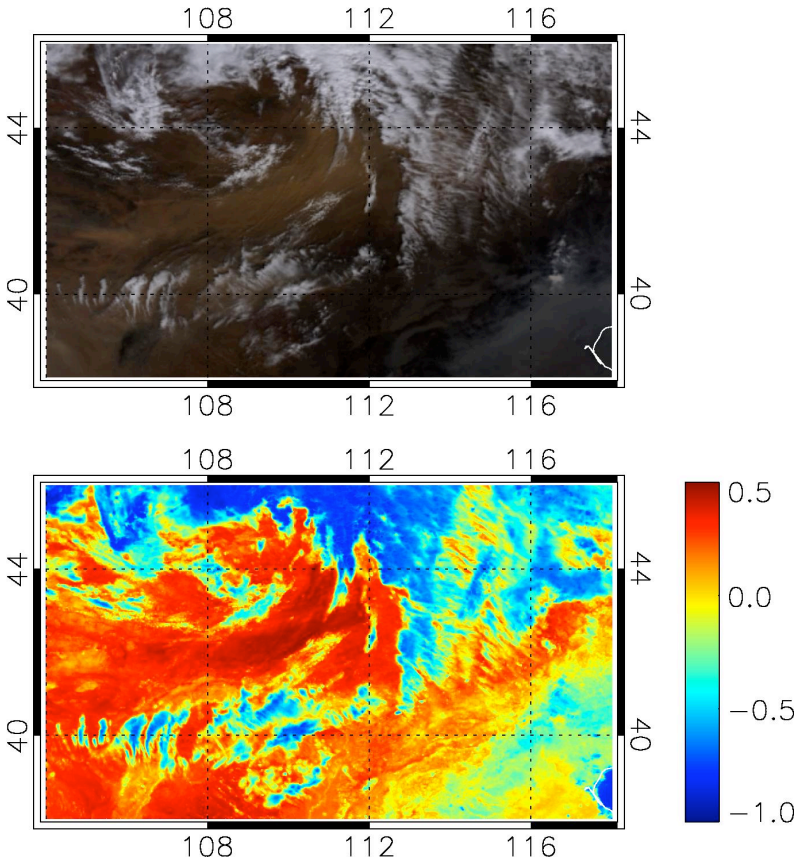

Fig. 24 Upper panel: MODIS RGB image on March 27, 2004 shows Asian dust storm over Northern China. Lower panel: MODIS NDDI image shows the differences between mineral dust aerosols and clouds.

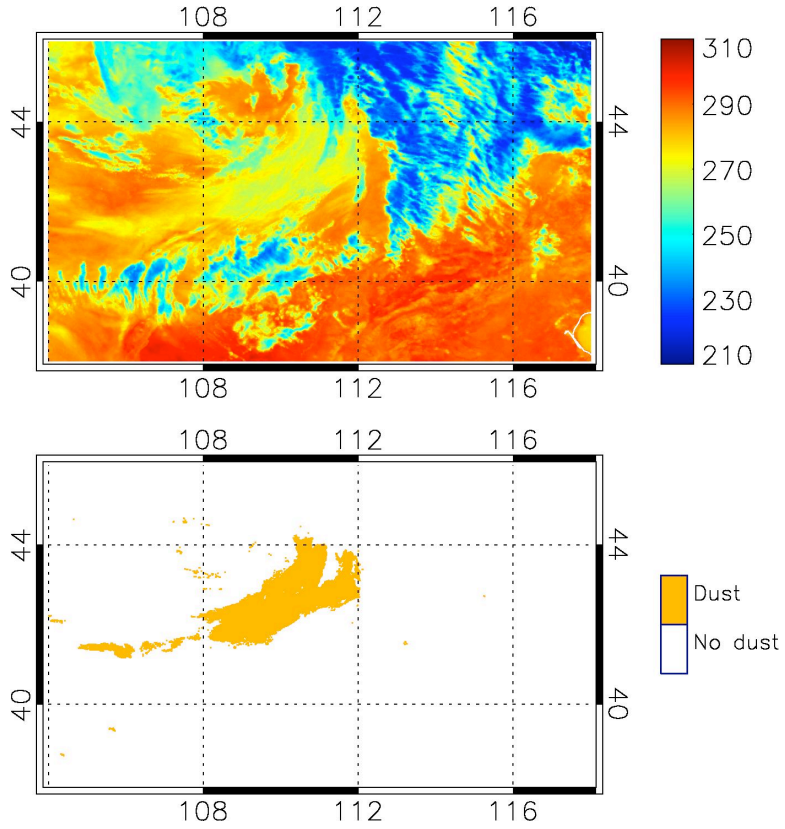

Fig. 25 Upper panel: brightness temperature (in K) image of MODIS 11 μm band over Northern China on March 27, 2004. Lower panel: the dust detection results (NDDI > 0.28 and BT11 < 275 K).

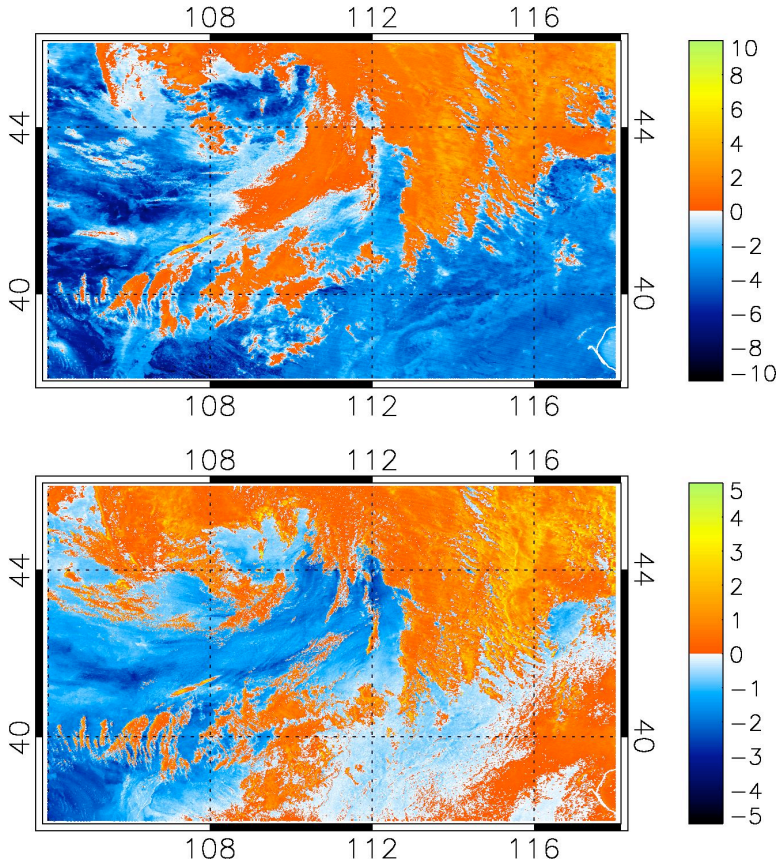

Fig. 26 Shown are the brightness temperature (in K) difference $BT_{8.5} - BT_{11}$ (upper panel) and $BT_{11} - BT_{12}$ (low panel) for a dust storm outbreak as indicated in the upper panel of Fig. 24.

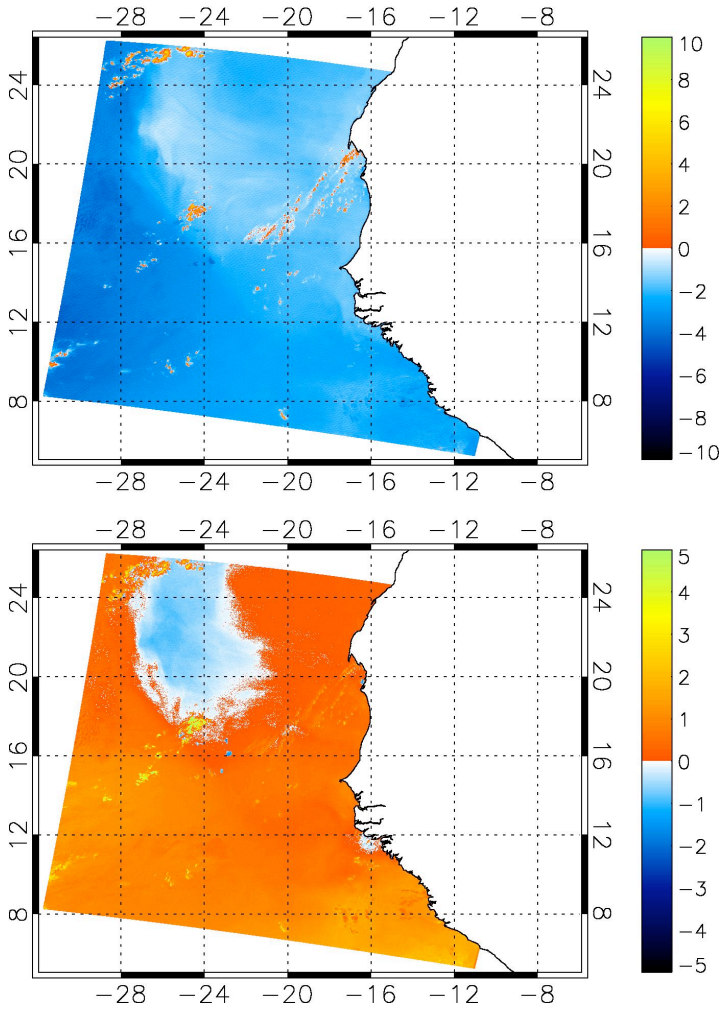

Fig. 27 Same plots as in Fig. 26 but for a dust storm over oceans as indicated in Fig. 19.

4.3 Bulk scattering properties for mineral dust and thin cirrus clouds

The bulk scattering properties for mineral dust aerosols for each Deep Blue channel are the same as those used in section 3. The effective radius and effective variance for mineral dust aerosols are still assumed to be 1.0 μm and 1.0, respectively. As for the thin cirrus clouds, the corresponding single-scattering properties are computed by using an improved geometric optics method [Zhang et al., 2004]. In situ measurements of cirrus clouds indicate that both the size and habit distribution of ice crystals composing cirrus may vary substantially within the clouds [Heymsfield et al., 2000]. Here, the droxtal, commonly used to represent the smallest ice particles, is employed here to approximate the particle shape of ice crystals for thin cirrus clouds. The gamma distribution, with an effective diameter of 20μm, is used for the size distribution of thin cirrus clouds. It should be noted that an extensive database of scattering properties has been built up for a set of ice particles including droxtals, hexagonal plates, hollow columns, bullet rosettes, and so on.

Fig. 28 shows the six nonzero elements of the phase matrix calculated at the wavelength of 0.412 μm for randomly oriented droxtal ice crystals. For comparison, the corresponding phase matrix elements for spheroidal mineral dust aerosols are also shown in this figure. The refractive index for droxtal ice crystals and mineral dust are $1.318+2.46175\times10^{-9}i$ and $1.55+0.002i$, respectively. Note that each phase matrix element for mineral dust aerosols is much smoother than that for droxtal ice crystals, since the particle shape for droxtal ice crystals is more complicated than that for spheroidal mineral dust aerosols. In addition, the forward scattering peak for droxtal ice crystals is much stronger than that for mineral dust aerosols. Such forward peaks typically require

thousands of expansion coefficients to represent the phase function in radiative transfer calculations. Subsequently, truncation of this forward peak is needed in order to reduce the number of terms for expansion. Here, truncation is performed on the phase function by using the method developed by Hu et al. [2000], referred to as δ-fit method. This method is an extension of delta-M method [Wiscombe, 1997], but uses least squares fitting procedure to minimize the differences between the actual phase function and the truncated phase function. Upon truncation of the phase function, the other phase matrix elements need to be scaled for consistency [Chami et al., 2001]. The single-scattering albedo and optical depth are scaled according to:

$$\varpi^* = \frac{(1-f)\varpi}{(1-\varpi f)} \tag{29}$$

$$\tau^* = (1-\varpi f)\tau \tag{30}$$

where f is the fraction of scattered energy due to the truncated peak.

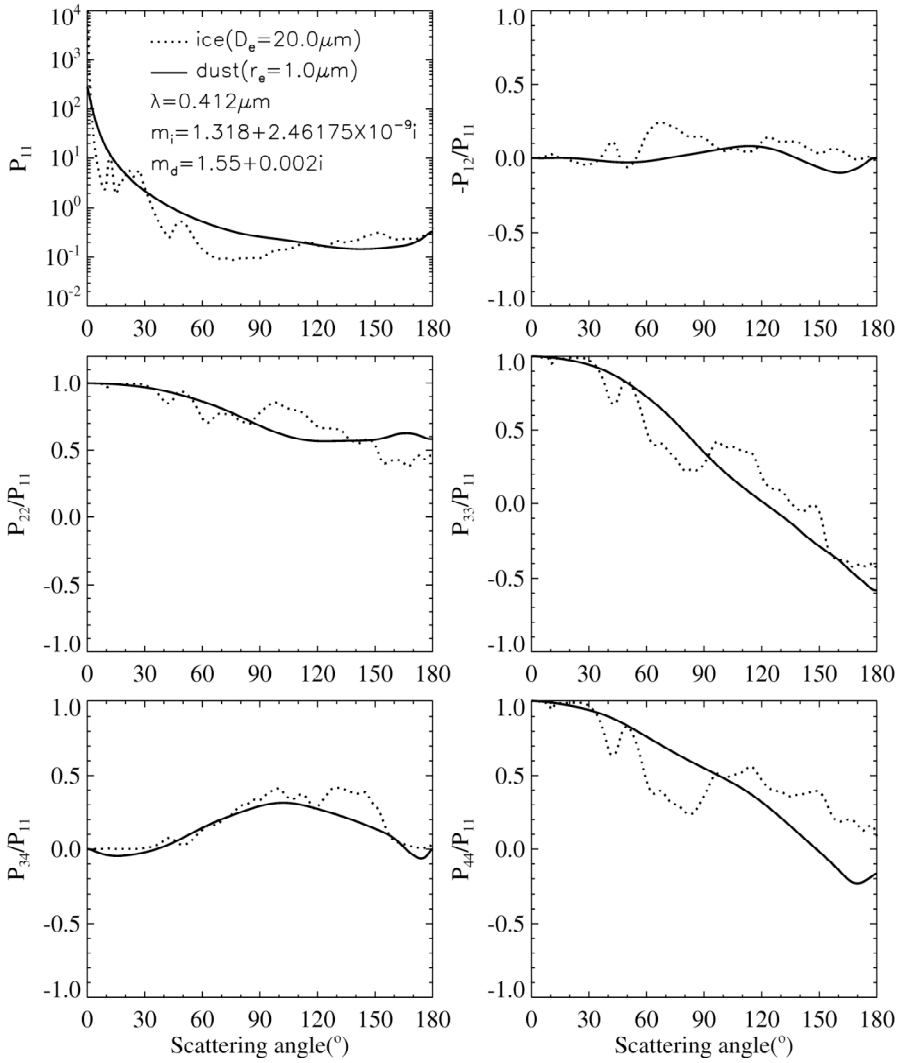

Fig. 28 Comparisons of the phase matrix calculated at the wavelength of 0.412 μm for randomly oriented droxtal ice crystals and spheroidal mineral dust aerosols.

4.4 The effect of thin cirrus on dust optical depth retrievals

As mentioned before, two different kinds of LUTs, similar to the aforementioned in section 3, are created to study the effect of thin cirrus clouds on dust AOD retrievals. One is for the dust only atmosphere, and the other is for the dust plus thin cirrus atmosphere. In the dust plus thin cirrus atmosphere, it is assumed that there is a single layer of homogeneous thin cirrus clouds with a height of 12 km, lying on top of mineral dust layers. The vertical distribution of mineral dust layers for these two kinds of atmosphere is the same as described in section 3.

Fig. 29 shows the relative differences of the TOA upward reflectances between the dust only and dust plus thin cirrus atmosphere, $(R_{dust\ plus\ thin\ cirrus} - R_{dust}) / R_{dust} \times 100\%$, as a function of satellite view zenith angles for different values of dust AOD and surface reflectance. The refractive index for mineral dust aerosols is assumed to be 1.55+0.003i. The solar zenith and relative azimuthal angles are 24° and 132°, respectively. Obviously, the relative differences of the TOA upward reflectances between the dust only and dust plus thin cirrus atmosphere are sensitive to the satellite view zenith angles.

It is also evident from Fig. 29 that the relative differences of the TOA upward reflectances between the dust only and dust plus thin cirrus atmosphere strongly depend on the values of dust AOD and underlying surface reflectance. As the dust AOD increases, the relative differences of the TOA upward reflectances between the dust only and dust plus thin cirrus atmosphere decrease.

Fig. 30 shows the polar plots of the TOA upward reflectances with different surface reflectances. The relative azimuthal angles are displayed from 0° to 360° in the counter-clockwise direction. The view zenith angles are measured from 0° to 66° in the radial direction. The solar zenith angle and the dust AOD are 24° and 0.5°, respectively. The corresponding relative differences of the TOA upward reflectances between the dust only and dust plus thin cirrus atmosphere are also shown in Fig. 30. It is also evident that the relative differences of the TOA upward reflectances between the dust only and dust plus thin cirrus atmosphere depend on the underlying surface reflectance.

Fig. 31 shows the calculated land surface reflectances (with a resolution of 0.1° latitude × 0.1° longitude) over North Asian at the MODIS 0.412, 0.470 and 0.650 μm channels by using the method introduced in section 3. Similarly, the surface reflectance over the Asian areas at 0.412 μm is much smaller than that at 0.650 μm.

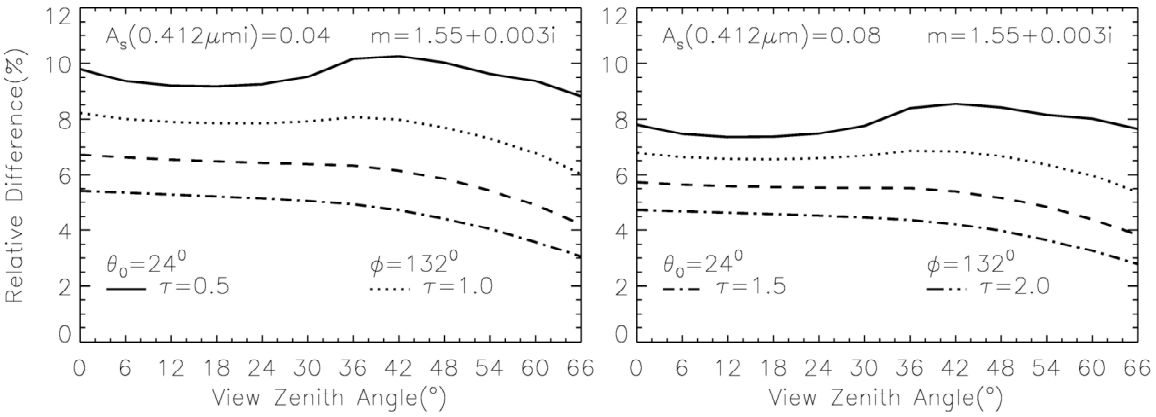

Fig. 29 The relative differences of the TOA upward reflectances between the dust only and dust plus thin cirrus atmosphere, as a function of satellite view zenith angles for different values of dust optical depth and surface reflectance. The surface reflectances for the left and right panels are 0.04 and 0.08, respectively.

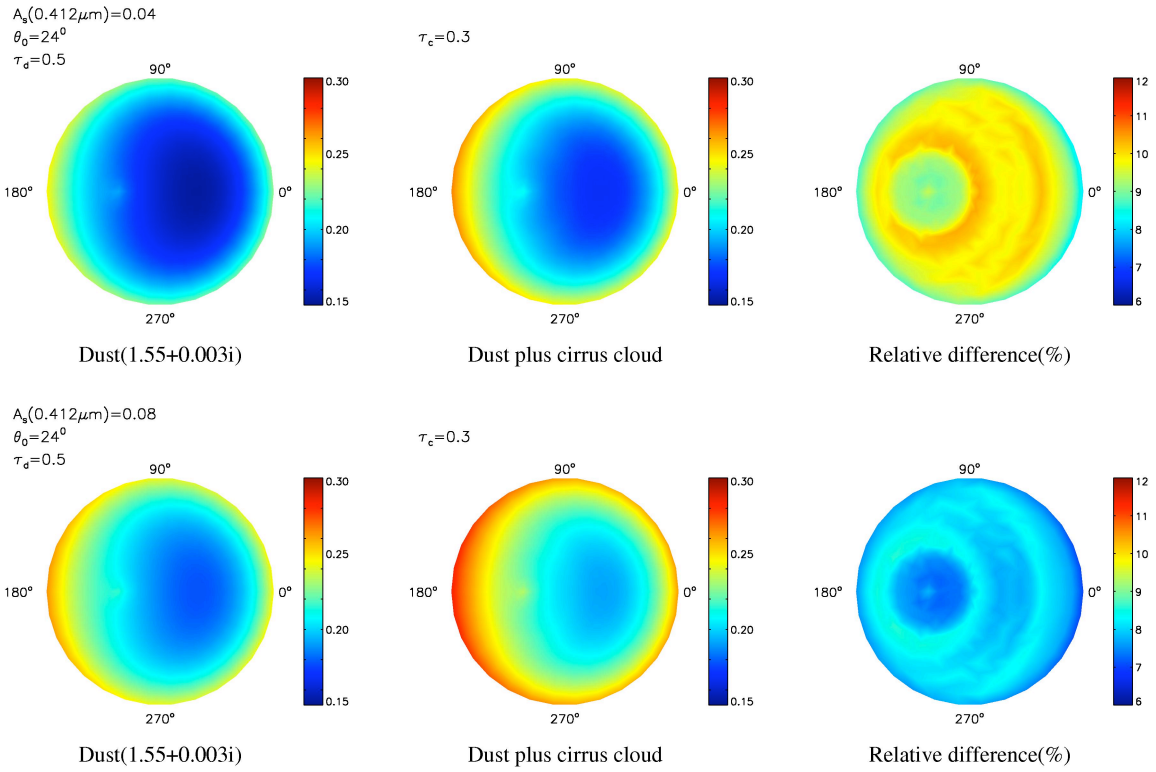

Fig. 30 Polar plots of the TOA upward reflectances for the dust only and dust plus thin cirrus atmosphere.

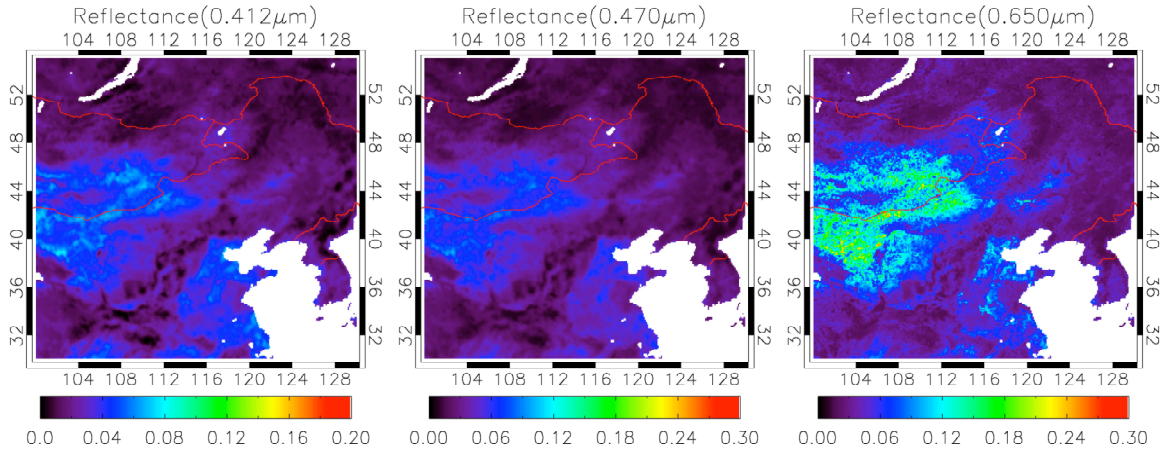

Fig. 31 Calculated surface reflectance database at 0.412, 0.470 and 0.65 μm channels over North Asia.

With the information of the surface reflectance and the LUTs for the dust only and dust plus thin cirrus atmosphere, the effect of thin cirrus on the retrieved dust optical depths can be discussed quantitatively. Fig. 32 shows the LUTs for the two-channel retrieval technique for the dust only and dust plus thin cirrus atmosphere. This figure, similar to Fig. 13, shows the relationship between the simulated TOA upward reflectances in the MODIS channels of 0.412 and 0.470 μm as a function of AOD for two kinds of dust aerosols. In this figure, the sun-satellite geometry in the upper panel is different from that in the lower panel. Obviously, the LUT for the two-channel retrieval technique based on the dust only atmosphere is quite different from that based on the dust plus thin cirrus atmosphere. If satellite measured radiances are contaminated due to undetected very thin cirrus cloud, then the LUT based on the dust only atmosphere is used to retrieve the dust optical depths. However, more realistic dust optical depths should be retrieved approximately based on the LUT for the dust plus thin cirrus atmosphere. It is not surprising that the differences in the LUTs between the dust only and dust plus thin cirrus atmosphere lead to an inconsistency in the retrieved dust AOD. For example, the dust AOD retrieved by LUT for the dust plus thin cirrus atmosphere should be smaller than that retrieved by LUT for the dust only atmosphere, especially for very low dust loading conditions. Under heavy dust loading conditions, the differences in the retrieved dust AOD between the dust only and dust plus thin cirrus atmosphere are smaller than those for low dust loading conditions. Note that the optical depth and scattering properties for thin cirrus clouds in the dust plus thin cirrus atmosphere are prescribed a priori, although the realistic optical properties (e.g., optical depth) for thin cirrus clouds are often unknown.

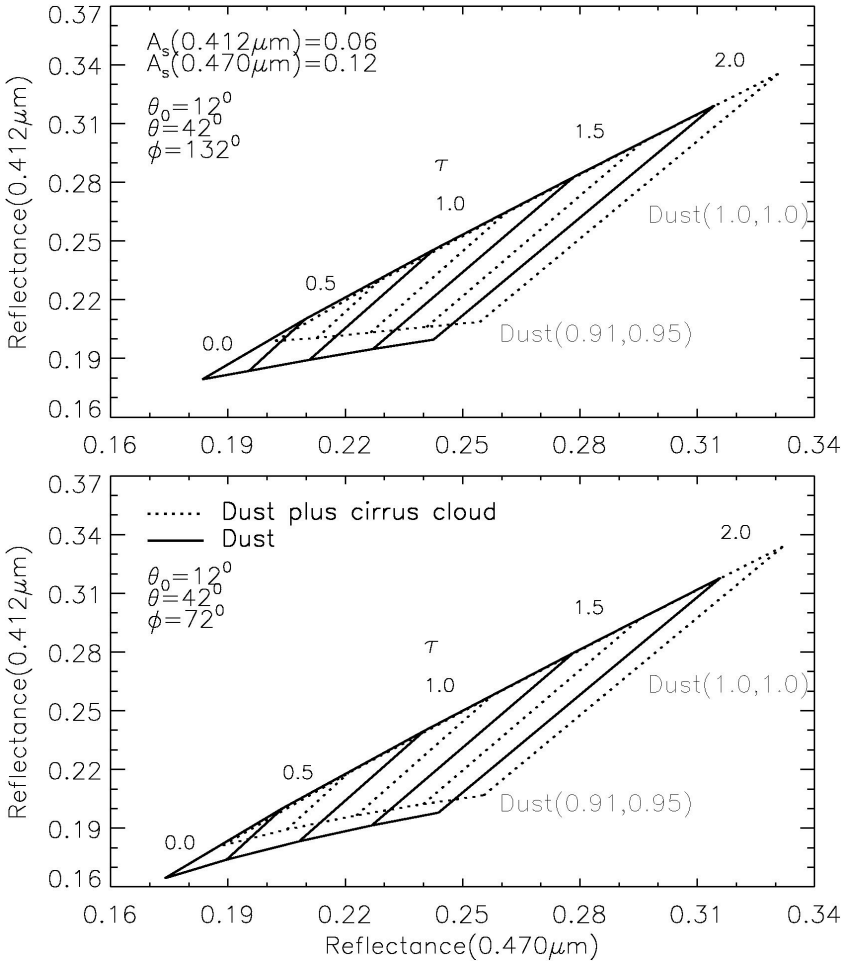

Fig. 32 Same plots as in Fig. 13 but for the dust only and dust plus thin cirrus atmosphere. In addition, the sun-satellite geometry associated with Fig. 13 and Fig. 32 is also different. Upper panel has relative azimuthal angle (ϕ) equal to 132°, while lower panel has ϕ equal to 72°. The optical depth and effective diameter for thin cirrus clouds are 0.3 and 20 μm, respectively.

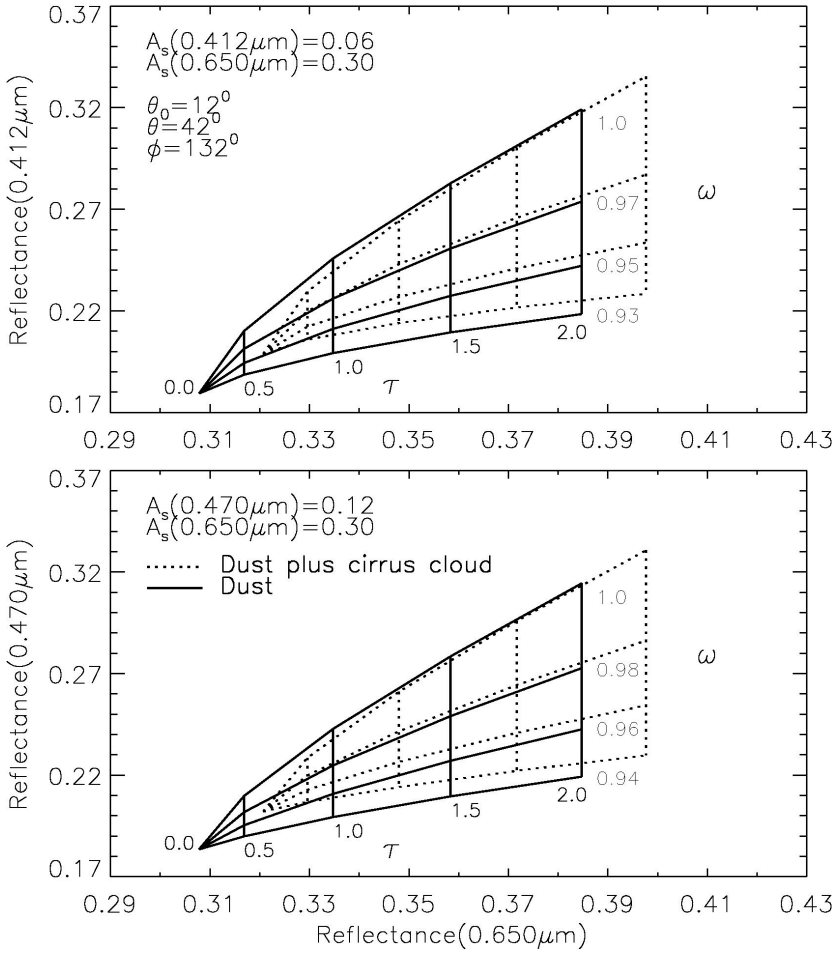

Fig. 33 Similar to Fig. 14 but for the comparison between the dust only and dust plus thin cirrus atmosphere. The more horizontal curves represent different values of single-scattering albedo.

Fig. 33 shows the LUTs for the three-channel retrieval technique for the dust only and dust plus thin cirrus atmosphere. Similar to Fig. 14, this figure describes the correlations between the reflectances at the MODIS 0.412 and 0.650 μm channels (upper panel) and between the reflectance at the MODIS 0.470 and 0.650 μm channels (low panel) for various dust AOD and single scattering albedos. The values for single scattering albedo indicated in the figure are for 0.412 μm (upper panel) and 0.470 μm (lower panel). The single scattering albedo for 0.650 μm is 1.0. The overall features of Fig. 33 for the differences between the LUTs for the dust only and dust plus thin cirrus atmosphere are the same as shown in Fig. 32, that is, the dust AOD retrieved by LUT for the dust plus thin cirrus atmosphere should be smaller than that retrieved by LUT for the dust only atmosphere, especially for low dust loading conditions. Under heavy dust conditions, the differences in the retrieved dust AOD between the dust only and dust plus thin cirrus atmosphere are smaller than those for low dust loading conditions.

For the present sensitivity study, we focus on the MODIS observation as indicated in Fig. 34. Fig. 34 (upper panel) shows a RGB image of dust storm over Mongolian regions from the MODIS data on May 27, 2008. The corresponding NDDI image, shown in the lower panel of Fig. 34, clearly indicates the NDDI values for clouds are different from those for airborne mineral dust and ground features. For pixels with NDDI values larger than 0.28, the two aforementioned LUTs are used to retrieved dust AOD based on the principle of Deep Blue algorithm. Fig. 35 (upper panel) shows the retrieved dust AOD based on the LUT for dust only atmosphere. The corresponding retrieval results, based on

the LUT for dust plus thin cirrus atmosphere, are shown in the lower panel of Fig. 35. Note that we neglect negative retrieved dust AOD, which results from the cloud-uncontaminated pixels but with the LUT based on the dust plus thin cirrus atmosphere for retrievals. The comparison of the retrieved dust AOD between different LUTs is shown in Fig. 36. The histogram of the retrieved dust AOD, as indicated in the upper panel of Fig. 36 shows the obvious differences for these two retrieval datasets. Furthermore, plotted in the lower panel of Fig. 36 are the absolute errors ($\tau_{dust} - \tau_{dust\ plus\ thin\ cirrus}$) as a function of retrieved dust AOD based on LUT for the dust plus thin cirrus atmosphere. Obviously, the failure to identify cloud-contaminated pixels, even contaminated by very thin cirrus clouds, may lead to larger errors in the retrieved dust AOD. At low dust loading conditions, the absolute errors can reach up to 0.5, which is larger than the assumed optical depth for thin cirrus. While at heavy dust loading conditions, the absolute errors are comparable to the assumed value (0.3) for thin cirrus optical depth.

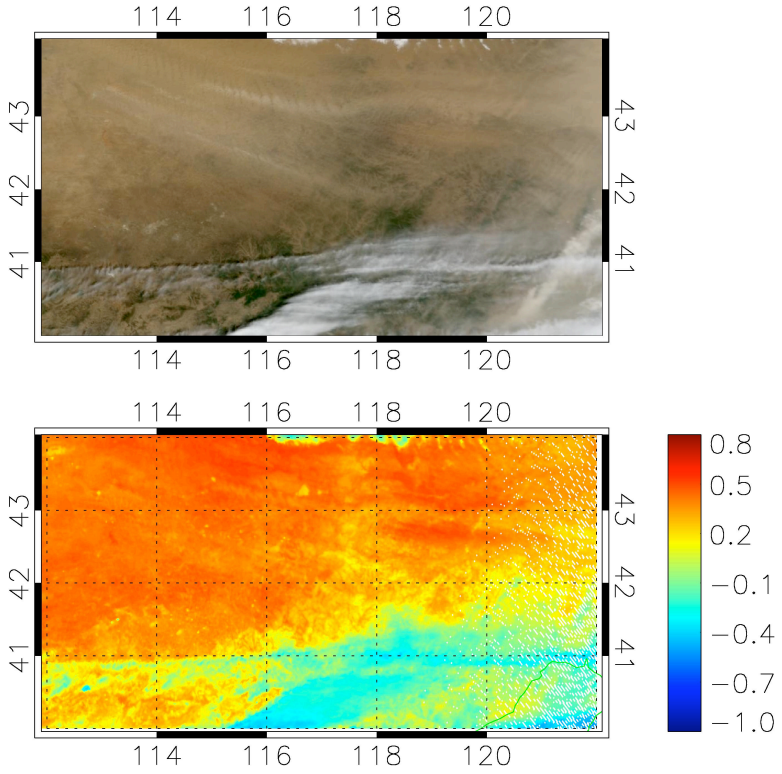

Fig. 34 Upper panel: MODIS RGB image on May 27, 2008 shows Asian dust storm over Mongolian regions. Lower panel: MODIS NDDI image shows the differences between mineral dust aerosols and clouds.

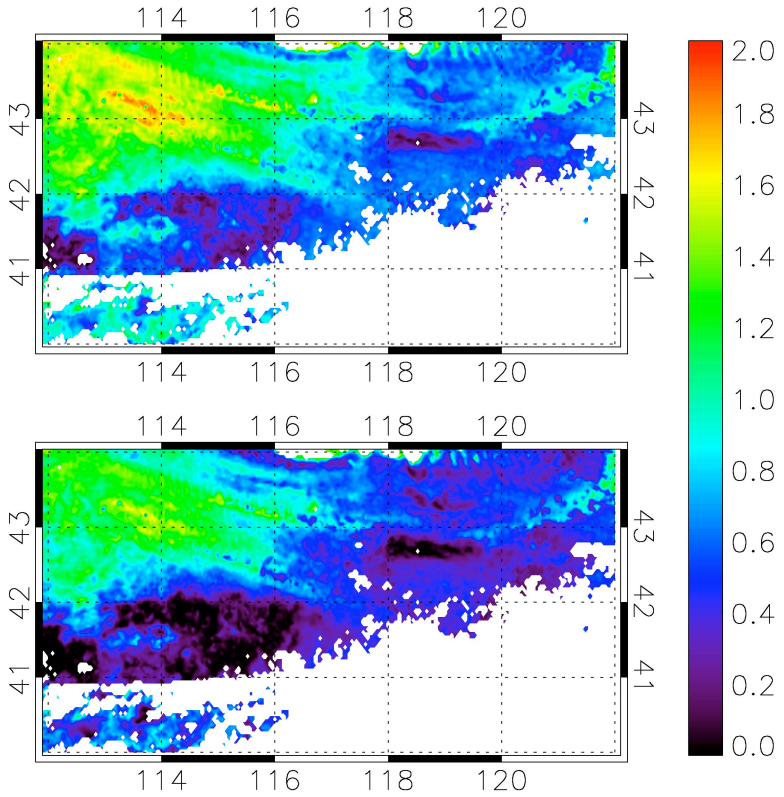

Fig. 35 Retrieved dust AOD corresponding to LUT based on the dust only atmosphere (upper panel) and LUT based on the dust plus thin cirrus atmosphere (lower panel).

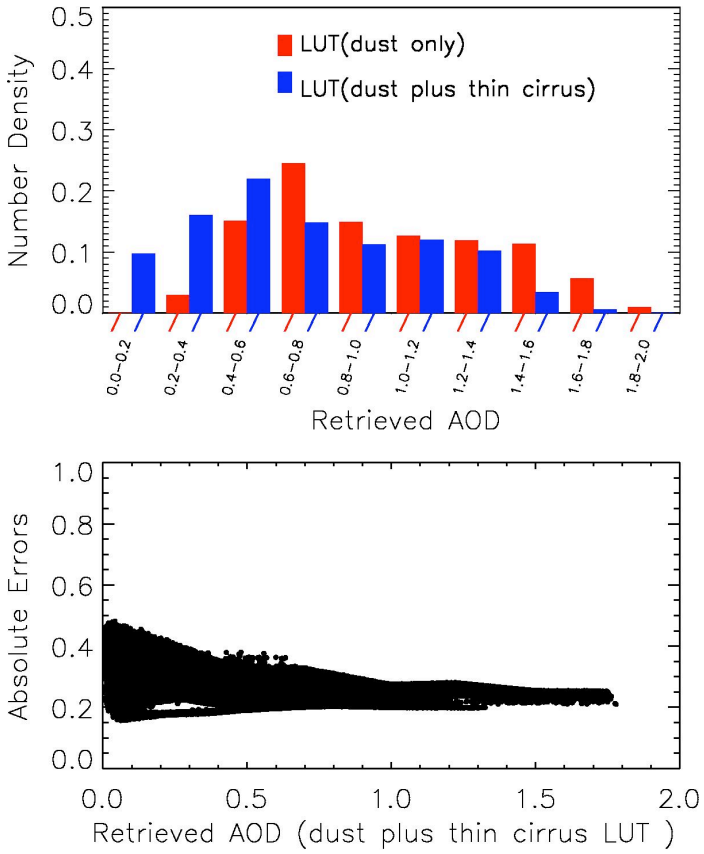

Fig. 36 Upper panel: the histogram of retrieved dust AOD based on the LUTs for the dust only and dust plus thin cirrus atmosphere, respectively. Lower panel: the absolute errors of the retrieved dust AOD.

4.5 Summary

The sensitivity study as to the effect of thin cirrus clouds on dust optical depth retrievals has been investigated and quantified from MODIS observations. The dust optical depths are retrieved based on a simplified aerosol retrieval algorithm based on the approach of the Deep Blue aerosol retrieval algorithm. The importance of identifying thin cirrus clouds in dust optical depth retrievals is highlighted. This has been undertaken through the comparison of retrieved dust optical depths by using two different lookup tables. One is for the dust only atmosphere, and the other is for the atmosphere with overlapping mineral dust and thin cirrus clouds. For simplicity, the optical depth and scattering properties for cirrus clouds are prescribed a priori. The present sensitivity study indicates the failure to identify pixels contaminated by thin cirrus clouds may lead to larger errors in the retrieved dust optical depths. Under heavy dust conditions, the errors in the retrieved dust optical depths due to the effect of thin cirrus are comparable to the assumed optical depth for cirrus clouds.

5. THE EFFECT OF PARTICLE SHAPES ON SHORTWAVE DIRECT RADIATIVE FORCING CALCULATIONS FOR MINERAL DUST

5.1 Methods

The effect of particle shapes on the dust direct radiative forcing calculations is estimated based on Fu-Liou radiative transfer model. Here, we only investigate the effect of particle shapes on the instantaneous TOA shortwave (SW) direct radiative forcing by mineral dust aerosols (hereafter referred to as instantaneous TOA SWRF), since the effect of particle shapes becomes less important in the longwave spectral regions due to the relatively small particle size parameters. In this study, the effect of particle shapes on the dust radiative forcing is illustrated in the following two aspects. First, without considering the effect of particle shapes on the dust AOD retrievals (see section 3), the effect of particle shapes on the single-scattering properties of dust aerosols, hence on the dust direct radiative forcing is assessed. Second, the effect of particle shapes on the dust direct radiative forcing is further discussed by including the effect of particle shapes on the dust AOD retrievals.

5.2 Scattering property simulations

Radiative forcing simulations for mineral dust aerosols depend on the single-scattering properties of dust aerosols (e.g., extinction efficiency Q_e, asymmetry factor g, and single-scattering albedo ω) and the optical depth τ, while the single-scattering properties of dust aerosols are related to the particle size, particle shape and refractive index. In the meanwhile, dust optical depth retrievals based on remote sensing techniques

also depend on the single-scattering properties of dust particles. That is to say, single-scattering properties of dust aerosols are at the heart of atmospheric dust retrievals and associated direct radiative forcing calculations.

Owing to the robust scattering-computational methods, we are now in a good position to evaluate the effect of particle shapes on the dust radiative forcing calculations, especially for shortwave spectral regions. As mentioned before, a spheroidal particle shape assumption has been widely employed in the simulation of scattering properties for nonspherical dust particles, although naturally occurring mineral dust aerosols have a great variability of particle shapes. Here, Q_e, g and ω are simulated separately by use of the spheroidal and spherical particle shape assumptions with ancillary information on the particle size and refractive index. In the present study, the particle size distribution for mineral dust is still specified in terms of lognormal function with an effective radius of 1.0 μm. 1000 size bins in term of volume equivalent sphere radius ranging from 0.02 to 20.0 μm are considered. The refractive index database for mineral dust aerosols in the solar spectral range is taken from d'Almeida et al. [1991]. The real and imaginary parts of the refractive index for mineral dust aerosols are shown in Fig. 37 as functions of wavelength ranging from 0.25 μm to 4.0 μm. It is evident that the real parts of the refractive index do not show a spectral dependence, whereas the imaginary parts have a strong spectral-dependence in the spectral regions shown here.

Similar to the methods used in section 2, we use the T-matrix method to derive the single-scattering properties for small and moderate size particles, whereas the improved geometric optics method (IGOM) is employed for large size particles. According to the aforementioned definition of aspect ratio for spheroidal particles, typical measured aspect

ratios for mineral dust aerosols range between 1.7 and 2.0 [Nakajima et al., 1989], i.e., prolate particle shape dominates in an ensemble of mineral dust aerosols. Since we are concerned here with the effect of particle shape on dust direct radiative forcing, it is sufficient to consider a simplified particle shape distribution for nonspherical dust aerosols. Here we assume dust particles to be a mixture of randomly oriented prolate spheroids with an aspect ratio equal to 1.7. This assumption is consistent with the goal of the current research, i.e., to study the effect of particle shape on dust radiative forcing calculations.

The asymmetry factor g is derived for each particle shape assumption and for each wavelength from the corresponding phase function via the following integral

$$g = \frac{1}{2}\int_0^{\pi} p(\Theta)\cos(\Theta)\sin(\Theta)d\Theta. \tag{31}$$

The asymmetry factor ranges from –1 to 1, with positive values for particles that scatter predominantly in the forward direction and negative values for backscattering predominantly particles. For symmetric phase functions, the asymmetry factor is zero. Fig. 38 shows the bulk scattering properties (mean extinction efficiency, single-scattering albedo and asymmetry factor) for spherical and nonspherical (spheroid with aspect ratio of 1.7) mineral dust particles in the spectral region from 0.25 to 4.0 μm. As evident in Fig. 38, the differences of their extinction efficiency, single-scattering albedo and asymmetry factor between the spheroidal and spherical particles are quite small. The relative errors due to the use of spherical particles to represent spheroidal particles are less than 1% for extinction efficiency and single-scattering albedo, and 2% for asymmetry factor. These results seems to be consistent with the statements suggested by Mishchenko et al., [1995] that the effect of particle shape on the dust radiative forcing

can be negligible and Mie theory can be used for computation, if the dust AOD is already known. In addition, it is also evident that the asymmetry factors for spheroidal particles is always larger that those for spherical particles, which means that the spheroidal particles scatter more energy in the forward hemisphere when compared with the spherical particles.

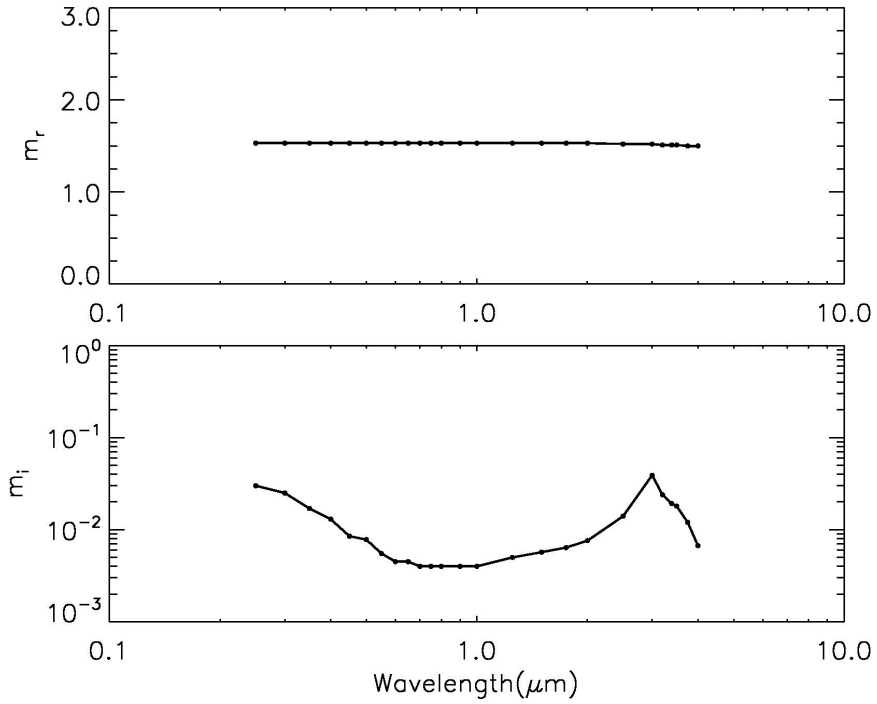

Fig. 37 Real and imaginary parts of the refractive index for mineral dust aerosols [d'Almeida et al., 1991].

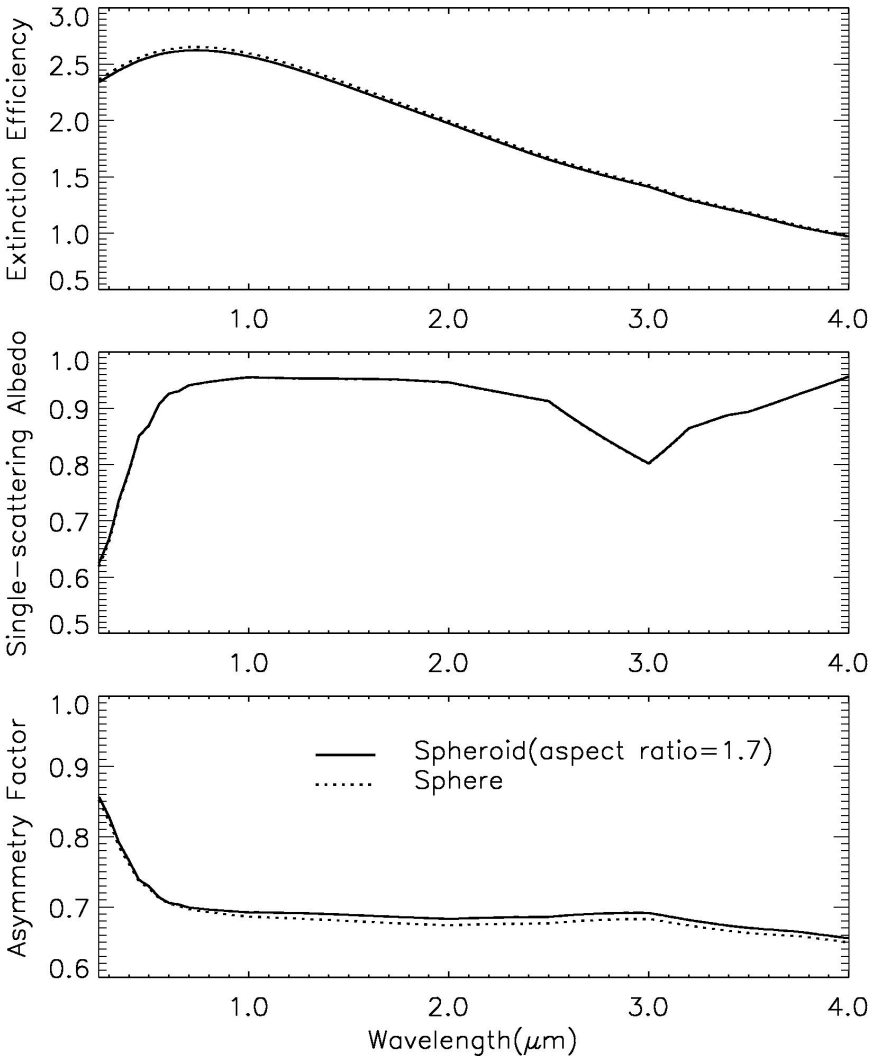

Fig. 38 The comparison of bulk scattering properties (mean extinction efficiency, single-scattering albedo and asymmetry factor) for spherical and nonspherical mineral dust particles in the spectral region ranging from 0.25 to 4.0 μm. The effective radius and effective variance for dust aerosols are assumed to be 1.0 μm and 1.0, respectively.

5.3 Radiative forcing simulations

The Fu-Liou radiative transfer model is used to calculate the hemispherical SW fluxes at TOA. The atmosphere is divided into 34 layers. Vertical profiles of temperature, pressure, ozone, and water vapor mixing ratios are from the standard mid-latitude atmosphere (1976). Note that we use the model only for cloud-free conditions. For each solar spectral band in the radiative model, the averaged single scattering albedo ϖ is calculated by integrating over band as follows:

$$\varpi = \int S(\lambda)\omega(\lambda)d\lambda / \int S(\lambda)d\lambda, \tag{32}$$

where $S(\lambda)$ is the solar spectrum at the top of the atmosphere. The band averaged asymmetry factor and extinction efficiency are also obtained this way. Then, the single-scattering properties related to the spheroidal and spherical particle shape assumptions over each solar spectral band are used as input to radiative transfer simulations. The instantaneous TOA SWRF by mineral dust aerosols is defined as:

$$\Delta F = F_{TOA}^{c} \uparrow - F_{TOA}^{d} \uparrow, \tag{33}$$

where ΔF is the instantaneous TOA SWRF, $F_{TOA}^{c} \uparrow$ and $F_{TOA}^{d} \uparrow$ are the upward SW flux at TOA for clear sky and dust atmosphere conditions, respectively. If $F_{TOA}^{d} \uparrow$ is larger than $F_{TOA}^{c} \uparrow$, then dust aerosols produce a cooling effect and vice versa.

Here, the Fu-Liou radiative transfer model is validated for Rayleigh scattering atmosphere by use of Clouds and the Earth's Radiant Energy System (CERES) data. As described in details in Loeb et al. [2005], the CERES instrument measures broadband radiances at the top of atmosphere for the total (0.3-200μm), shortwave (0.3-5μm) and infrared window (8-12μm) channels with a spatial resolution of 20km at the nadir. The CERES/MODIS SSF product, based on the synergy of MODIS aerosol/cloud properties

and the CERES TOA fluxes, contains MODIS aerosol optical depth within the CERES footprint. One year (2005) of merged Terra CERES/MODIS SSF product confined to the global cloud-free ocean areas between 60°S and 60°N is used. Due to the large errors in MODIS aerosol retrievals at low aerosol load conditions, it is very difficult to get the information about the TOA upward SW flux with zero optical depth. Thus, the instantaneous TOA upward SW flux in the absence of aerosols and clouds is inferred from the linear relationship between TOA upward SW flux and low aerosol optical depths for each solar zenith angle, as indicated by the following formula [Christopher and Zhang, 2002],

$$SWF = F_{clr} + slope \times \tau_{0.55}, \tag{34}$$

where SWF is the measured TOA upward SW flux for cloud free condition, F_{clr} is defined as the TOA SW flux in the absence of aerosols and clouds, $\tau_{0.55}$ is the MODIS retrieved optical depth at 0.55 μm. Fig. 39 shows the scatter plots of CERES SSF TOA upward SW fluxes as a function of SSF MODIS aerosol optical depths (0.55 μm) for different solar zenith angles. The corresponding linear regression line is also showed. The value of F_{clr} is then derived by extrapolation the linear regression back to zero optical depth conditions. Fig. 40 indicates the simulated clear sky SW albedos, which is equal to the ratio between the instantaneous TOA upward SW flux and the incident solar flux for clear sky conditions, at the top of atmosphere as a function of solar zenith angles at three different wind conditions based on the Fu-Liou radiative transfer model. The corresponding results (open circles) inferred from CERES are also shown. It is evident from Fig. 40 that the TOA SW albedos between the simulated results and the CERES measurement results match very well, especially at smaller solar zenith angles.

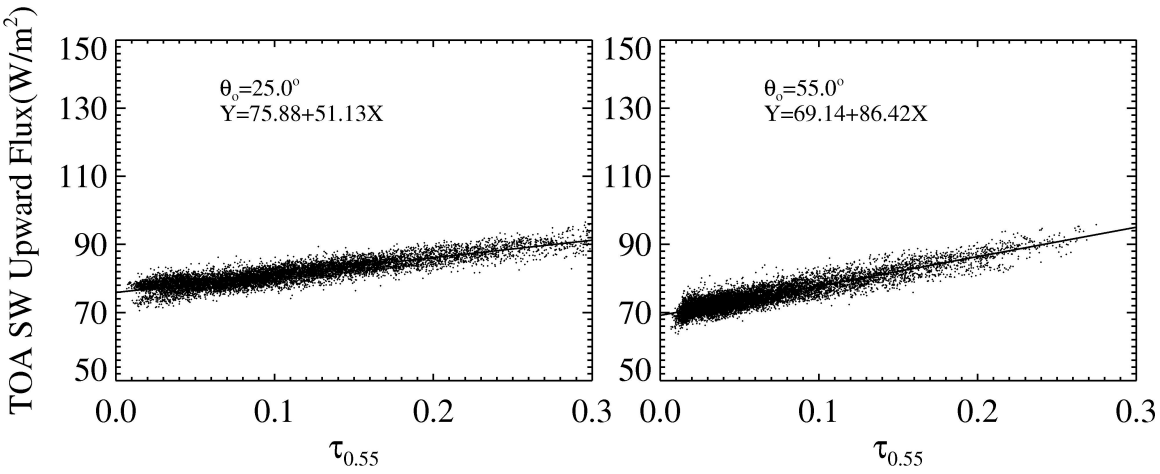

Fig. 39 Scatter plots of CERES SSF TOA SW upward flux as a function of SSF MODIS aerosol optical depth (0.55 μm) for different solar zenith angles. The corresponding linear regression line is also showed.

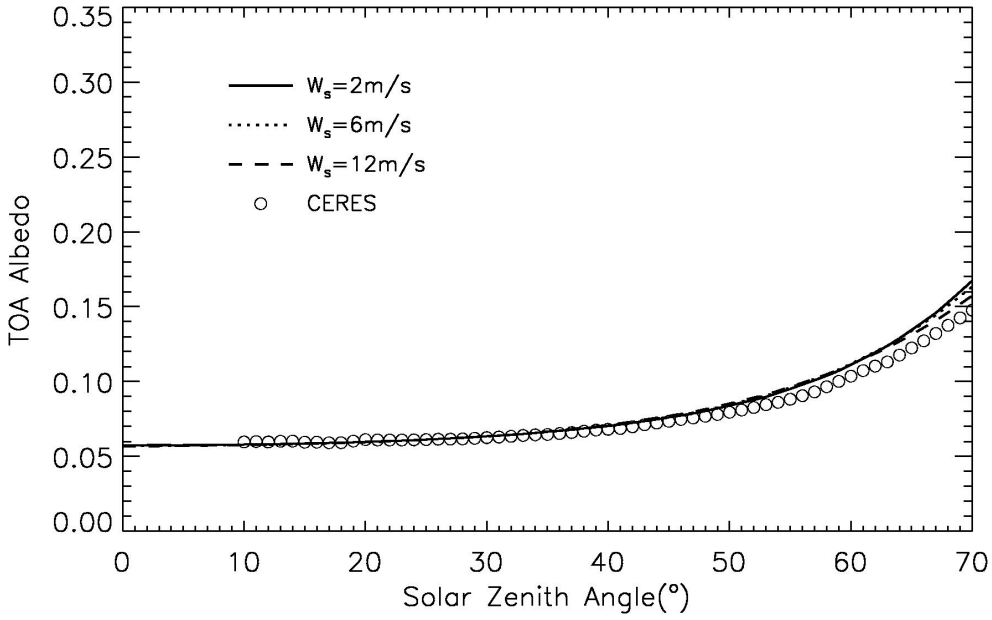

Fig. 40 Simulated clear sky SW albedos at the top of atmosphere as a function of solar zenith angles at three different wind conditions by using Fu-Liou model. The corresponding results (open circles) inferred from CERES are also shown.

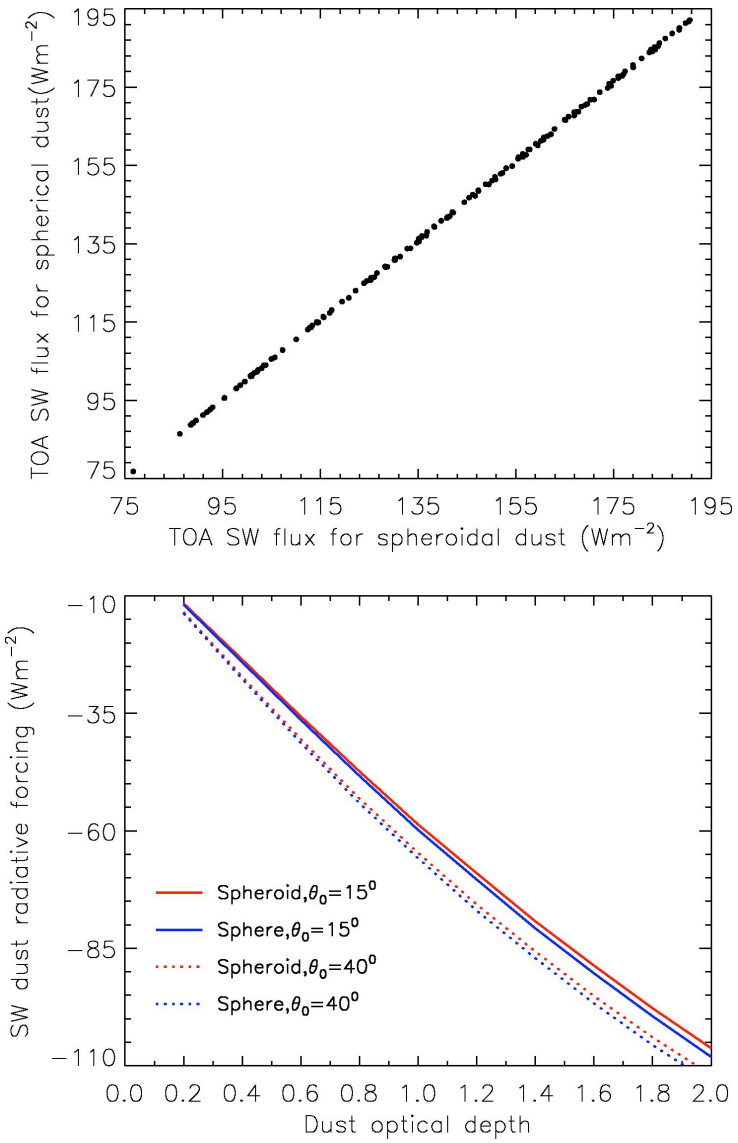

Fig. 41 (Upper panel) TOA SW fluxes for spheroidal dust versus TOA SW fluxes for spherical dust over dark surface. (Lower panel) Simulated SW dust radiative forcing with spheroidal and spherical particle shape assumptions, as a function of dust optical depths for different solar zenith angles.

5.4 Sensitivity study of the effect of particle shapes on dust direct radiative forcing

As mentioned before, the following two aspects related to the effect of dust particle shapes on the instantaneous TOA SWRF would be discussed here. First, we will study the effect of particle shapes on the instantaneous TOA SWRF by only including the effect of particle shapes on the scattering property simulations (e.g., extinction efficiency, single-scattering albedo and asymmetry factor). That is to say, the effect of particle shape on the retrieved dust optical depths is not taken into account in the radiative forcing calculations. With the scattering properties based on the spheroidal and spherical particle shape assumptions, the TOA upward SW fluxes for a dust atmosphere are calculated for different dust optical depths (τ=0.2 to 2.0) and different solar zenith angles. We set the oceans with surface wind speed of 6m/s as the underlying surface, which corresponds to a dark surface albedo. Fig. 41 (upper panel) shows the scatter plots of the TOA upward SW fluxes for a dust atmosphere with the spheroidal particle shape assumption versus the corresponding results with the spherical particle shape assumption. Obviously, there are almost no differences between the TOA upward SW fluxes computed from the spherical and spheroidal particle shape assumptions, which means that the TOA upward SW fluxes for a dust atmosphere are not sensitive to the dust particle shape, if the dust optical depths are the same for both particle shape assumptions. In the meanwhile, we also calculate the TOA upward SW fluxes for zero aerosol optical depth, from which the instantaneous TOA SWRF are derived according to Eq. (33). An example of the instantaneous TOA SWRF with the spheroidal and spherical particle shape assumptions, as a function of dust optical depth for different solar zenith angles, is shown in the lower panel of Fig. 41. The solid and dotted lines shows the TOA instantaneous SWRF with solar zenith angles of

15° and 40°, respectively. The red color is for the dust aerosols with spheroidal shape assumption, while the blue color is for spherical dust particles. It is evident that the instantaneous TOA SWRF for mineral dust is not sensitive to the particle shape assumption provided the dust optical depths are already known, which is consistent with the statements suggested by Mishchenko et al. [1995] and Fu et al. [2009]. The differences of the instantaneous TOA SWRF between the spherical and spheroidal particle shape assumptions are less than 1.0 Wm^{-2}. However, the instantaneous TOA SWRF is sensitive to the solar zenith angle, and the magnitude of the instantaneous TOA SWRF for solar zenith angle of 40° is larger than that for solar zenith angle of 15°.

Second, we will take the sensitivity study as to the effect of particle shapes on the dust radiative forcing by including the effect of particle shape on the dust optical depth retrievals, since the retrieved dust AOD based on the spheroidal particle shape assumption can be either larger or smaller than that retrieved based on the spherical particle shape assumption depending on scattering angles. The detailed discussion about the effect of particle shapes on the dust optical depth retrievals is referred to section 3. Here, the retrieved dust optical depths based on the spheroidal and spherical particle shape assumptions, as well as the averaged scattering properties for each spectral band, are employed as input to the FU-Liou radiative transfer code. It should be emphasized that it is assumed the scattering properties of dust aerosols used in the retrieval algorithm are consistent with those shown in Fig. 38.

Fig. 42 shows the instantaneous TOA SWRF over land (dark surface) as a function of solar zenith angles for two different dust optical depths. Here, the surface albedo is assumed to be 0.05. The red (blue) error bars represent the dust radiative forcing

uncertainties due to 10% (5%) errors in optical depth retrievals due to the different particle shape assumption. For different values of dust optical depth, the strongest instantaneous TOA SWRF occurs when the solar zenith angle is 65°-75° despite the decrease in the incident solar flux as the solar zenith angle increases. This means that as the solar zenith angle increases, a larger portion of the radiation scattered in the forward atmosphere is included in the upward scattered irradiance. Shown in Fig. 43 are the same plots as in Fig. 42 but for a different surface albedo with value of 0.15. In this case, the magnitude of the TOA instantaneous SWRF decreases, when compared with the corresponding result as indicated in Fig. 42. It is evident from Fig. 42 and Fig. 43 that the instantaneous TOA SWRF uncertainties due to the use of spherical particles to approximate spheroidal particles cannot be neglected, depending on the surface reflectance, dust AOD, and solar zenith angle.

Fig. 44 shows the spatial distribution of retrieved dust AOD based on the spheroidal and spherical particle shape assumptions, as well as the corresponding instantaneous TOA SWRF for different surface albedos. Due to the differences of the retrieved dust AOD between the spheroidal and spherical particle shape assumptions, the differences between the corresponding instantaneous TOA SWRF are also obvious. The spatial distribution of the retrieved dust AOD and the simulated instantaneous TOA SWRF are consistent, and regions with high dust AOD correspond to high magnitude of instantaneous TOA SWRF. In addition, it should be noted that as the surface albedo increases, the magnitude of the instantaneous TOA SWRF decreases, and the differences of the instantaneous TOA SWRF between the spheroidal and spherical particle shape assumptions also decrease.

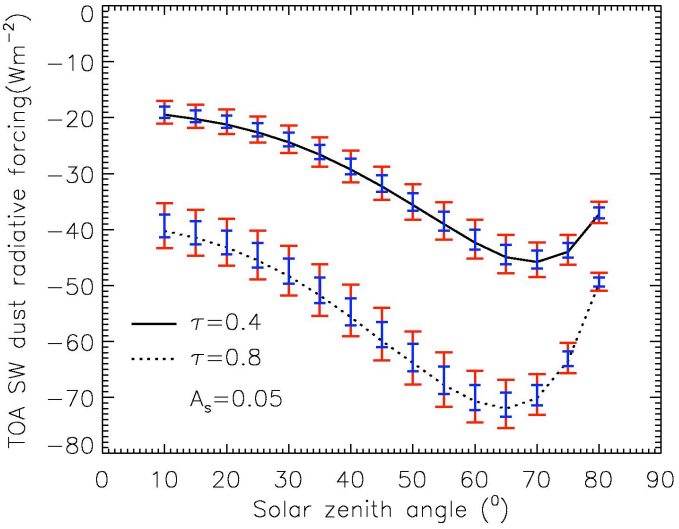

Fig. 42 TOA SW dust radiative forcing over dark surface with a surface albedo of 0.05, as a function of solar zenith angles for two different optical depths. The red (blue) error bars represent the dust radiative forcing uncertainties due to 10% (5%) errors in optical depth retrievals.

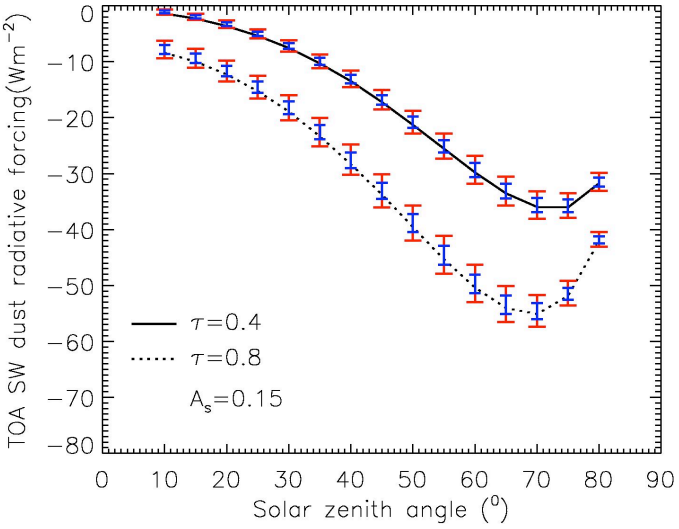

Fig. 43 Same plots as in Fig. 42 but for a different surface albedo.

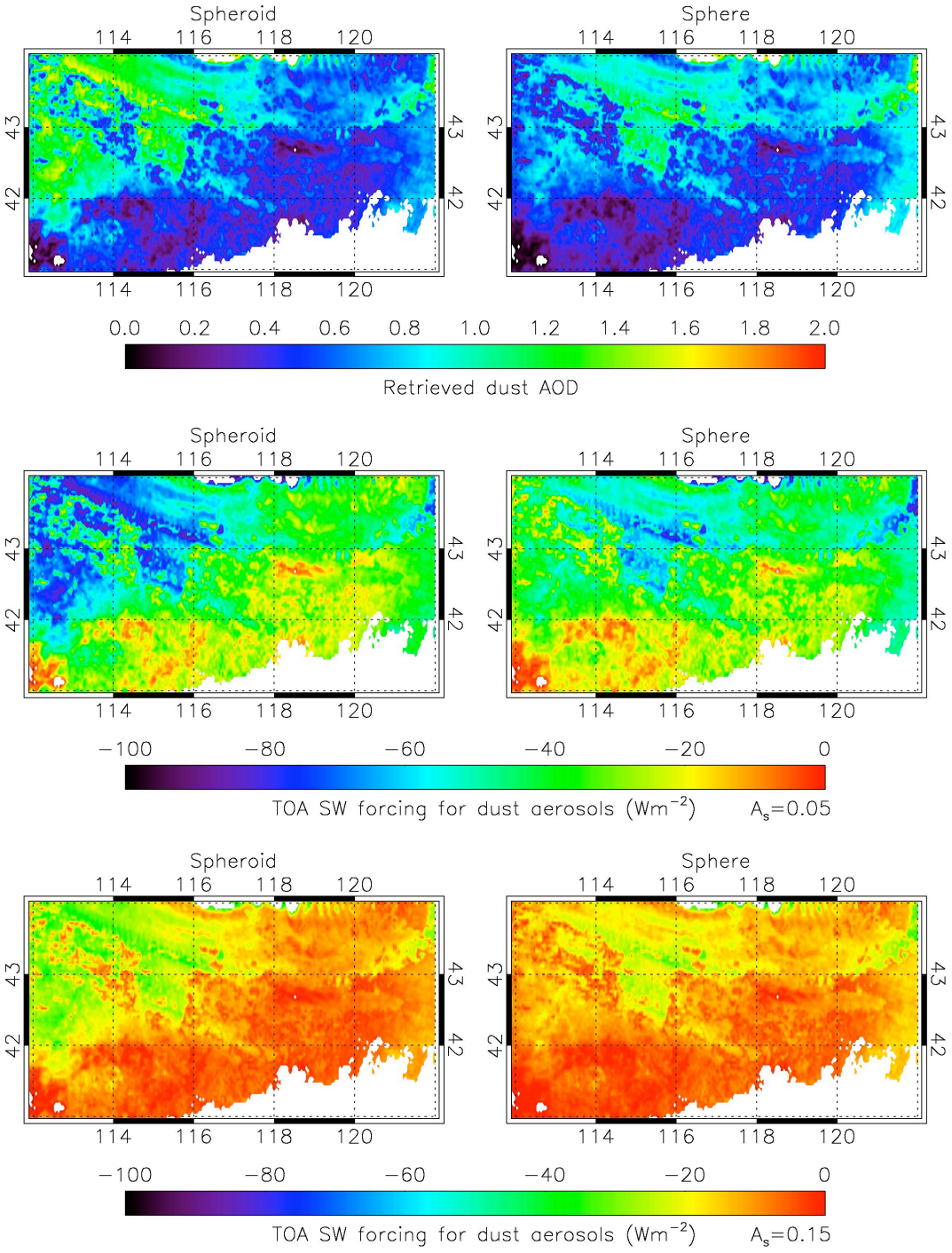

Fig. 44 Spatial distribution of retrieved dust AOD based on the spheroidal and spherical particle shape assumptions and the corresponding TOA instantaneous SWRF for different surface albedos.

The comparison of the simulated instantaneous TOA SWRF between the spheroidal and spherical particle shape assumptions is shown in the left panel of Fig. 45 for different scattering angles. It should be noted that the effect of particle shapes on the dust AOD retrievals is taken into account in the radiative forcing calculations. For scattering angles ranging from 125° to 129°, the instantaneous TOA SWRF based on the spherical particle shape assumption is stronger than the counterpart based on the spheroidal particle shape assumption. For scattering angles larger than 143°, the opposite is observed, and the differences of the instantaneous TOA SWRF between the spheroidal and spherical particle shape assumptions are becoming larger and larger as the scattering angle increases. These results are consistent with the comparison results for the retrieved dust AOD based on different particle shape assumptions, as shown in Fig. 23. The right panel of Fig. 45 shows the relative difference ε_F of the instantaneous TOA SWRF on the basis of these two particle shape assumptions as a function of dust optical depths for different scattering angles. The ε_F is defined as

$$\varepsilon_F = \left| \frac{\Delta F_{sphere} - \Delta F_{spheroid}}{\Delta F_{spheroid}} \right|, \tag{35}$$

where ΔF_{sphere} and $\Delta F_{spheroid}$ represent the instantaneous TOA SWRF based on the spherical and spheroidal particle shape assumptions, respectively. Obviously, the values of ε_F, which can exceed up to 60% at low dust loading conditions, depend critically on the scattering angles at which the dust optical depths are retrieved. The results shown in Fig. 45 demonstrate the effect of particle shapes on the dust radiative forcing calculations cannot be neglected provided this kind of effect is taken into account in the dust AOD retrievals.

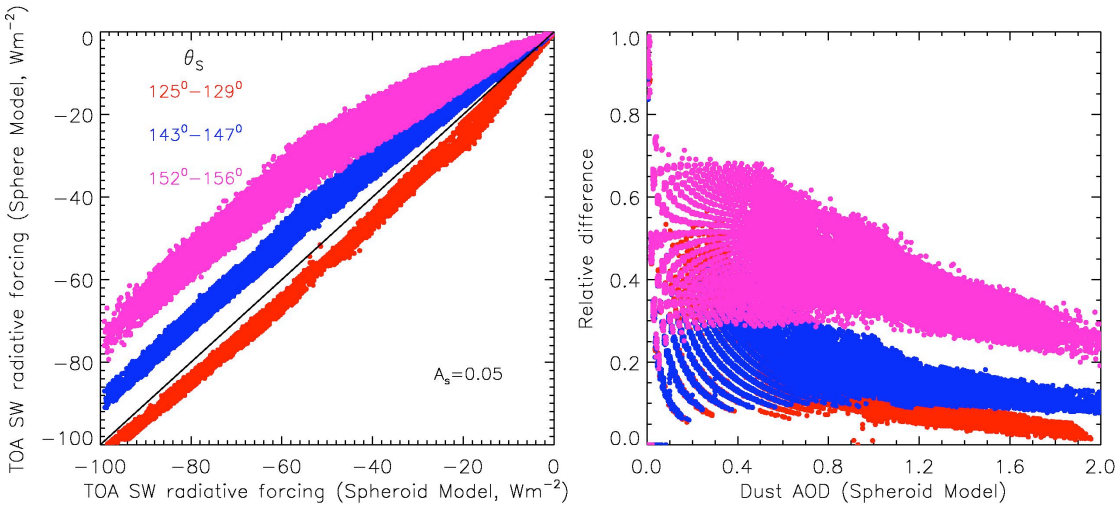

Fig. 45 Left panel: the scatter plots of TOA SW radiative forcing for spherical dust versus the counterpart for spheroidal dust for different scattering angles. Right panel: the corresponding relative differences for TOA SW radiative forcing.

5.5 Summary

With the spheroidal and spherical particle shape assumptions for mineral dust aerosols, the effect of particle shapes on the dust radiative forcing calculations is investigated by focusing on the instantaneous TOA SWRF. Without considering the effect of particle shapes on the dust AOD retrievals, the effect of particle shapes on the single-scattering properties of dust aerosols, hence on the dust direct radiative forcing is negligibly small. However, the effect of particle shapes on the dust direct radiative forcing cannot be neglected provided that the effect of particle shape on the dust AOD retrievals is also taken into account. In addition, the differences of the dust TOA instantaneous SWRF between the spheroidal and spherical particle shape assumptions critically depend on the dust AOD, solar zenith angle, and surface reflectance.

6. SUMMARY AND CONCLUSION

Recently, much effort has been devoted to the study of nonspherical mineral dust aerosols, with the goal of improving our understanding of the optical and radiative properties, as well as developing robust aerosol retrieval algorithms. The present research aims here to support ongoing efforts in the fields of mineral dust aerosol research related to the Deep Blue algorithm by use of MODIS observations, since the empirical phase function used in the Deep Blue algorithm may not be representative of the bulk scattering properties for realistic dust aerosols. First, the LUTS for the Deep Blue algorithm are updated with existing scattering-computational methods, namely, the T-matrix method and IGOM method. The feasibility of the hybrid approach, which has already been employed in Deep Blue algorithm for LUT development, is also demonstrated on the basis of the spheroidal particle shape assumption for the phase function and the spherical particle shape assumption for the other phase matrix elements. Second, a sensitivity study is carried out to quantify the nonspherical effect on the retrieved dust optical depths by using a simple retrieval algorithm that was developed from the principles of the Deep Blue algorithm. It is concluded that the nonspherical effect of mineral dust aerosols cannot be neglected for dust optical depth retrievals, and the assumption of spherical particle shapes for dust aerosol retrievals may lead to a significant underestimation (as much as 20%) of AOD. Furthermore, the differences of the retrieved dust AOD between the spherical and spheroidal particle shape assumptions depend critically on the scattering angle.

From the simple retrieval algorithm, the effect of thin cirrus clouds on the dust optical depth retrievals has also been investigated and quantified from MODIS observations. It is found that the failure to identify pixels contaminated by thin cirrus clouds may lead to larger errors in the retrieved dust optical depths. It is also discovered that the errors in the retrieved dust optical depths due to the effect of thin cirrus under heavy dust conditions are comparable to the optical depth for thin cirrus clouds.

Finally, with the spheroidal and spherical particle shape assumptions for mineral dust aerosols, the effect of particle shapes on the dust radiative forcing calculations is also investigated by focusing on the instantaneous TOA SWRF. Without considering the effect of particle shapes on the dust optical depth retrievals, the effect of particle shapes on the scattering properties of dust aerosols, hence on the dust radiative forcing is negligibly small. However, the effect of particle shapes on the dust radiative forcing cannot be neglected provided that this kind of effect is taken into account in the dust AOD retrievals.

REFERENCES

Ackerman, S. A. (1997), Remote sensing aerosols using satellite infrared observations, *J. Geophys. Res.*, *102*, 17069-17079.

Baum, B. A., P. Yang, A. J. Heymsfield, S. Platnick, M. D. King, Y. X. Hu, and S. T. Bedka (2005), Bulk scattering properties for the remote sensing of ice clouds. Part 2: narrowband models, *J. Appl. Meteorol.*, *44*, 896-1911.

Beyer, W. H. (1981), *CRC standard mathematical tables*, Boca Ration, FL: CRC Press.

Bi, L., P. Yang, G. W. Kattawar, and R. Kahn (2008), Single-scattering properties of tri-axial ellipsoidal particles for a size parameter range from the Rayleigh to geometric-optics regimes, *Appl. Opt.*, *48*, 114-126.

Bi, L., P. Yang, G. W. Kattawar, and R. Kahn (2010), Modeling optical properties of mineral aerosol particles by using non-symmetric hexehedra, *Appl. Opt.*, *49*, 334-342.

Bohren, C. F., and D. R. Huffman (1983), *Absorption and scattering of light by small particles*, New York: Wiley.

Chami, M., R. Santer, and E. Dilligeard (2001), Radiative transfer model for the computation of radiance and polarization in an ocean-atmosphere system: Polarization properties of suspended matter for remote sensing, *Appl. Opt.*, *40*, 2398-2416.

Christopher, S. A., and T. A. Jones (2008), Dust radiative effect over global oceans, *IEEE Trans. Geosci. Remote Sens.*, *5*, 74-77.

Christopher, S. A., and J. Zhang (2002), Shortwave aerosol radiative forcing from MODIS and CERES observations over the oceans, *Geophys. Res. Lett.*, *29*, doi:10.1029/2002GL014803.

Chu, D. A., Y. J. Kaufman, C. Ichoku, L. A. Remer, D. Tanre, and B. N. Holben (2002), Validation of MODIS aerosol optical depth retrieval over land, *Geophys. Res. Lett.*, *29*, doi:10.1029/2001GL013205.

Curtis, D. B., B. Meland, M. Aycibin, N. P. Arnold, V. H. Grassian, M. A. Young, and P. D. Kleiber (2008), A laboratory investigation of light scattering from representative components of mineral dust aerosols at a wavelength of 550nm, *J. Geophys. Res.*, *113*, doi:10.1029/2007JD009387.

d'Almeida, G. A., P. Koepke, and E. P. Shettle (1991), *Atmospheric aerosols: Global climatology and radiative characteristics*, Hampton, VA: A. Deepak.

Darmenov, A., and I. N. Sokolik (2005), Identifying the regional thermal-IR radiative signature of mineral dust with MODIS, *Geophys. Res. Lett.*, *32*, doi:10.1029/2005GL023092.

Deuze, J. L., M. Herman, P. Goloub, D. Tanre, and A. Marchand (1999), Characterization of aerosols over ocean from POLDER/ADEOS-1, *Geophys. Res. Lett.*, *26*, 1421-1424.

De Haan, J. F, P. B. Bosma, and J. W. Hovenier (1987), The adding method for multiple scattering calculations of polarized light, *Astron. Astrophys.*, *183*, 371-391.

Draine, B. T., and P. J. Flatau (1994), Discrete dipole approximation for scattering calculations, *J. Opt. Soc. Am.*, *11*, 1491-1499.

Dubovik, O., B. N. Holben, T. Lapyonok, A. Sinyuk, M. I. Mishchenko, P. Yang, and I. Slutsker (2002a), Non-spherical aerosol retrieval method employing light scattering by spheroids, *Geophys. Res. Lett.*, *29*, doi:10.1029/2001GL014506.

Dubovik, O., B. N. Holben, T. F. Eck, A. Smirnov, Y. J. Kaufman, M. D. King, D. Tanre, and I. Slutsker (2002b), Variability of absorption and optical properties of key aerosol types observed in worldwide locations, *J. Atmos. Sci.*, *59*, 590-608.

Dubovik, O., A. Sinyuk, T. Lapyonok, B. N. Holben, M. I. Mishchenko, P. Yang, T. F. Eck, H. Volten, O. Muñoz, B. Veihelmann, W. J. van der Zande, J. F. Leon, M. Sorokin, and I. Slutsker (2006), Application of spheroid models to account for aerosol particle nonsphericity in remote sensing of desert dust, *J. Geophys. Res.*, *111*, doi: 10.1029/2005JD006619.

Dutton, E. G., P. Reddy, S. Ryan, and J. J. Deluisi (1999), Features and effects of aerosol optical depth observed at Mauna Loa, Hawaii, *J. Geophys. Res.*, *99*, 8295-8306.

Eck, T. F., B. N. Holben, O. Dubovik, A. Smirnov, P. Coloub, H. B. Chen, B. Chatenet, L. Gomes, X. Y. Zhang, S. C. Tsay, Q. Ji, D. Giles, and I. Slutsker (2005), Columnar aerosol optical properties at AERONET sites in central eastern Asia and aerosol transport to the tropical mid-Pacific, *J. Geophys. Res.*, *110*, doi:10.1029/2004JD005274.

Foot, J. S. (1998), Some observations of the optical properties of clouds, 2, cirrus, *Q. J. Roy. Meteor. Soc.*, *114*, 145-164.

Fu, Q., and K. N. Liou (1993), Parameterization of the radiative properties of cirrus clouds, *J. Atmos. Sci.*, *50*, 2008-2025.

Fu, Q., T. J. Thorsen, J. Su, J. M. Ge, and J. P. Huang (2009), Test of Mie-based single-scattering properties of non-spherical dust aerosols in radiative flux calculations, *J. Quant. Spectrosc. Radiat. Transfer*, *110*, 1640-1653.

Gao, B. C., Y. J. Kaufman, D. Tanre, and R. R. Li (2002), Distinguishing tropospheric aerosols from thin cirrus clouds for improved aerosol retrievals using the ratio of 1.38-μm and 1.24-μm channels, *Geophys. Res. Lett.*, *29*, doi:10.1029/2002GL015475.

Grenfell, T. C., and S. G. Warren (1999), Representation of a nonspherical ice particle by a collection of independent sphere for scattering and absorption of radiation, *J. Geophys. Res.*, *104*, 31697-31709.

Hansell, R. A., S. C. Ou, K. N. Liou, J. K. Roskovensky, S. C. Tsay, C. Hsu, and Q. Ji (2007), Simultaneously detection/separation of mineral dust and cirrus clouds using MODIS thermal infrared window data, *Geophys. Res. Lett.*, *34*, doi:10.1029/2007GL029388.

Hansen, J. E., and L. D. Travis (1974), Light scattering in planetary atmospheres, *Space Sci. Rev.*, *16*, 527-610.

Haywood, J., and O. Bougher (2000), Estimates of the direct and indirect radiative forcing due to tropospheric aerosols: A review, *Rev. Geophys.*, *38*, 513-543.

Heymsfield, A. J., and J. Iaquinta (2000), Cirrus crystal terminal velocities, *J. Atmos. Sci.*, *57*, 916-938.

Herman, J. R., and E. A. Celarier (1997), Earth surface reflectivity climatology at 340-380 nm from TOMS data, *J. Geophys. Res.*, *102*, 28003-28011.

Hsu, N. C., S. C. Tsay, M. D. King, and J. R. Herman (2004), Aerosol properties over bright-reflecting source regions, *IEEE Trans. Geosci. Remote Sens.*, *42*, 557-569.

Hsu, N. C., S. C. Tsay, M. D. King, and J. R. Herman (2006), Deep blue retrievals of Asian aerosols properties during ACE-Asia, *IEEE Trans. Geosci. Remote Sens.*, *44*, 3180-3195.

Hu, Y. A., G. Wielicki, B. Lin, G. Gibson, S. C. Tsay, K. Stamnes, and T. Wong (2000), δ-fit: A fast and accurate treatment of particle scattering phase functions with weighted singular-value decomposition least-squares fitting, *J. Quant. Spectrosc. Radiat. Transfer*, *65*, 681-690.

Jin, Z. H., and K. Stamnes (2004), Radiative transfer in nonuniformly refracting layered media: atmosphere-ocean system, *Appl. Opt.*, *33*, 431-442.

Kahnert, M. (2004), Reproducing the optical properties of fine desert dust aerosols using ensembles of simple model particles, *J. Quant. Spectrosc. Radiat. Transfer*, *85*, 231-249.

Kahnert, M., T. Nousiainen, and B. Veihelmann (2005), Spherical and spheroidal model particles as an error source in aerosol climate forcing and radiance computations: A case study for feldspar aerosols, *J. Geophys. Res.*, *110*, doi:10.1029/2004JD005558.

Kahnert, M., T. Nousiainen, and P. Raisanen (2007), Mie simulations as an error source in mineral aerosol radiative forcing calculations, *Q. J. Roy. Meteor. Soc.*, *133*, 299-307.

Kalashnikova, O. V., and I. N. Sokolik (2002), Importance of shapes and compositions of wind-blown dust particles for remote sensing at solar wavelength, *Geophys. Res. Lett.*, *29*, doi:10.1029/2002GL014947.

Kalashnikova, O. V., R. Kahn, I. N. Sokolik, and W. H. Li (2005), Ability of multiangle remote sensing observations to identify and distinguish mineral dust types: Optical

models and retrievals of optically thick plumes, *J. Geophys. Res.*, *110*, doi:10.1029/2004JD004550.

Kaufman, Y. J., D. Tanre, L. Remer, E. F. Vermote, D. A. Chu, and B. N. Holben (1997), Operational remote sensing of tropospheric aerosol over the land from EOS-MODIS, *J. Geophys. Res.*, *102*, 17051-17068.

Kaufman, Y. J., D. Tanre, and O. Boucher (2002), A satellite view of aerosols in the climate system, *Nature, 419*, 215-223.

King, M. D., Y. J. Kaufman, W. P. Menzel, D. Tanre (1992), Remote sensing of cloud, aerosol, and water vapor properties from the moderate resolution imaging spectrometer (MODIS), *IEEE Trans. Geosci. Remote Sens.*, *30*, 1-27.

King, M. D., Y. J. Kaufman, D. Tanre, and T. Nakajima (1999), Remote sensing of tropospheric aerosols from space: Past, present and future, *B. Am. Meteorol. Soc.*, *80*, 2229-2259.

Koelemeijer R. B. A., J. F. de Haan, and P. Stammes (2003), A database of spectral surface reflectivity in the range 335-772nm derived from 5.5 years of GOME observations, *J. Geophys. Res.*, *108*, doi:10.1029/2002JD002429.

Kokhanovsky, A. A., B. Mayer, and V. V. Rozanov (2005), A parameterization of the diffuse transmittance and reflectance for aerosol remote sensing, *Atmos. Res.*, *73*, 37-43.

Kokhanovsky, A. A., W. Von Hoyningen-Huene, and J. P. Burrows (2006), Atmospheric aerosol load as derived from space, *Atmos. Res.*, *81*, 176-185.

Koren, I., E. Ganor, and J. H. Joseph (2001), On the relation between size and shape of desert dust aerosol, *J. Geophys. Res.*, *106*, 18047-18054.

Levy, R. C., L. A. Remer, and Y. J. Kaufman (2004), Effects of neglecting polarization on the MODIS aerosol retrieval over land, *IEEE Trans. Geosci. Remote Sens.*, *42*, 2576-2583.

Levy, R. C., L. A. Remer, and O. Dubovik (2007), Global aerosol optical properties and application to moderate resolution imaging spectroradiometer aerosol retrieval over land, *J. Geophys. Res.*, *112*, doi:10.1029/2006JD007815.

Li, F., A. M. Vogelmann, and V. Ramanathan (2004), Saharan dust radiative forcing measured from space, *J. Climate*, *17*, 2558-2571.

Liao, H and J. H. Seinfeld (1998), Radiative forcing by mineral dust aerosols: Sensitivity to key variables, *J. Geophys. Res.*, *103*, 31637-31645.

Loeb, N. G., and M. S. Natividad (2005), Top-of-atmosphere direct radiative effect of aerosols over global oceans from Merged CERES and MODIS observations, *J. Climate*, *18*, 3506-3526.

Martins, J. V., D. Tanre, L. A. Remer, Y. J. Kaufman, S. Mattoo, and R. Levy (2002), MODIS cloud screening for remote sensing of aerosol over oceans using spatial variability, *Geophys. Res. Lett.*, *29*, doi:10.1029/2001GL013252.

Martonchik, J.V., and D. J. Diner (1992), Retrieval of aerosol optical properties from multi-angle satellite imagery, *IEEE Trans. Geosci. Remote Sens.*, *30*, 223-230.

McFarquhar, G. M., A. J. Heymsfield, J. Spinhirne, and B. Hart (2000), Subvisual tropopause tropical cirrus: Observations and radiative impacts, *J. Atmos. Sci.*, *57*, 1841-1853.

Mishchenko, M. I., A. A. Lacis, and L. D. Travis (1994), Errors introducing by the neglect of polarization in radiance calculations for Rayleigh scattering atmospheres, *J. Quant. Spectrosc. Radiat. Transfer*, *51*, 491-510.

Mishchenko, M. I. and L. D. Travis (1994), T-matrix computations of light scattering by large spheroidal particles, *Opt. Commun.*, *109*, 16–21.

Mishchenko, M. I., A. A. Lacis, B. E. Carlson, and M. I. Travis (1995), Nonsphericity of dust-like tropospheric aerosols: Implications for aerosol remote sensing and climate forcing, *Geophys. Res. Lett.*, *22*, 1077-1080.

Mishchenko, M. I., L. D. Travis, R. A. Kahn, and R. A. West (1997), Modeling phase functions for dustlike tropospheric aerosols using a shape mixture of randomly oriented polydisperse spheroids, *J. Geophys. Res.*, *102*, 16831-16847.

Mishchenko, M. I., I. V. Geogdzhayev, B. Cairns, W. B. Rossow, and A. A. Lacis (1999), Aerosol retrievals over the ocean by use of channels 1 and 2 AVHRR data: Sensitivity analysis and preliminary results, *Appl. Opt.*, *38*, 7325-7341.

Mishchenko, M. I., I. V. Geoqdzhayev, L. Liu, J. A. Ogren, A. A. Lacis, W. B. Rossow, J. W. Hovenier, H. Volten, and O. Muñoz (2003), Aerosol retrievals from AVHRR radiances: Effect of particle non-sphericity and absorption and an updated long-term global climatology of aerosol properties, *J. Quant. Spectrosc. Radiat. Transfer*, *79*, 953-972.

Mishchenko, M. I., L. D. Travis, and A. A. Lacis (2002), *Scattering, absorption, and emission of light by small articles*, New York: Cambridge University Press.

Myhre, G., and F. Stordal (2001), Global sensitivity experiments of the radiative forcing due to mineral aerosol, *J. Geophys. Res.*, *106*, 18193-18204.

Nakajima, T., M. Tanaka, M. Yamano, M. Shiobara, K. Arao, and Y. Nakanishi (1989), Aerosol optical characteristics in the yellow sand events observed in May, 1982 at Nagasaki—Part 2: Models, *J. Meteor. Soc. Japan*, *67*, 279-291.

Nousiainen, T., and K. Vermeulen (2003), Comparison of measured single-scattering matrix of feldspar particles with T-matrix simulations using spheroid, *J. Quant. Spectrosc. Radiat. Transfer*, *79*, 1031-1042.

Nousiainen, T. (2009), Optical modeling of mineral dust particles: A review, *J. Quant. Spectrosc. Radiat. Transfer*, *110*, 1261-1279.

Nussenzveig, H. M., and W. J. Wiscombe (1980), Efficiency factors in Mie scattering, *Phys. Rev. Lett.*, *18*, 1490-1494.

Okada, K., J. Heintzenberg, K. Kai, and Y. Qin (2001), Shape of atmospheric mineral particles collected in three Chinese arid-regions, *Geophys. Res. Lett.*, *28*, 3123-3126.

Pilinis, C., and X. Li (1998), Particle shape and internal inhomogeneity effect on the optical properties of tropospheric aerosols of relevance to climate forcing, *J. Geophys. Res.*, *103*, 3789-3800.

Purcell, E. M., and C. R. Pennypacker (1973), Scattering and absorption of light by nonspherical dielectric grains, *Astrophys. J.*, *186*, 705-714.

Qu, J. J., X. J. Hao, M. Kafotos, and L. L. Wang (2006), Asian dust storm monitoring combining terra and aqua MODIS SRB measurements, *IEEE Trans. Geosci. Remote Sens.*, *3*, 484-486.

Reid, J. S., H. H. Jonsson, H. B. Maring, A. Smirnov, D. L. Savoie, S. S. Cliff, E. A. Reid, J. M. Livingston, M. M. Meier, O. Dubovik, and S. C. Tsay (2003a),

Comparison of size and morphological measurements of coarse mode dust particles from Africa, *J. Geophys. Res.*, *108*, doi:10.1029/2002JD002485.

Reid, E. A., J. S. Reid, M. M. Meier, M. R. Dunlap, S. S. Cliff, A. Broumas, K. Petty, and H. Maring (2003b), Characterization of African dust transported to Puerto Rico by individual particle and size segregated bulk analysis, *J. Geophys. Res.*, *108*, doi:10.1029/2002JD002935.

Remer, L. A., D. Tanre, Y. J. Kaufman, C. Ichoko, S. Mattoo, R. Levy, D. A. Chu, B. N. Holben, J. V. Martins, R. R. Li, and Z. Ahmad (2002), Validation of MODIS aerosol retrieval over ocean, *Geophys. Res. Lett.*, *29*, doi:10.1029/2001GL013204.

Remer, L. A., Y. J. Kaufman, D. Tanre, S. Mattoo, D. A. Chu, J. V. Martins, R. R. Li, C. Ichoku, R. C. Levy, R. G. Kleidman, T. F. Eck, E. Vermote, and B. N. Holben (2005), The MODIS aerosol algorithm, products, and validation, *J. Atmos. Sci.*, *62*, 947-973.

Roskovensky, J. K., and K. N. Liou (2003), Detection of thin cirrus from 1.38μm/0.65μm reflectance ration combined with 8.6-11μm brightness temperature difference, *Geophys. Res. Lett.*, *30*, doi:10.1029/2003GL018135.

Roskovensky, J. K., and K. N. Liou (2005), Simultaneous determination of aerosol and thin cirrus optical depths over oceans from MODIS data: Some case studies, *J. Atmos. Sci.*, *63*, 2307-2323.

Sokolik, I. N. (2002), The spectral radiative signature of wind-blown mineral dust: Implications fro remote sensing in the thermal IR region, *Geophys. Res. Lett.*, *29*, doi:10.1029/2002GL015910.

Sokolik, I. N., and O. B. Toon (1999), Incorporation of mineralogical composition into models of the radiative properties of mineral aerosols from UN to IR wavelengths, *J. Geophys. Res.*, *104*, 9423-9444.

Sokolik, I. N., D. Winker, G. Bergametti, D. Gillette, G. Carmichael, Y. J. Kaufman, L. Gomes, L. Schuetz, and J. Penner (2001), Introduction to special section on mineral dust: outstanding problems in quantifying the radiative impact of mineral dust, *J. Geophys. Res.*, *106*, 18015-18027.

Tegen, I., A. A. Lacis, and I. Fung (1996), The influence on climate forcing of mineral aerosols form disturbed soils, *Nature*, *380*, 419-422.

Volten, H., O. Muñoz, E. Rol, J. F. de Haan, W. Vassen, J. W. Hovenier, K. Muinonen, and T. Nousiainen (2001), Scattering matrices of mineral aerosol particles at 441.6 and 632.8 nm, *J. Geophys. Res.*, *106*, 17375–17401.

Vouk, V. (1948), Projected area of convex bodies, *Nature*, *162*, 330-331.

Wang, M., and H. R. Gordon (1994), Estimating aerosol optical properties over the oceans with the multiangle imaging spectroradiometer: Some preliminary studies, *Appl. Opt.*, *33*, 4042-4057.

West, R. A., L. R. Doose, A. M. Eibl, M. G. Tomasko, and M. I. Mishchenko (1997), Laboratory measurements of mineral dust scattering phase function and linear polarization, *J. Geophys. Res.*, *102*, 16871-16881.

Wiscombe, W. J. (1977), The Delta-M method: Rapid yet accurate radiative flux calculations fro strongly asymmetric phase functions, *J. Atmos. Sci.*, *34*, 1408-1422.

Wu, L. G., S. A. Braun, J. J. Qu, and X. J. Hao (2006), Simulating the formation of Hurricane Isabel (2003) with AIRS data, *Geophys. Res. Lett.*, *33*, doi:10.1029/2005GL024665.

Yang, P., and K. N. Liou (1996), Geometric-optics-integral-equation method for light scattering by nonspherical ice crystals, *Appl. Opt.*, *35*, 6568-6584.

Yang, P., K. N. Liou, M. I. Mishchenko, and B. C. Gao (2000), Efficient finite-difference time-domain scheme for light scattering by dielectric particles: Application to aerosols, *Appl. Opt.*, *39*, 3727-3737.

Yang, P., Q. Feng, G. Hong, G. W. Katawar, W. J. Wiscombe, M. I. Mishchenko, O. Dubovik, I. Laszlo, and I. N. Sokolik (2007), Modeling the scattering and radiative properties of nonshpherical dust-like aerosols, *J. Aerosol Sci.*, *38*, 995-1014.

Yee, S. K. (1966), Numerical solution of initial boundary value problems involving Maxwell's equations in isotropic media, *IEEE Trans. Geosci. Remote Sens.*, *14*, 302-307.

Zhang, J. L., and S. A. Christopher (2003), Longwave radiative forcing of Saharan dust aerosols estimated from MODIS, MISR, and CERES observations on Terra, *Geophys. Res. Lett.*, *30*, doi:10.1029/2003GL018479.

Zhang, Z., P. Yang, G. W. Kattawar, S. C. Tsay, B. A. Baum, H. L. Huang, Y. X. Hu, A. J. Heymsfield, and J. Reichardt (2004), Geometric optics solution to light scattering by droxtal ice crystals, *Appl. Opt.*, *43*, 2490-2499.

Zhao, T. X. -P., I. Laszlo, O. Dubovik, B. N. Holben, J. Sapper, D. Tanre, and C. Pietras (2003), A study of the effect of non-spherical dust particles on the AVHRR aerosol optical thickness retrievals, *Geophys. Res. Lett.*, *30*, doi:10.1029/2002GL016379.

VITA

Name:	Qian Feng
Address:	Department of Atmospheric Sciences c/o Dr. Ping Yang Texas A&M University College Station, TX 77843-3150
Email Address:	fengqian@ariel.met.tamu.edu
Education:	B.S., Physics, Ocean University of China, 1998 M.S., Physical Oceanography, Ocean University of China, 2001 Ph.D., Physical Oceanography, Ocean University of China, 2004